UNIVERSITÀ DEGLI STUDI DI PADOVA

Dipartimento di Fisica e Astronomia "Galileo Galilei"

Master Degree in Astrophysics and Cosmology

Final dissertation

Investigating a possible solution to the Cosmic Microwave Background Anomalies

Thesis supervisor
Prof. Nicola Bartolo
Thesis co-supervisor
Prof. Michele Liguori

Candidate
Daniela Montes Doria

Academic Year 2022/2023

Abstract

Measurements of the Cosmic Microwave Background (CMB) taken by both WMAP and Planck Satellites have claimed the presence of statistical deviations from the standard cosmological model. These anomalies, although not statistically significant (2-3σ level), raise the possibility of new physics related to the early Universe's initial conditions (from inflation). A recent phenomenological model, proposed by Hansen et al. (2019) successfully reproduces six of these anomalies. This toy model is based on the notion that non-Gaussianity could be the source of these anomalies and resembles models of primordial non-Gaussianity characterized by strongly scale-dependent g_{NL}-like trispectra. The objective of this work is to compute and characterize the trispectrum of the initial curvature perturbation ζ from inflation, which is the Fourier counterpart of the 4-point correlation function, associated with the toy model. This analysis aims to provide insights into the physical properties underlying the toy model. To achieve this, we investigate the shape of the primordial trispectrum of ζ in two specific cases: the folded kite-shape limit and the specialized planar limit. Our preliminary results in the folded limit, where $k_1 = k_2, k_3 = k_4$ and the diagonal $k_{12} = 0$, suggests that this configuration may be more suitable for exploring our trispectrum's shape. However, a more thorough analysis of the trispectrum's shape is needed to gain deeper insights into the type of primordial non-Gaussianity present in the model and to support this initial finding. Additionally, we provide explicit equations for the CMB trispectrum, which can be useful for future numerical analyses. These analyses have the potential to enhance the understanding of the properties that might be responsible for the CMB anomalies and may help in providing both new forecasts and constraints on the non-Gaussian parameter g_{NL} when applied to Planck data.

Contents

Chapter 1

Introduction

The Cosmic Microwave Background (CMB) structure had been hidden for many years due to instrumental limitations. However, advancements in both theory and observational data have firmly established that the CMB carries significant scientific information through its temperature and polarization patterns. Since the initial detection of temperature anisotropies by the COBE satellite, there has been a growing interest in improving sensitivity and acquiring high-quality data on temperature patterns from various missions. Extensive studies of this data have led to the development of the current cosmological model (ΛCDM).

At the same time, measurements of the CMB by satellites like WMAP and Planck have revealed indications of some departures from our standard cosmological model, indicating the presence of unexpected features or anomalies at large angular scales (see, e.g. Ade et al. 2016). While many of these anomalies may not be statistically significant ($2 - 3\sigma$ level), they provide a potential window to explore new physics related to the initial conditions of the early Universe, attempting to explain their presence in the data. Still, some researchers suggest that these anomalies could be attributed to systematic issues or statistical flukes. Examples of these anomalies include large-scale hemispherical power asymmetry, small-scale hemispherical power asymmetry, non-Gaussian hot or cold spots, low power on large angular scales, quadrupole and octopole alignment, and parity asymmetry on large angular scales (Tegmark et al., 2003; Eriksen et al., 2007; Schwarz et al., 2015).

Motivated by the desire to identify a common physical cosmological origin for these anomalies, numerous detailed investigations have been conducted. The proposed models can generally be categorized into two groups: those with the explicit breaking of statistical isotropy and those where statistical isotropy breaking arises (locally) from the presence of primordial non-Gaussianity. Adhikari et al. (2018) found that the hemispherical power asymmetry could be modeled by a local-type trispectrum (the Fourier counterpart of the 4-point correlation function) of primordial curvature perturbations. However, they did not address the issue of an inflationary model capable of explaining power asymmetry. On the other hand, Byrnes et al. (2016b) reported a set of inflationary scenarios that could accommodate the hemispherical asymmetry, concluding that a single-field model is inadequate to reproduce the correct power asymmetry, and a multi-field scenario is more suitable.

A more recent phenomenological model proposed by Hansen et al. (2019) reproduces simultaneously six extensively studied anomalies and is based on the idea that non-Gaussianity may be the origin of these anomalies, manifesting as apparent deviations from statistical isotropy and features in the power spectrum. However, the authors did not derive the physical model that could give rise to the toy model reproducing the CMB anomalies.

As a further development, the same authors also established a one-to-one connection between the temperature field T used in the construction of the toy model and the inflationary curvature perturbation ζ in its most general expression. To achieve this, an expansion (in terms of convolution in Fourier space with a given kernel) of ζ was carried out up to the order of primordial non-Gaussianity g_{NL}, corresponding to cubic non-linearities (Schmidt and Kamionkowski, 2010). Since the proposed model involves the temperature field at the cubic order, it is necessary to explore higher-order correlation functions, such as the four-point function or trispectrum. Thus, the calculations developed up to now in Hansen et al. (2019) serve as a starting point for this thesis, as the previously explained formalism allows us to obtain the expression for the temperature field, expand it in harmonic spherical terms, and derive an expression for the multiple coefficients (a_{lm}) in terms of curvature perturbation (ζ), incorporating the non-Gaussian contribution.

Therefore, this thesis aims to compute and characterize the trispectrum template associated with the toy model developed by Hansen et al. (2019). We can compute the trispectrum in both harmonic space and Fourier space, providing complementary information to properly identify the properties of this high-order correlation function.

In conducting a thorough trispectrum analysis, there are two essential quantities that we aim to obtain. Firstly, the amplitude of the overall non-Gaussianity provides information about the strength of non-Gaussianity, while the so-called “shape” of non-Gaussianity carries valuable information about the underlying physical processes that generate the template. Analyzing these quantities allows us to associate specific information with different inflationary models or cosmological scenarios. To determine these fundamental quantities, we need to analyze the obtained template and identify the functional dependencies and behaviors of the different terms involved.

For instance, the non-Gaussianity parameter g_{NL} determines the overall amplitude of the non-Gaussian contribution to the trispectrum, the functional form of the integral kernel contains valuable information for identifying the shape of our template, and other contributions such as the primordial power spectrum, and geometrical dependencies should be explored as well.

The results of our trispectrum analysis for this specific toy model can provide insights into primordial non-Gaussianity, which may be related to the initial conditions of the early Universe. Additionally, it can offer further information about the physical model underlying the phenomenological model that reproduces the CMB anomalies.

The thesis is organized as follows. In Chapter 2, we present the main foundations of the Standard Cosmological Model (ΛCDM). Chapter 3 contains a brief review of Cosmic Microwave Background (CMB) anisotropies, power spectrum, and trispectrum. Chapter 4 introduces some of the most studied CMB anomalies, exploring possible explanations for their presence in the data. The proposed model by Hansen et al. (2019) is explained in Chapter 5, recovering the main equations. In Chapter 6, the trispectrum of the toy model is calculated and some of the characteristics of the primordial trispectrum of ζ are studied, such as the shape. Finally, we provide a discussion of our results, along with the most relevant conclusions and future work in Chapter 7.

Chapter 2

Standard Cosmological Model ΛCDM

Over the last few years, numerous pieces of evidence have pointed to a comprehensive picture of the Universe, in which our current understanding is consistent with the parametric model Lambda Cold Dark Matter (ΛCDM). According to this model, the Universe is experiencing an accelerated expansion and is comprised of three main components, primarily composed of Dark Energy (DE), which drives the late accelerated expansion of the Cosmos and is thought to be in the form of the cosmological constant Λ. The second largest constituent is denominated Cold Dark Matter (CDM), a non-luminous substance that interacts only through gravity. In addition to these, there is baryonic matter, also known as ordinary matter. Indeed, with these three ingredients, a wide variety of cosmological observations can be explained Heavens (2008).

The foundations of this description are the Einstein Field Equations (EFE), which describe the relationship between the geometry (curvature of spacetime) and the distribution of matter and energy, and the Cosmological Principle, which states that the Universe is homogeneous and isotropic on a large scale ($\sim$ 200 Mpc). These fundamental ideas provide the framework for understanding the evolution of the Cosmos, identifying its components, and making predictions about its potential future scenarios. The EFE states that

$$R_{\mu\nu} - \frac{1}{2} g_{\mu\nu} R = 8\pi G T_{\mu\nu} \,, \tag{2.1}$$

where $R_{\mu\nu}$ and R are respectively the Ricci tensor and scalar, $g_{\mu\nu}$ the metric, G the Newtonian gravitational constant, and $T_{\mu\nu}$ is the energy-momentum tensor of the fluid which describes the energy content of the Universe.

Within the framework of the EFE, we can describe the dynamics of an expanding

Universe with curvature k, that is symmetric under rotation and spatial translations, conditions that satisfy the Friedmann-Lemaître-Robertson-Walker (FLRW) metric given by

$$d^2s = -d^2t + a^2(t)\left[\frac{d^2r}{1-kr^2} + r^2 d\Omega^2\right], \tag{2.2}$$

where t represents the cosmic time of an observer comoving with the cosmic fluid, $a(t)$ is the scale factor that accounts for the expansion of the Universe, and k parametrizes the curvature as follows: $k = 0$ corresponds to a flat universe, $k = +1$ to a closed universe, and $k = -1$ to an open universe.

The set of equations that govern the evolution of this model is the Friedmann Equations, which can be derived from the EFE by explicitly considering the 00 and ij components and exploiting the conservation laws given by $\nabla_\mu T^{\mu\nu} = 0$. Here, $T^{\mu\nu} = diag[-\rho(t), P(t), P(t), P(t)]$ represents the stress-energy tensor of a perfect fluid. Consequently, we obtain

$$\left(\frac{\dot{a}}{a}\right)^2 = \frac{8\pi G}{3}\rho - \frac{k}{a^2} + \frac{\Lambda}{3}, \tag{2.3}$$

$$\frac{\ddot{a}}{a} = -\frac{4\pi G}{3}(\rho + 3P) + \frac{\Lambda}{3}, \tag{2.4}$$

$$\dot{\rho} = -3H(\rho + P), \tag{2.5}$$

where $H = \dot{a}/a$ is the Hubble parameter, ρ denotes the energy density, and P stands for the isotropic pressure of the fluid. The dot notation indicates differentiation with respect to the cosmic time t. It is important to note that only two of these equations are independent, so we require an additional equation to complete the system. This additional expression is the equation of state, given by $P = w\rho$, where the value of w depends on the specific energy content under consideration.

2.1 Components of the Universe

The most abundant component of the Universe is an enigmatic form of energy known as Dark Energy. This mysterious force exerts its influence on large scales, resulting in accelerated expansion. The acceptance of this hypothesis grew substantially in the late 1990s, supported by observations of distant supernovae (e.g. Riess et al. 1998). Dark Energy is commonly associated with two forms: the cosmological constant, denoted as Λ, and scalar fields such as quintessence or moduli. It is the vacuum energy of the system that drives the accelerated expansion of the Universe. In general, to achieve accelerated expansion, a field with a state equation parameter

$w < -1/3$ is required. Particularly, Λ corresponds to a source field with $w = -1$, implying a negative pressure $P = -\rho$. Currently, Dark Energy constitutes approximately 68% of the total energy density of the Universe.

Another dominant component of the Universe is a strange form of pressureless matter, known as Dark Matter, which fills our Universe and is roughly five times more abundant than ordinary matter Garrett and Duda (2011). The presence of DM is essential as it provides the gravitational pull necessary to explain the observed large-scale structure, the formation of galaxies, and galaxy clusters. Although DM remains elusive and has yet to be directly detected, compelling cosmological and astrophysical evidence strongly supports its existence (see, for example Freese, 2009). Furthermore, Dark Matter is described as a non-radiating, approximately collisionless, and non-relativistic particle, which accounts for roughly 27% of the total energy density.

Surprisingly, ordinary baryonic matter which includes everything made up of protons, electrons, and neutrons accounts for only about 5% of the total energy density of the Universe. There is also a small percentage that corresponds to the contribution of radiation.

The ΛCDM model incorporates these components to accurately describe various observed properties of the Universe, including the accelerating expansion, the Cosmic Microwave Background (CMB) radiation and its anisotropies, the abundance pattern of the light elements (Hydrogen, Helium, and Lithium), and the formation and evolution of the large-scale structure. However, it is the addition of inflation to ΛCDM that allows for the development of what we commonly refer to as the Standard Cosmological Model.

Through the combined analyses of data from different cosmological observations, such as the CMB, galaxy surveys, and supernovas, scientists have not only validated but also refined the inflation + ΛCDM model. This model is described by six fundamental parameters: Ω_b baryon density, Ω_c CDM density, Ω_Λ density parameter for the cosmological constant, H_0 Hubble constant today, A_s amplitude, and n_s spectral index of the scalar fluctuations. The current best-fit values for these parameters are presented in Table 2.1. It is important to note that the last two parameters, A_s and n_s, are derived from the power spectrum of a specific inflationary model, for instance, the single-field model.

Parameters	Planck (CMB + Lensing)
$\Omega_b h^2$	0.0224±0.0001
$\Omega_c h^2$	0.120±0.001
Ω_Λ	0.6847 ± 0.0073
$H_0(\text{km}s^{-1}\text{Mpc}^{-1})$	67.4 ± 0.5
ln $(10^{10}A_s)$	3.044 ± 0.014
n_s	0.965±0.004

Table 2.1: Values for the six-parameter inflation + ΛCDM model obtained by fitting the full-mission Planck data of the CMB, taken from Aghanim et al. (2020).

2.2 Thermal history of the Universe

The Standard Cosmological Model, therefore, consists of the following: the Universe originated from an extremely hot and dense state known as the Big Bang (BB) approximately 13.8 Gyr ago. During its early moments, within the first 10^{-35} seconds, it underwent a phase of nearly exponential expansion. Since then, the Universe has continued to expand, under the gravitational influence described by General Relativity. During this inflationary epoch, quantum fluctuations in the inflaton field played an important role in establishing the initial conditions for the generation of the primordial density perturbations.

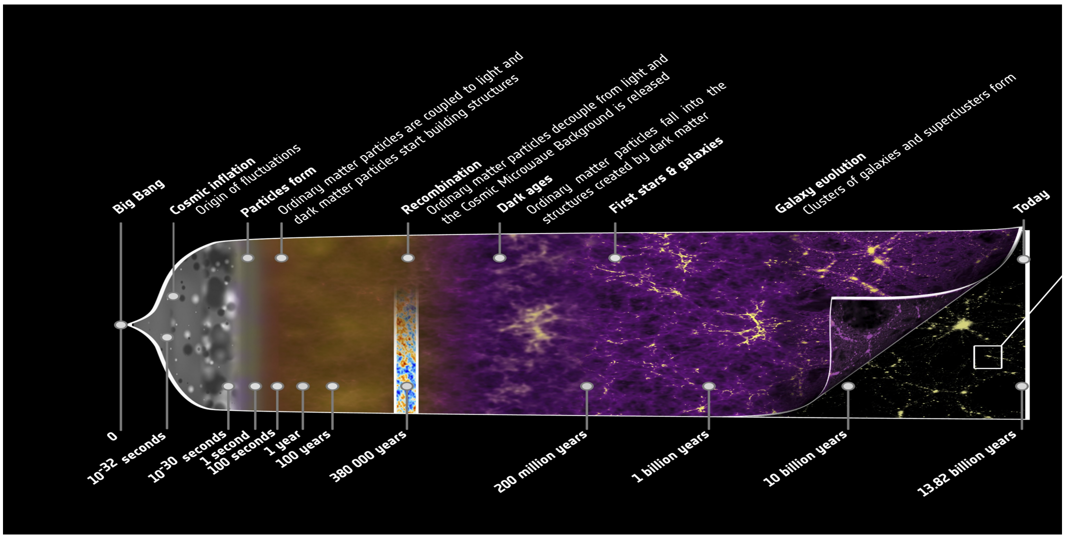

Figure 2.1: Schematic representation of the history of our Universe, taken from ESA – C. Carreau.

Following the rapid expansion phase, a crucial process known as Reheating occurred, facilitating efficient thermalization. This marked the beginning of the radiation-dominated era, characterized by a fluid with an equation of state, where $P = 1/3\rho$, and a scale factor, $a = t^{1/2}$. As the Universe continued to expand and cool down, various particles began to form, including protons, electrons, and neutrons. When the temperature reached $\sim$ 3000 K, roughly 380.000 years after the BB, the energy of photons dropped to a level where protons and electrons could combine, forming neutral hydrogen atoms through the process of recombination. This had a major effect, for the first time, the Universe became transparent and photons could travel freely through space. The decoupling of photons from matter led to the formation of CMB radiation, which is the relic radiation from the early Universe that we can observe today.

After the recombination phase ended, the Universe entered the matter-dominated era. During this time, the dominant energy density was attributed to pressureless, non-relativistic matter, comprising both CDM and baryonic matter. The scale factor for this case is described by $a = t^{2/3}$. Throughout this epoch, neutral hydrogen gas continued to evolve. Eventually, the temperature and density conditions propitiated the synthesis of light elements, such as Hydrogen (H), Helium (He), and a trace amount of Lithium (Li). This process is known as Big Bang Nucleosynthesis (BBN) and has a fundamental role in understanding the abundance of light elements in the Universe. Following the era of BBN, galaxies and large-scale structures began to form.

At present, the Universe continues its expansion, causing galaxies to move away from each other. Furthermore, DE has emerged as the dominant component of the total energy density. Consequently, the ultimate fate of the Cosmos and the long-term evolution of its constituents remain actively researched topics.

2.3 The Inflationary Paradigm

The detection of the CMB reinforces the Hot Big Bang theory as the leading explanation for the origin of the Universe. However, despite its success in explaining many observations at that time, there were several notable "shortcomings". The first of these inconsistencies is dubbed the *Horizon problem.* This problem arises from the fact that CMB radiation exhibits a remarkably uniform temperature across the entire sky. This uniformity suggests that distant regions of the Universe should have been in causal connection at certain points in cosmic history. However, it becomes puzzling when one considers that these regions were separated by vast distances, and should not have had enough time to communicate with each other. Consequently, there seems to be no apparent reason for them to be causally connected, and even less to have the same thermal properties.

Another issue is the *Flatness problem*, which is connected to the curvature term in equation (2.5). Nowadays, we understand that the Universe is nearly flat, with a value of $\Omega_k = 10^{-2}$, as indicated in Aghanim et al. (2020). To account for this current value of Ω_k, the HBB theory predicts that the early Universe was even flatter, requiring a fine-tuning of the initial value to $\Omega_k = 10^{-60}$, a seemingly unnatural condition. Therefore, the inflationary paradigm, proposed by Guth (1981), emerged as a potential solution to address the shortcomings of the HBB model.

It is widely accepted that the Universe underwent a phase of accelerating expansion shortly after the Big Bang. This period of rapid expansion, known as inflation, was remarkably brief, during which the universe's size increased by a factor of at least e^{60}. Then, in this inflationary phase, regions that were causally connected before inflation could come into thermal equilibrium. However, as inflation ended, these same regions became causally disconnected and grew distant from each other. This phenomenon offers a compelling explanation for the characteristics exhibited by CMB radiation.

Furthermore, inflation provides a solution to the fine-tuning problem. Even if the Universe began with arbitrary initial conditions, the quasi-exponential expansion during inflation restores the value of the curvature consistent with a flat universe. In addition to these benefits, inflationary theory also provides an explanation for the formation of large-scale structures in the Cosmos. It proposes that quantum fluctuations during this period acted as seeds for density perturbations, which subsequently grew, leading to the formation of the structures we observe in the Universe today.

As a result, the inflationary theory provides a compelling explanation for the origin and characteristics of our Universe, and it has indeed become an essential part of the cosmological model.

2.3.1 Single field Inflation

The simplest theory to explain the early rapid expansion of the Universe is the single-field model, also known as Cosmic Inflation. This concept was originally proposed by Guth (1981), where the mechanism driving the expansion is the vacuum energy density of a scalar field called the inflaton field.

As previously discussed, in order to achieve inflation, the acceleration term in the second Friedmann equation (2.5) must be positive, indicated by $\ddot{a} > 0$. This condition implies that the equation of state parameter must satisfy $w < -1/3$. Consequently, a mechanism is required to provide a sufficiently negative pressure during this phase. One possible option is the cosmological constant Λ, however, the exponential expansion it induces never ends, which is incompatible with the observed history of the Universe. Alternatively, a single scalar field φ, can mimic the behavior of Λ and drive an expansion that terminates when specific conditions are no longer fulfilled.

To examine the evolution of this scalar field, we assume it is minimally coupled to gravity, resulting in an action that takes the following form

$$S = S_{HE} + S_{\varphi} = \int d^4x\sqrt{-g}\left(R - \frac{1}{2}g^{\mu\nu}\partial_\mu\varphi\partial_\nu\varphi - V(\varphi)\right) , \tag{2.6}$$

the above expression is the sum of two components: the gravitational Hilbert-Einstein action S_{HE} and the action of the inflaton scalar field S_φ. The lagrangian for the real scalar field is constructed with a canonical kinetic term and a potential term $V(\varphi)$. The specific form of the potential can vary depending on the inflation model[1].

Additionally, the inflaton stress-energy momentum tensor $T_{\mu\nu}$ is given by

$$T_{\mu\nu} = \partial_\mu\varphi\partial_\nu\varphi - g_{\mu\nu}\left[\frac{1}{2}g^{\alpha\beta}\partial_\alpha\,\varphi\partial_\beta\,\varphi - V(\varphi)\right] . \tag{2.7}$$

Furthermore, the dynamics of the inflaton field is described by the Equation of Motion (EoM), derived from the variational principle, resulting in

$$\ddot{\varphi} + 3H\dot{\varphi} - \frac{\nabla^2\varphi}{a^2} = -\frac{\partial V}{\partial\varphi} , \tag{2.8}$$

it is worth mentioning that this expression corresponds to the Klein-Gordon equation for a quantum scalar field in the FLRW metric. In this equation, the term $3H\dot{\varphi}$ can be interpreted as a form of friction due to the expansion of the Universe.

In general, the inflaton field φ is decomposed into the sum of a background value and quantum fluctuations, as follows

$$\varphi(\boldsymbol{x}, t) = \varphi_0(t) + \delta\varphi(\boldsymbol{x}, t) , \tag{2.9}$$

here, the classical background value represents the homogeneous and slowly varying part of the field, denoted as $\langle\varphi(\boldsymbol{x}, t)\rangle = \varphi_0(t)$. On the other hand, quantum fluctu-

---

[1] For instance, the potential $V(\varphi)$ can take the shape of a simple quadratic potential $V(\varphi) = \frac{1}{2}m_\varphi^2\varphi^2$, a self-interaction potential $V(\varphi) = \frac{\lambda}{4}\varphi^4$ or an effective potential to account for interactions between φ and other fields.

ations describe random perturbations in the field, with the property, $\langle\delta\varphi(\boldsymbol{x},t)\rangle = 0$. It is commonly assumed that $\langle\delta\varphi^2(\boldsymbol{x},t)\rangle \ll \varphi_0^2(t)$, a condition that is observationally supported by the small value of the CMB temperature anisotropies, $\Delta T/T \simeq 10^{-5}$, which are related to the quantum fluctuations.

Evaluating equation (2.7) for the case of the background value $\varphi_0(t)$, we obtain the following components of the stress-energy tensor

$$\begin{aligned} T^0_0 &= -\left[\tfrac{1}{2}\dot\varphi_0^2(t) + V(\varphi_0)\right] = -\rho_\varphi(t)\,, \\ T^i_j &= \left[\tfrac{1}{2}\dot\varphi_0^2(t) - V(\varphi_0)\right]\delta^i_j = P_\varphi(t)\delta^i_j\,, \end{aligned} \tag{2.10}$$

with such an energy-momentum tensor, we can achieve an inflationary period by ensuring that, at a certain moment, the potential energy dominates over the kinetic term, meaning $V(\varphi) \gg \frac{1}{2}\dot\varphi^2$. This condition implies that the pressure $P_\varphi \sim -V(\varphi) \sim -\rho_\varphi$. This requirement is fulfilled when φ_0 traverses an almost flat region of its potential, a state known as the *slow-roll regime*, as depicted in figure 2.2. During this phase, inflation is primarily driven by the vacuum energy density of φ, and the potential can be treated as constant.

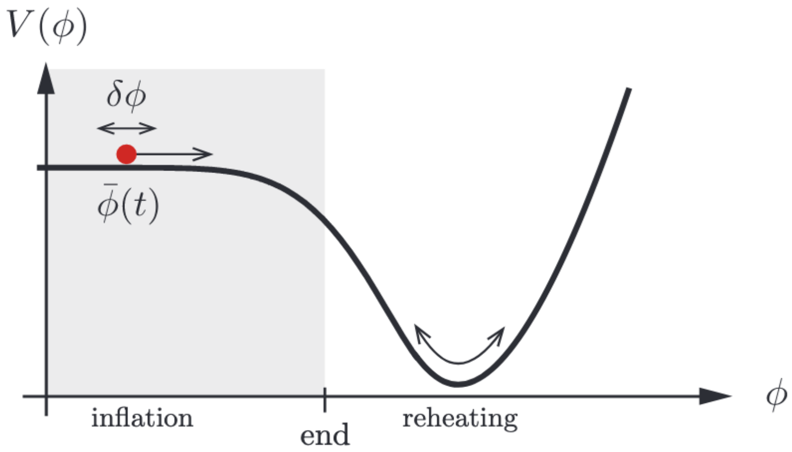

Figure 2.2: Representation of the inflationary phase known as a *slow-roll regimen* illustrated as a shaded area in the graph. Image credit Baumann (2012).

To establish and maintain the slow-roll regime for a sufficiently extended duration, certain conditions must be satisfied. These conditions are the *first slow-roll condition*, which dictates that $V(\varphi) \gg \dot\varphi^2$, and the *second slow-roll condition*, which stipulates that $\ddot\varphi \ll 3H\dot\varphi$. Fulfilling these conditions ensures that the potential energy dominates over the kinetic energy of the scalar field φ, resulting in a slow and sustained evolution of the field.

Moreover, we can introduce some parameters to quantify the characteristics of the slow-roll dynamics,

$$\epsilon = -\frac{\dot{H}}{H^2} \simeq \frac{3}{2}\frac{\dot{\varphi}^2}{V(\varphi)}\,, \tag{2.11}$$

$$\eta = -\frac{\ddot{\varphi}}{H\dot{\varphi}} \simeq \frac{V''}{3H^2} - \frac{\dot{H}}{H^2}\frac{V'}{3H\dot{\varphi}} \simeq \eta_v - \epsilon\,, \tag{2.12}$$

where ϵ quantifies the flatness of the potential, while η controls the duration of inflation. It is important to note that these parameters must satisfy the condition $\epsilon, \eta \ll 1$. Then, inflation comes to an end when these parameters reach unity. These quantities are useful to compare the theoretical predictions with observational data. In fact, a hierarchy of parameters can be constructed, with ϵ and η serving as the first in this hierarchy.

2.3.2 Cosmological perturbations from Inflation

In the early Universe, during the inflationary epoch, the inflaton field underwent quantum fluctuations. To comprehend this phenomenon, it is important to study how these small-scale fluctuations, denoted as $\delta\varphi$, evolve into cosmological perturbations on larger scales.

These primordial quantum fluctuations originated on scales much smaller than the comoving Hubble radius, r_H[2]. Subsequently, inflation amplified and stretched these fluctuations beyond the horizon scale. On such scales, the fluctuations are no longer causally connected, and they remain nearly constant over time because microscopic physics has negligible influence on their evolution. Additionally, the fluctuations are intimately linked with density perturbations, $\delta\rho$, which give rise to the observed anisotropy in the CMB temperature. As these perturbations re-enter the horizon, they serve as the initial conditions for the formation of structures in the Universe. For a more comprehensive exploration of the study of inflaton field quantum fluctuations, refer to Riotto (2017). However, this section aims to present some key results to facilitate an understanding of this process.

The evolution of the fluctuations can be described by perturbing equation (2.8) at linear order. This linear perturbation analysis allows us to understand how small

---

[2] The comoving Hubble radius accounts for the causal connection over one Hubble time and is defined as $r_H = \frac{c}{aH}$.

deviations from equation (2.8) give rise to the observed variations

$$\ddot{\delta\varphi} + 3H\dot{\delta\varphi} - \frac{\nabla^2\delta\varphi}{a^2} = -\frac{\partial^2 V}{\partial\varphi^2}\delta\varphi\,. \tag{2.13}$$

To study the EoM, it is initially convenient to express the fluctuations as a function of the conformal time τ and proceed with the quantization of the field. This approach allows us to consider that

$$\delta\varphi = \frac{\delta\hat{\varphi}}{a}\,, \tag{2.14}$$

therefore, working in Fourier space, one can express the quantum operator $\delta\hat{\varphi}$ as

$$\delta\hat{\varphi}(\boldsymbol{x},\tau) = \int \frac{d^3\boldsymbol{k}}{(2\pi)^3}\left[u_{\boldsymbol{k}}(\tau)\hat{a}_k e^{-i\boldsymbol{k}\cdot\boldsymbol{x}} + u^*_{\boldsymbol{k}}(\tau)\hat{a}^\dagger_k e^{i\boldsymbol{k}\cdot\boldsymbol{x}}\right]\,, \tag{2.15}$$

where $u_{\boldsymbol{k}}$ represents the wave functions associated with the quantum operators $\delta\hat{\varphi}$. The operators $\hat{a}$ and $\hat{a}^\dagger$ [3] correspond to the annihilation and creation operators, respectively. This means that $\hat{a}_{\boldsymbol{k}}|0\rangle = 0$, where $|0\rangle$ is the free vacuum state, and $\langle 0|\hat{a}^\dagger_{\boldsymbol{k}} = 0$. After performing some mathematical steps, we can express the result as follows

$$u''_k(\tau) + \left[k^2 - \frac{a''}{a} + \frac{\partial^2 V}{\partial\varphi^2}a^2\right]u_k(\tau) = 0\,. \tag{2.16}$$

The above equation describes a harmonic oscillator, where the frequency changes in time due to the expansion of the Universe. Particularly, in flat spacetime the solution to the Klein-Gordon equation is

$$u_k \simeq \frac{e^{-iw_k\tau}}{\sqrt{2w_k}}\,, \tag{2.17}$$

here, $w_k^2 = k^2 + m^2$. When dealing with an expanding Universe, the choice of the vacuum state becomes somewhat ambiguous. However, using the equivalence principle, especially involving small scales and short time intervals, we can expect the solution to mimic the behavior in flat Minkowski spacetime, plane waveforms. Consequently, when we locally approximate the spacetime as flat, we can recover the expression (2.17), leading to the following

$$u_k(\tau) \simeq \frac{e^{-ik\tau}}{\sqrt{2k}}\,, \tag{2.18}$$

this choice is referred to as the Bunch-Davies vacuum for a scalar field in curved spacetime. It involves the condition that at small scales we restore the flat case,

---

[3] These operators follow the usual canonical commutation relations: $[\hat{a}_{\boldsymbol{k}}, \hat{a}_{\boldsymbol{k'}}] = 0$ and $[\hat{a}_{\boldsymbol{k}}, \hat{a}^\dagger_{\boldsymbol{k'}}] = (2\pi)^3\delta^3(\boldsymbol{k} - \boldsymbol{k'})$.

specifically when $k \gg aH$.

One approach to solving equation (2.16) is by considering a massless scalar field, $m_\varphi^2 = V''(\varphi) = 0$, in a pure de Sitter spacetime ($H \simeq const$). In this case, the conformal time can be expressed as

$$d\tau = \frac{dt}{a} \leftrightarrow \tau = -\frac{1}{aH}\,, \tag{2.19}$$

as a result, the term $\frac{a''}{a}$ takes the form

$$\frac{a''}{a} = \frac{2}{\tau^2} = \frac{2}{r_H^2}\,. \tag{2.20}$$

Hence, we are interested in solving the equation in two distinct regimes:

Sub-horizon regime: when the comoving wavelength associated with mode k is within the Hubble radius r_H, the following condition holds

$$k \gg aH \longrightarrow u_k'' + k^2 u_k = 0\,, \tag{2.21}$$

this expression represents a harmonic oscillator, describing a plane wave solution. Consequently, it leads to

$$u_k(\tau) = \frac{e^{-ik\tau}}{\sqrt{2k}}\,. \tag{2.22}$$

Super-horizon regime: when the comoving wavelength associated with the mode k exits the Hubble radius, so that

$$k \ll aH \longrightarrow u_k'' - \frac{a''}{a} u_k = 0\,. \tag{2.23}$$

In this regime, the EoM becomes a second-order differential equation whose solution corresponds to a combination of a growing and decaying mode,

$$u_k(\tau) = B(k)a(\tau) + A(k)a^{-2}(\tau)\,, \tag{2.24}$$

as we can observe, the decaying mode becomes negligible very quickly due to the effect of inflation. As a consequence, our focus shifts to the growing one. In this case, determining the amplitude of the fluctuations within this regime involves matching the solutions given by equations (2.22) and (2.24) at the time when k mode exits the horizon (the horizon crossing time), this leads to

$$|\delta\varphi_k| = |B(k)| = \left.\frac{1}{a\sqrt{2k}}\right|_{k=aH} = \frac{H}{\sqrt{2k^3}}\,, \tag{2.25}$$

physically what happens is that the k modes that exit the Hubble radius acquire a "frozen" value given by equation (2.25) because microphysics cannot act on such larger scales. This means that outside the horizon perturbations freeze, and preserve the primordial features until the re-entering of the horizon.

Alternatively, we can also solve the equation (2.16) in a more general case known as Quasi-de Sitter, where ($H \neq const$). For a more in-depth treatment refer to Bartolo et al. (2004). In this case, the value of the quantum fluctuation is given by

$$|\delta\varphi_k| = \frac{H}{\sqrt{2k^3}}\left(\frac{k}{aH}\right)^{\frac{3}{2}-\nu}\,, \tag{2.26}$$

where $\epsilon = \nu - 3/2$, this scale dependence on $k^{-\epsilon}$ is one of the unique prediction of inflationary models.

Up to this point, our focus has been on the study of quantum fluctuations in the inflaton field. Nevertheless, for a complete understanding of how these fluctuations evolve into primordial density perturbations, it is important to also account for perturbations in the metric. As previously mentioned, the inflaton plays a crucial role in the energy distribution of the Universe means that perturbations in the energy-momentum tensor lead to variations in the FLRW metric. Conversely, metric variations influence the evolution of inflaton perturbations, as they are incorporated into the perturbed Klein-Gordon equation. Consequently, the study of both field and metric perturbations is inherently intertwined and needs to be studied together, which is extensively covered in Bartolo et al. (2004). To facilitate this analysis, we use a gauge-invariant[4] quantity known as the *curvature perturbation on uniform energy density hypersurfaces*, denoted as ζ, given by

$$\zeta \equiv -\hat{\Phi} - H\frac{\delta\rho}{\rho}\,, \tag{2.27}$$

which is a "mixed variable" containing both matter and metric perturbations. Such a quantity is the most natural way to study the problem of the perturbations, since

---

[4] In cosmology, a gauge transformation is a map that links points of the background spacetime and of the perturbed spacetime, keeping fixed the coordinates in the background spacetime. This is necessary in order to compare a tensor before and after perturbation because they are defined on different spacetimes unless choosing a one-to-one relationship between the two spaces.

EFE equations themselves couple the metric and the inflaton fluctuations, as we already mentioned. In this expression, $\hat{\Phi}$ represents the Bardeen potential, a crucial parameter related to the scalar metric perturbations that describe spatial variations in the gravitational potential. Besides, it is used to characterize the primordial density fluctuations and their impact on the formation of large-scale structures in the Universe. Additionally, it can be proved that the inhomogeneities generated by the primordial inflaton fluctuations are responsible for producing temperature anisotropies.

Fluctuations in the inflaton field are related to perturbation in the metric and in the expansion rate. In fact, the fluctuations produce variations in the expansion rate in different regions of the Universe on large scales. In particular, this temporal shift can be expressed as

$$\delta t = -\frac{\delta\varphi}{\dot{\varphi}}\,, \tag{2.28}$$

this effect is reflected in fluctuations of the number of e-folds[5] given by

$$\delta N = H\delta t = -H\frac{\delta\varphi}{\dot{\varphi}}\,. \tag{2.29}$$

The previous equation can be written using the equations (2.10), combined with the background equation (2.8) of φ, and the continuity equation (2.5), as a result we obtain that

$$\delta N = -H\frac{\delta\varphi}{\dot{\varphi}} = -H\frac{\delta\rho}{\dot{\rho}}\,. \tag{2.30}$$

Moving on to equation (2.27), the factor $\hat{\Phi}$ can be set equal to zero with a proper choice of gauge (*spatial flat gauge*) leading to

$$\zeta = \delta N = -H\frac{\delta\rho}{\dot{\rho}} = -H\frac{\delta\varphi}{\dot{\varphi}}\,, \tag{2.31}$$

where we can see how the fluctuations of the inflaton field are linked to the perturbation of the energy density. As pointed out before, the quantum fluctuations are frozen out outside the horizon, and at re-entering they generate the density perturbations and temperature fluctuations in the CMB

$$\zeta\big|_{t_{exit}} \simeq -H\frac{\delta\varphi}{\dot{\varphi}} = \zeta\big|_{t_{ent}} \simeq -H\frac{\delta\rho}{\dot{\rho}} = \frac{1}{4}\frac{\delta\rho}{\rho} \sim \frac{\Delta T}{T}\,, \tag{2.32}$$

where we use the fact that $\rho \propto a^{-4} \propto T^4$. This is a simplified model to treat how

---

[5] The number of e-folds is used to quantify the amount of cosmic expansion and it is defined as $N = ln\left(\frac{a(t_f)}{a(t_i)}\right) = \int_{t_i}^{t_f} H dt$

the quantum fluctuations can imprint information in the temperature fluctuations of the CMB, however, it helps us to see the relationship between them.

2.4 Correlation functions

According to the current inflationary paradigm, the origin of primordial density perturbations can be traced back to quantum fluctuations of a scalar field. However, these fluctuations cannot be directly observed. Instead, we rely on a statistical approach to describe their properties.

In this statistical analysis, we consider the observable universe as a stochastic realization within a statistical ensemble of possibilities. In general, to characterize these perturbations statistically, we turn to joint ensemble averages involving a set of N fields, either in real or Fourier space, e.g. Eriksen et al. (2002). These ensemble averages are commonly known as the N-point correlation functions which quantify the correlations between density or temperature perturbations at multiple points in the space and can be defined as follows

$$C_N(\theta_1, ..., \theta_N) = \langle T(\hat{n}_1)T(\hat{n}_2)\cdots T(\hat{n}_N)\rangle \, . \tag{2.33}$$

In the case of Gaussian initial conditions, all the statistical information of the fluctuations is encoded in the two-point correlation function, this is equivalently known as the power spectrum in Fourier space. By contrast, non-Gaussian conditions could be anything else, and higher-order correlation functions can provide useful information about the nature of the fluctuations (Verde et al. 2000; Verde and Heavens 2001).

2.4.1 Power spectrum

The quantum fluctuations can be described by a random field, denoted as $\delta\varphi(\boldsymbol{x}, t)$. Assuming that these fields follow a Gaussian distribution, their statistical properties are primarily characterized by the expectation value, which in this case is $\langle\delta\varphi\rangle = 0$. However, a more interesting description involves computing the covariance, represented by the two-point correlation function.

In accordance with the Cosmological Principle, we make the assumption of statistical homogeneity and isotropy, which implies that the two-point correlation function of these fluctuations in real space can be defined as the ensemble average of the fields at two distinct locations, $\boldsymbol{x}$ and $\boldsymbol{x}+\boldsymbol{r}$ (in comoving coordinates). Consequently, the correlation function only depends on the separation distance r. This leads to

$$\xi(r) \equiv \langle \delta(\boldsymbol{x}+\boldsymbol{r})\delta(\boldsymbol{x})\rangle \,, \tag{2.34}$$

expanding the field in Fourier space, we arrive at the following expression

$$\delta(\boldsymbol{x}) = \int \frac{d^3\boldsymbol{k}}{(2\pi)^3}\, e^{i\boldsymbol{k}\cdot\boldsymbol{x}}\, \delta(\boldsymbol{k}) \,. \tag{2.35}$$

Indeed, as a consequence, the Fourier transform of the two-point correlation can be expressed in terms of the power spectrum $P(k)$, which only depends on the magnitude of the wavevector k, and it measures the amplitude of the fluctuations at a given scale k. Then, we can define that

$$\langle \delta(\boldsymbol{k})\delta(\boldsymbol{k}')\rangle = (2\pi)^3\delta^3(\boldsymbol{k}+\boldsymbol{k}')P(k) \,. \tag{2.36}$$

Furthermore, it is possible to define the dimensionless power spectrum as follows

$$\mathcal{P}(k) = \frac{k^3}{2\pi^2}P(k) \,, \tag{2.37}$$

and the variance can be expressed as follows

$$\langle \delta^2(\boldsymbol{x})\rangle = \int_0^\infty \frac{dk}{k}\mathcal{P}(k) \,. \tag{2.38}$$

In order to proper analyse the dimensionless power spectrum $\mathcal{P}(k)$, we introduce the spectral index n_s, which serves to characterize the shape of the spectrum

$$n_s = \frac{\mathrm{dln}\,\mathcal{P}(k)}{\mathrm{dln}k} \,, \tag{2.39}$$

where n_s represents the spectral index for scalar perturbations. Specifically, when n_s is constant, the adimensional power spectrum can be expressed as a power law

$$\mathcal{P}(k) = \mathcal{P}_0(k)\left(\frac{k}{k_0}\right)^{n_s-1} \,, \tag{2.40}$$

here, k_0 is a pivot scale, often chosen as $k_0 = 0.05$ Mpc^{-1}, while $\mathcal{P}_0(k)$ denotes the amplitude evaluated at this pivot scale. When $n_s = 1$, the expression becomes independent of k and is known as the Harrison-Zel'dovic spectrum.

The actual value determined by Akrami et al. (2020c) is $n_s = 0.9649 \pm 0.0042$ at 68 % CL in the case of single-field slow-roll inflation.

2.5 Non-gaussianity

Non-Gaussianity stands as a crucial feature in cosmology, offering valuable insights into the underlying processes during the early epochs of the Universe. While our current observations align with the idea of scale-invariant perturbations, described by almost Gaussian statistics, where the power spectrum encapsulates all the statistical information, it is essential to acknowledge that deviations from pure Gaussian behavior remain a viable and intriguing possibility.

The existence of some degree of non-Gaussianity within the primordial cosmological perturbation field constitutes a broad prediction shared by various cosmological scenarios (Verde et al. 2001; Maldacena 2003; Bartolo et al. 2005; Jung et al. 2023). Moreover, it is worth noting that non-Gaussian signatures and their specific shape are significant model dependent, which makes primordial non-Gaussianity (PNG) a powerful tool to constrain inflation and to provide information about physics at very high energy scales in the early Universe.

For instance, non-Gaussianity serves as an indicator of intriguing phenomena in the Universe, suggesting the presence of non-linear interactions, asymmetry, or higher-order dependencies. These features can be attributed to alternative models such as warm inflation, curvature mechanism, ghost inflation, or even string theory, a more thorough discussion can be found in Linde and Mukhanov (1997); Gupta et al. (2002); Lyth et al. (2003); Bartolo et al. (2004).

The standard approach to quantifying non-Gaussianity involves analyzing higher-order correlation functions, such as the three-point correlation function (referred to as bispectrum in Fourier space, see e.g. Verde et al. (2000); Wang and Kamionkowski 2000; Babich et al. 2004; Akrami et al. 2020a) or the four-point correlation function (trispectrum). These functions capture statistical relationships beyond simple pair-wise correlations. In particular, they can reveal complex patterns in the data. In general, we can define the Fourier transform of the N-point correlation functions of the primordial curvature fluctuation using the following expression

$$\langle \zeta_{\boldsymbol{k}_1} \zeta_{\boldsymbol{k}_2} ... \zeta_{\boldsymbol{k}_N} \rangle = (2\pi)^3 \delta^3(\boldsymbol{k}_{12...N}) F_\zeta(\boldsymbol{k}_1, \boldsymbol{k}_2, ..., \boldsymbol{k}_N) \,, \tag{2.41}$$

in this expression, all the essential information regarding the amplitude and shape of the primordial non-Gaussianity is encoded in the function $F_\zeta(\boldsymbol{k}_1, \boldsymbol{k}_2, ..., \boldsymbol{k}_N)$. A crucial observable for the study of PNG is the CMB since it originated at early times when perturbations remained in the linear regime, ensuring the preservation of their statistical characteristics. Currently, the most precise result in this field has been obtained through the analysis of Planck CMB data. This has yielded an upper bound on the level of PNG, measuring at roughly less than 0.1 % of the amplitude of the Gaussian component of the field Akrami et al. (2020a).

2.5.1 Primordial Trispectrum

The simplest indicator sensible to non-Gaussianity is the 3-point correlation function of the primordial curvature perturbation ζ. However, recent investigations into this issue of the initial perturbations have focused on the Fourier equivalent of the 4-point correlation function, the trispectrum. This statistical quantity allows us to study correlations among four Fourier modes, which represent the wavevectors of the curvature perturbations. The trispectrum is formally defined as

$$\langle \zeta_{\boldsymbol{k}_1} \zeta_{\boldsymbol{k}_2} \zeta_{\boldsymbol{k}_3} \zeta_{\boldsymbol{k}_4} \rangle_c = (2\pi)^3 \delta^3(\boldsymbol{k}_1 + \boldsymbol{k}_2 + \boldsymbol{k}_3 + \boldsymbol{k}_4) T_\zeta(\boldsymbol{k}_1, \boldsymbol{k}_2, \boldsymbol{k}_3, \boldsymbol{k}_4)\,, \tag{2.42}$$

in this equation, $T_\zeta(\boldsymbol{k}_1, \boldsymbol{k}_2, \boldsymbol{k}_3, \boldsymbol{k}_4)$ represents the primordial trispectrum, with homogeneity being accounted by the presence of the Dirac delta. When we analyze this function, we expect the wavevectors to form a closed quadrilateral configuration. Notably, both the amplitude and shape of the trispectrum are model-dependent. Consequently, predictions regarding these characteristics provide a valuable tool for distinguishing among different inflationary scenarios.

Among the most widely used models for introducing non-gaussianity are the *local type non-Gaussian models*, where non-linear contributions of the perturbations on super-horizon scales give rise to non-Gaussian behavior. These models have been extensively studied, as referenced in the literature Okamoto and Hu (2002); Bartolo et al. (2004); Byrnes (2014). In these models, the Bardeen's curvature potential Φ in the matter-dominant era is expressed as a local function of a Gaussian field Φ_G and is often expanded into a Taylor series as (e.g. Nishimichi 2012)

$$\Phi(\boldsymbol{x}) = \Phi_G(\boldsymbol{x}) + f_{NL}\left[\Phi_G^2(\boldsymbol{x}) - \langle \Phi_G^2 \rangle\right] + g_{NL}\,\Phi_G^3(\boldsymbol{x}) + \dots\,, \tag{2.43}$$

In real space, the cubic-order contribution is often parametrized in terms of the curvature perturbation ζ as

$$\zeta(\boldsymbol{x}) = \zeta_G(\boldsymbol{x}) + \frac{9}{25} g_{NL}\,\zeta_G^3(\boldsymbol{x})\,. \tag{2.44}$$

In this context, the trispectrum in the local non-Gaussian model can be expressed as follows

$$T_\zeta(\boldsymbol{k}_1, \boldsymbol{k}_2, \boldsymbol{k}_3, \boldsymbol{k}_4) = \frac{54}{25}\, g_{NL}^{local}\, [P_\zeta(k_1) P_\zeta(k_2)\, P_\zeta(k_3) + 3\, perm.] \,. \tag{2.45}$$

In their analyses, Akrami et al. (2020a) found that the local-type trispectrum described in equation (2.45) is consistently negligible in the context of single-field inflation as discussed by Senatore and Zaldarriaga 2012b. However, it can have a significantly large value in multi-field models of inflation, where the presence of a large bispectrum is forbidden by symmetry as noted in Senatore and Zaldarriaga 2012a. Additionally, other scenarios were explored including $g_{NL}^{\dot{\sigma}^4}$ and $g_{NL}^{(\partial\sigma)^4}$, which can be generated by operators in the effective field theory (EFT) of inflation. Currently, the trispectrum constraint provided by Planck stands at $g_{NL} = (-5.8 \pm 6.5) \times 10^4$ at the 68% CL.

Subsequently, extensive research has been undertaken to establish constraints on the amplitude and shape of primordial non-Gaussianity using the trispectrum, such as the works by Regan et al. 2010, Mizuno and Koyama 2010, Regan et al. 2015, Smith et al. 2015, and Feng et al. 2015.

When considering the trispectrum shape, which encodes information about the distribution of power across various configurations, the most frequently examined shape in the literature is the *local shape*. This shape describes a trispectrum that remains relatively constant across different configurations of the four k modes. Other notable templates include the *equilateral shape*, characterized by four k modes with similar magnitudes and approximately equal angles between them, the *orthogonal shape*, where the signal is enhanced when the k modes align in specific patterns, and the *enfolded shape*, which arises from folded or looped configurations resulting in non-Gaussian signatures, a comprehensive discussion of these possible trispectrum shapes can be found in the works of Chen et al. 2009, Bartolo et al. 2010, Regan et al. 2010 and Akrami et al. (2020a).

It is important to highlight that these various shape templates are associated with different inflationary models. Consequently, a thorough characterization of the trispectrum proves valuable in distinguishing among several inflationary scenarios.

2.5.2 Shape of the primordial trispectrum

In this section, we aim to illustrate how it is possible to derive the shape of the trispectrum using the approach proposed by Chen et al. (2009), which was subsequently implemented in Bartolo et al. (2010). In their work Chen et al. (2009)

calculated large scalar four-point correlation functions within the framework of general single-field inflation models. They found that the leading order trispectra exhibits four distinct shapes, enabling differentiation between them and the trispecta of the local form. They also proposed a methodology for computing these different shapes, including the local trispectrum. In this discussion, we will specifically follow this approach for the local trispectrum case considering only the cubic-order contribution.

We focus our attention on the trispectrum in the local form. This is obtained from the ansatz in real space

$$\zeta(\boldsymbol{x}) = \zeta_G + \frac{3}{5} f_{NL} \left(\zeta_G^2 - \langle\zeta_G^2\rangle\right) + \frac{9}{25} g_{NL} \left(\zeta_G^3 - 3\langle\zeta_G^2\rangle\zeta_G\right) . \tag{2.46}$$

This particular form arises in multi-field models, where the large non-Gaussianities are generated from isocurvature modes at super-horizon scales. The resulting trispectrum is given by

$$\mathcal{T} = f_{NL}^2 \, T_{loc1} + g_{NL} \, T_{loc2} \, , \tag{2.47}$$

where we introduce T_{loc1} and T_{loc2} which are associated with the specific shape. Particularly, we focus on the cubic contribution that involves the g_{NL} parameter where T_{loc2} is defined as follows

$$T_{loc2} = \frac{27}{100} \sum_{i=1}^{4} k_i^3 \, . \tag{2.48}$$

Before delving into the discussion of the shape function, we note that the arguments of this function are the four momenta k_1, k_2, k_3, k_4. For the configuration to form a tetrahedron as in figure 2.3, the following conditions are required:

Firstly, we define three angles at one vertex as follows

$$\cos\alpha = \frac{k_1^2 + k_{14}^2 - k_4^2}{2k_1 k_{14}} \, , \tag{2.49}$$

$$\cos\beta = \frac{k_2^2 + k_{14}^2 - k_3^2}{2k_2 k_{14}} \, , \tag{2.50}$$

$$\cos\gamma = \frac{k_1^2 + k_2^2 - k_{12}^2}{2k_1 k_2} \, , \tag{2.51}$$

these angles should satisfy that

$$1 - \cos^2\alpha - \cos^2\beta - \cos^2\gamma + 2\cos\alpha\cos\beta\cos\gamma \geq 0 \, . \tag{2.52}$$

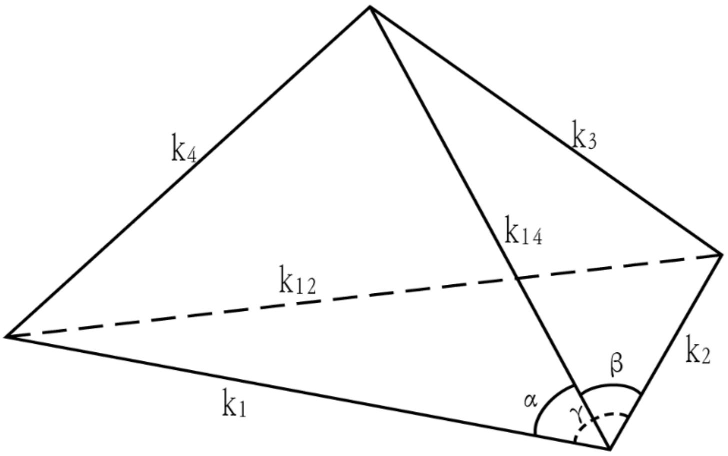

Figure 2.3: Schematic representration of the tetrahedron considered by Chen et al. (2009) in terms of the wavevectors k$_1$, k$_2$, k$_3$, k$_4$, two diagonals k$_{12}$, k$_{14}$ and a set of three angles α, β and γ.

Secondly, the four momenta should satisfy all the triangle inequalities

$$k_1 + k_4 > k_{14}\,;\; k_1 + k_2 > k_{12}\,;\; k_2 + k_3 > k_{14}\,, \tag{2.53}$$

$$k_1 + k_{14} > k_4\,;\; k_1 + k_{12} > k_2\,;\; k_2 + k_{14} > k_3\,, \tag{2.54}$$

$$k_4 + k_{14} > k_1\,;\; k_2 + k_{12} > k_1\,;\; k_3 + k_{14} > k_2\,, \tag{2.55}$$

the last triangle inequality (k_3, k_4, k_{12}) is always satisfied given equations (2.52) and (2.55).

These conditions are explored in various limits:

Equilaterial limit: $k_1 = k_2 = k_3 = k_4$.

Folded limit: $k_{12} = 0$ and $k_1 = k_2$, $k_3 = k_4$.

Specialized planar limit: $k_1 = k_3 = k_{14}$ and one can solve for k_{12} that

$$k_{12} = \left[k_1^2 + \frac{k_2 k_4}{2k_1^2}\left(k_2 k_4 + \sqrt{(4k_1^2 - k_2^2)(4k_1^2 - k_4^2)}\right)\right]^{1/2}\,. \tag{2.56}$$

In figure 2.4, we have depicted the shape function T_{loc2} in the equilateral limit, where $k_1 = k_2 = k_3 = k_4$ with a fixed value of $k_1 = 1$. The diagonals k_{12} and k_{14} vary within the range of 0 to 2. Notably, it is observed that T_{loc2} remains independent of both k_{12} and k_{14}. While, in figure 2.5, we have presented the folded limit of the shape function. Here, we have kept $k_1 = 1$ fixed, while allowing k_4 to vary within the range of 0 to 1, and the diagonal k_{14} within the range of 0 to 2. In particular, in the folded limit we have assumed $k_4 < k_1$ without losing generality. Note also that

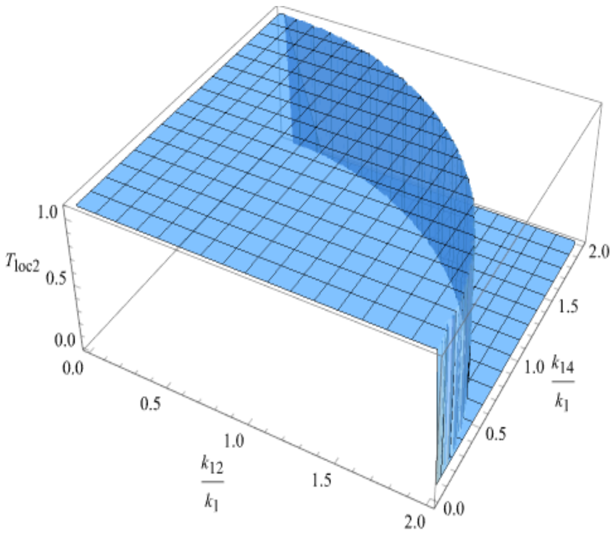

Figure 2.4: Plot of the shape function T_{loc2} in the equilateral limit, where $k_1 = k_2 = k_3 = k_4$, because there is no k_{12}, k_{14} dependence one gets a plateau.

T_{loc2} does not vanish in the limit where $k_4 \to 0$.

In the work of Chen et al. (2009), other cases were investigated, including the specialized planar limit see figure 2.5, where $k_1 = k_3 = k_{14}$, and the near double-squeezed limit, where $k_3 = k_4 = k_{12}$, resulting in a tetrahedron resembling a planar quadrangle. Additionally, in the specialized planar limit, we observe that the shape function T_{loc2} is non-vanishing. It is worth noting that the figures presented in this section align closely with the findings reported in the referenced paper.

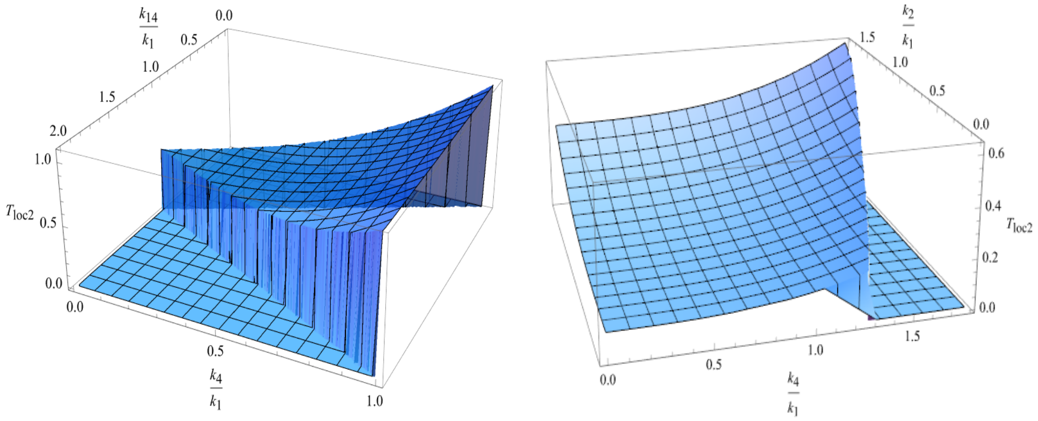

Figure 2.5: Shape function T_{loc2} in two different limits. The plot on the left shows the function in the folded limit ($k_1 = k_2$, $k_3 = k_4$ and $k_{12} = 0$), while on the right the specialized planar limit ($k_1 = k_3 = k_{14}$) is presented.

Chapter 3

The Cosmic Microwave Background

One of the observational pillars of our knowledge of the Universe and its evolution is the Cosmic Microwave Background (CMB) radiation. It is so rich that an enormous amount of observational data and constraints have been obtained from it. Hence, since its discovery it has been many efforts to elucidate its origin and main characteristics.

The existence of the CMB was theorized by George Gamow in 1948 as a test for his theory of the HBB. This faint radiation consists of photons emitted when the Universe became transparent to light at the recombination epoch about 380.000 years after the BB. It was discovered by Penzias and Wilson in 1965 when they detected an incredibly uniform and isotropic signal coming from all over the sky.

The CMB radiation is well-described by a blackbody spectrum with a mean temperature of $T_0 = 2.725$K. Subsequent measurements of its spectrum by the Cosmic Background Explorer (COBE), the Wilkinson Microwave Anisotropy Probe (WMAP), and Planck have revealed also smaller temperature anisotropies $\Delta T/T \sim 10^{-5}$, which deeply impacted on our understanding of the evolution of cosmic structures. Studying the CMB has revolutionized our comprehension of the universe's origins and structure. Moreover, it has confirmed the Big Bang theory's predictions and supported the cosmic inflation concept.

3.1 Origin of the Temperature Anisotropies

The standard cosmological scenario explaining the history of the cosmos involves an inflationary epoch, followed by a reheating phase where the inflaton field begins to oscillate around the minimum of its potential and subsequently decays into lighter relativistic particles. This process culminates with the efficient thermalization of the Universe, making the beginning of the radiation-dominated era.

It has been observed that the CMB spectrum aligns closely with that of a near-perfect blackbody. This correspondence reveals an almost complete level of thermalization between matter and radiation during its production. According to this in the early times, baryons and photons were tightly coupled, with photons having a significantly small mean free path which ensures a continuous scattering by free electrons, thereby promoting thermal equilibrium. The predominant interaction mechanism between electrons and photons during this phase is Compton scattering, along with its non-relativistic counterpart, the Thomson scattering, given by

$$e^- + \gamma \leftrightarrow e^- + \gamma\,.$$

Eventually, the Universe cooled down sufficiently, enabling recombination to occur, which allowed the formation of neutral hydrogen. During this period, protons and electrons became bound together, leading to a decrease in the efficiency of the scattering process. As a result, matter decoupled from radiation, and photons began to propagate freely through space. These photons reach us today, composing the Cosmic Microwave Background radiation (CMB), as depicted in figure 3.1. The CMB radiation appears to originate from a uniform spherical surface around the observer, known as the *Last Scattering Surface* (LSS). This surface is placed at a redshift of approximately $z_{rec} \approx 1100$, and the radius of this shell corresponds to the distance each photon has traveled since its last scattering at the recombination epoch.

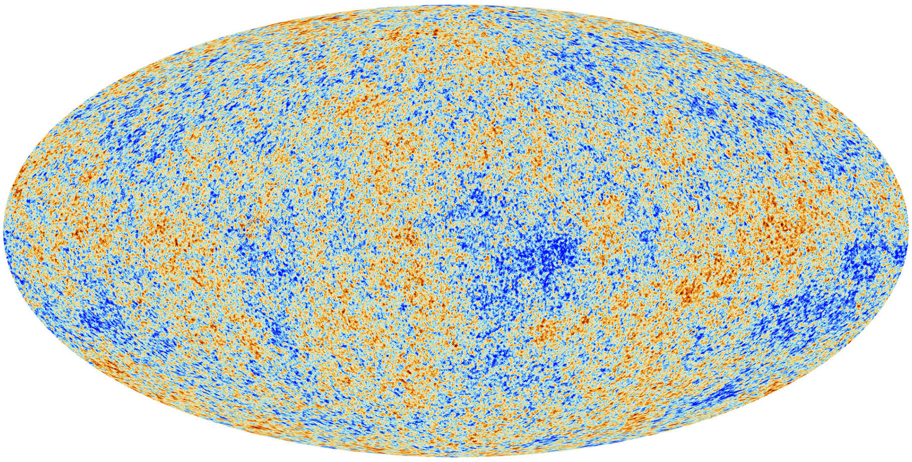

Figure 3.1: Map of the CMB temperature anisotropies by the Planck observatory. Taken from ESA and the Planck Collaboration.

The origin of the temperature anisotropies illustrated in Figure 3.1 is closely tied to the initial quantum fluctuations that existed during the inflationary epoch. Specifically, these super-horizon fluctuations generated the primordial curvature perturbation denoted as ζ, which carries the information about the scalar density perturbations $\delta\rho$ and primordial potentials Φ at early times. Consequently, the properties of the CMB radiation are inherited from this primordial curvature perturbation ζ. Looking back to the time before recombination, when the cosmological plasma consisted of a tightly coupled photon-baryon fluid, we can explain almost completely the anisotropy features of the CMB by analyzing the behavior of this fluid.

Two types of anisotropies are distinguished: primary anisotropies arising from processes back to the time of recombination, and secondary anisotropies generated by the interaction of CMB photons with cosmic structures, changing their properties along the line of sight. The presence of the primary anisotropies can be attributed to three fundamental effects: the interaction of photons with gravitational potential wells at large angular scales (Sachs-Wolfe effect), the evolution of the photon-baryon fluid, and Compton scattering at smaller scales (Silk damping).

The secondary anisotropies, on the other hand, emerge from various effects that modify the properties of CMB photons. These mechanisms include variations in the gravitational potential on large scales along the photon's path (Rees-Sciama effect and Integrated Sachs-Wolfe effect). Additionally, other processes involve the scattering between CMB photons and free electrons, such as the Sunyaev-Zel'dovich (SZ) effect, Ostriker-Vishniac (OV) effect, and inhomogeneous reionization. For an in-depth review of all these phenomena, refer to Sachs and Wolfe (1967); Silk (1967); Peebles and Yu (1970); Sunyaev and Zeldovich (1970); Aghanim et al. (2008).

In order to gain a comprehensive grasp of the physics underlying CMB anisotropies, it is convenient to study the two-point correlation function or angular power spectrum, which we will delve into in the upcoming section.

3.2 CMB Angular Power Spectrum

In Chapter 2, we discussed the standard methodology used to establish the connection between theoretical predictions and observational data. For the case of CMB radiation, its primary observable is the intensity as a function of frequency and direction on the sky denoted as $\hat{\boldsymbol{n}}$. Additionally, the CMB spectrum closely resembles that of a blackbody with nearly constant temperature across the entire sphere. Due to this characteristic, the temperature field is commonly described in terms of the temperature fluctuations, denoted as $\theta(\hat{\boldsymbol{n}}) = \Delta T/T$. Consequently, we can further expand this field into spherical harmonics, represented by Y_{lm}, as follows

$$\theta(\hat{\boldsymbol{n}}) = \frac{\Delta T}{T}(\hat{\boldsymbol{n}}) = \sum_{l=0}^{\infty} \sum_{m=-l}^{l} a_{lm} \, Y_{lm}(\hat{\boldsymbol{n}}) \, , \tag{3.1}$$

here, $\hat{\boldsymbol{n}}$ represents the coordinates of the temperature measurements across the sky, and a_{lm} are the coefficients of this expansion, carrying information about the amplitude of the CMB map within an angular aperture of $\theta \sim l^{-1}$. To express the a_{lm} coefficients in terms of the temperature anisotropies, we make use of the orthogonality property intrinsic to spherical harmonics,

$$a_{lm} = \int d\Omega(\hat{\boldsymbol{n}}) \, Y^*_{lm}(\hat{\boldsymbol{n}})\theta(\hat{\boldsymbol{n}}) \, , \tag{3.2}$$

as a result, all the statistics of the temperature field are encompassed within the multiple coefficients a_{lm}. It is important to note that while the theoretical model does not predict the specific values of a_{lm}, it does provide information about their distribution.

As already pointed out, the density perturbations responsible for the temperature anisotropies originate during inflation. In the context of the simplest inflationary model, quantum fluctuations exhibit an almost Gaussian distribution. Consequently, we expect that the multiple coefficients will follow the same statistical distribution. This leads to an expected mean value of $\langle a_{lm} \rangle$ being zero, for this reason, the variance C_l carries all the statistical information

$$\langle a_{lm} a^*_{l'm'} \rangle = \delta_{ll'} \delta_{mm'} C_l \, , \tag{3.3}$$

this expression is analogous to the definition of the power spectrum equation 2.36, although in this context, it is referred to as the *angular power spectrum*. Observe that for a given value of l, the a_{lm} coefficients have their own variance. Furthermore, when considering a specific value of l, there exist $2l+1$ individual values for the a_{lm} coefficients. A more practical definition of C_l is provided by

$$C_l = \frac{1}{2l+1} \sum_{m=-l}^{l} \langle |a_{lm}|^2 \rangle \, . \tag{3.4}$$

Moreover, an inherent uncertainty affects the angular power spectrum, imposing limitations on its precision. The *cosmic variance* arises from the fact that we have only one realization of our Universe. The definition of cosmic variance is

$$\left(\frac{\Delta C_l}{C_l}\right) = \sqrt{\frac{2}{2l+1}}\,, \tag{3.5}$$

the cosmic variance diminishes as the value of l increases and escalates as l decreases, directly impacting the larger scales that are associated with the inflationary period.

On the other hand, it is advantageous to derive an expression for the multiple coefficients in terms of the curvature perturbation ζ, which allows us to compare the theoretical predictions of a given inflationary model with the observational data. Notably, equation (3.2) highlights the dependence of the a_{lm} coefficients on the anisotropic temperature field $\theta(\hat{\boldsymbol{n}})$ and it is widely accepted that the characteristics of the temperature field stem from several physical processes associated with quantum fluctuation that emerged during inflation and the subsequent evolution of the photons until today. To account for all the processes influencing the temperature field, it is customary to work in Fourier space. Particularly, when considering the Sach-Wolfe approximation, the dominant contribution to temperature fluctuations on large scales is the gravitational potential fluctuation. Hence, at the decoupling time (t_*), we define that the temperature fluctuations are related to the gravitational potential through the relation

$$\frac{\Delta T}{T} \sim \frac{1}{3}\Phi_*\,. \tag{3.6}$$

In equation (3.2), we can represent the temperature fluctuation field in Fourier space as follows

$$\begin{aligned} a_{lm} &= \frac{1}{3}\int d\Omega(\hat{\boldsymbol{n}})\, Y^*_{lm}(\hat{\boldsymbol{n}})\Phi_*(\hat{\boldsymbol{n}})\,, \\ &= \frac{1}{3}\int d\Omega(\hat{\boldsymbol{n}})\, Y^*_{lm}(\hat{\boldsymbol{n}}) \int \frac{d^3\boldsymbol{k}}{(2\pi)^3}\, e^{i\boldsymbol{x}\cdot\boldsymbol{k}}\Phi_*(\boldsymbol{k})\,, \end{aligned} \tag{3.7}$$

the exponential term can be expanded into a sum of spherical Bessel functions j_l through the implementation of the Rayleigh plane wave expansion

$$e^{i\boldsymbol{k}\cdot\boldsymbol{x}} = 4\pi \sum_{lm} i^l\, j_l(kr_*)\, Y^*_{lm}(\hat{\boldsymbol{k}})\, Y_{lm}(\hat{\boldsymbol{n}})\,, \tag{3.8}$$

where r_* is the distance from the last scattering surface, so that $x = r_*\,\hat{\boldsymbol{n}}$. Substituting the aforementioned expression into (3.7), we derive

$$a_{lm} = \frac{4\pi}{3}\, i^l \int \frac{d^3\boldsymbol{k}}{(2\pi)^3}\Phi_*(\boldsymbol{k}) j_l(kr_*) Y^*_{lm}(\hat{\boldsymbol{k}})\,. \tag{3.9}$$

Accounting for all the physical mechanisms to explain the CMB anisotropic radiation requires the introduction of the transfer function $\Delta_l(k)$. Specifically, within the Sach-Wolfe approximation, $\Delta_l(k) \sim j_l(kr_*)/3$. The transfer function provides insight into the post-recombination physical phenomenon and is computed through the solution of the Boltzmann-Einstein equations [1]. Consequently, equation (3.9) takes the form

$$a_{lm} = 4\pi\, i^l \int \frac{d^3\boldsymbol{k}}{(2\pi)^3}\, \Phi(\boldsymbol{k})\, \Delta_l(k)\, Y^*_{lm}(\hat{\boldsymbol{k}})\,. \tag{3.10}$$

Furthermore, when considering first-order perturbations, we assume that during the matter-dominated era at the time of decoupling, the gauge-invariant curvature perturbation ζ is linked to the Bardeen potential (primordial gravitational potential) Φ in the following manner

$$\Phi = -\frac{3}{5}\,\zeta\,, \tag{3.11}$$

by substituting the previous relation into (3.10), we establish a connection between a_{lm} coefficients and the curvature perturbation through the following expression

$$a_{lm} = -\frac{12\pi}{5}\, i^l \int \frac{d^3\boldsymbol{k}}{(2\pi)^3}\, \zeta(\boldsymbol{k})\, \Delta_l(k)\, Y^*_{lm}(\hat{\boldsymbol{k}})\,. \tag{3.12}$$

At this point, we can proceed to explicitly calculate the angular power spectrum

$$\begin{aligned}\langle a_{lm} a^*_{l'm'}\rangle &= (4\pi)^2 \int \frac{d^3\boldsymbol{k}}{(2\pi)^3}\frac{d^3\boldsymbol{k'}}{(2\pi)^3}\,(i)^{l-l'}\langle\Phi(\boldsymbol{k})\Phi(\boldsymbol{k'})\rangle\Delta_l(k)\Delta^*_{l'}(k')Y^*_{lm}(\hat{\boldsymbol{k}})Y_{l'm'}(\hat{\boldsymbol{k}}')\\ &= (4\pi)^2 \int \frac{d^3\boldsymbol{k}}{(2\pi)^3}\,(i)^{l-l'}\,P_\Phi(k)\,\Delta_l(k)\Delta^*_{l'}(k)Y^*_{lm}(\hat{\boldsymbol{k}})Y_{l'm'}(\hat{\boldsymbol{k}})\\ &= \delta_{ll'}\delta_{mm'}C_l\,,\end{aligned} \tag{3.13}$$

in this derivation, we have used the orthonormality relation of spherical harmonics to simplify the expression. Additionally, we establish the definition that the temperature angular power spectrum is expressed as

$$C_l = \frac{2}{\pi}\int dk\, k^2\, P_\Phi(k)\, |\Delta_l(k)|^2\,. \tag{3.14}$$

Figure 3.2 illustrates the theoretical prediction for the temperature angular power

---

[1] The Boltzmann equation tells us how the distribution function of some particle species evolves in time, is given by

$$\frac{df}{d\lambda} = C(f)\,,$$

where λ is an affine parameter along a trajectory and C is the collision term which contains information about interactions.

spectrum (blue solid line) alongside the current observational data (red dots), acquired from the Planck Satellite. Notably, the observational data align with the best-fit model ΛCDM. Additionally, it is worth noting that the plotted quantity is $D_l = l(l+1)C_l/2\pi$, an auto-spectrum that indicates the approximate contribution per logarithmic interval of multipoles centered around l to the variance of the fluctuation.

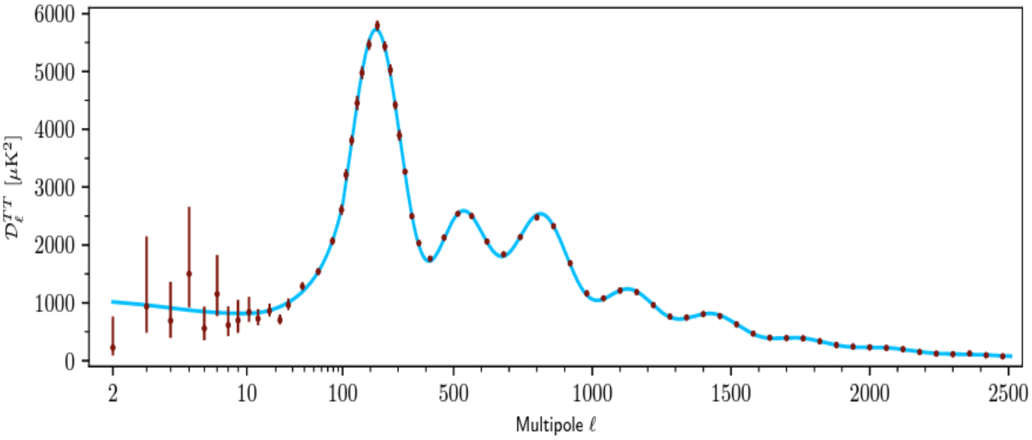

Figure 3.2: Planck CMB power spectra. Notice that the large scales have a significant error bar due to the effect of cosmic variance. Credit: ESA and the Planck Collaboration Aghanim et al. (2020).

Furthermore, the power spectrum exhibits three distinct features: the Sachs-Wolfe plateau ($2 \leq l \leq 30$), the acoustic peaks ($30 \leq l \leq 1500$), and the damping tail ($l \geq 1500$).

At the largest angular scales (low l), the primary driver of intensity fluctuations is attributed to extensive gravitational potential perturbations existing within the LSS during recombination. The gravitational effect arises from the fact that photons must exit the maxima or minima of the potential associated with these perturbations. When only the SW effect is dominant, the spectrum remains invariant across varying angular scales.

As mentioned previously, on these larger scales, gravity exclusively operates within the linear regime, and there are no reaction effects, such as those stemming from pressure. Nonetheless, pressure contributions manifest on intermediate and smaller angular scales. In these regions of the spectrum, photon and baryon dynamics are dominant. Prior to decoupling, the photon-baryon fluid responds to the gravitational influence of Dark Matter. As the fluid encounters a potential well, it starts to fall toward the well. However, under the influence of gravity, the compression of the photon-baryon fluid leads to a pressure counteracting the gravitational force. Subsequently, the fluid expands outward. As this expansion proceeds, pressure diminishes, causing gravity to prompt the fluid to fall inward again. This cyclic inward-outward motion of the fluid constitutes *acoustic oscillations*, which represent standing sound waves Ryden (2016). These oscillations impact the matter and energy distribution, yielding overdense regions (compressions) and underdense regions (rarefactions) in the plasma. Additionally, due to the Doppler effect, the photons become either cooler or hotter than the average temperature, depending on the motion of the photon-baryon fluid at the time of decoupling.

Following recombination, the photons in the CMB occasionally interact with free electrons, resulting in intermittent diffusion or damping of the temperature fluctuations on smaller scales. This process, known as Silk damping, leads to the attenuation of temperature anisotropies, evident in the presence of the tail observed in the power spectrum.

The significance of the CMB cannot be overstated. The correct understanding of all the underlying physical processes from its formation in the early times until the present day provides us with a plethora of insights into the properties of our Universe. The distinct pattern of peaks and troughs exhibited in figure 3.2 corresponds to fluctuations in the energy-density in the early Universe. These patterns enable us to extract various cosmological parameters, including the abundances of Dark Matter and Dark Energy, the spatial curvature, the Hubble constant, the spectral index of primordial fluctuations, and other crucial characteristics of the early Universe.

On the other hand, the CMB power spectrum serves as a fundamental tool for the analysis of observational data, encapsulating the entire statistical information of the CMB under the assumption that the initial quantum fluctuations adhere to a Gaussian distribution. Nevertheless, the potential exists for certain physical mechanisms to induce non-Gaussian features, leaving an imprint on the CMB radiation. To explore non-Gaussianity, we use higher-order correlation functions. In this work, our attention centers on the four-point correlation function, or its Fourier counterpart, known as the trispectrum.

3.3 CMB Trispectrum

The four-point correlation function, or trispectrum in Fourier space, plays a crucial role in the exploration of non-Gaussianity. It measures the degree of correlation among temperature fluctuations at four distinct points across the CMB sky, as depicted in figure 3.3. More precisely, it quantifies how much the temperature at one point tends to be higher or lower when the temperatures at the other three points have specific values.

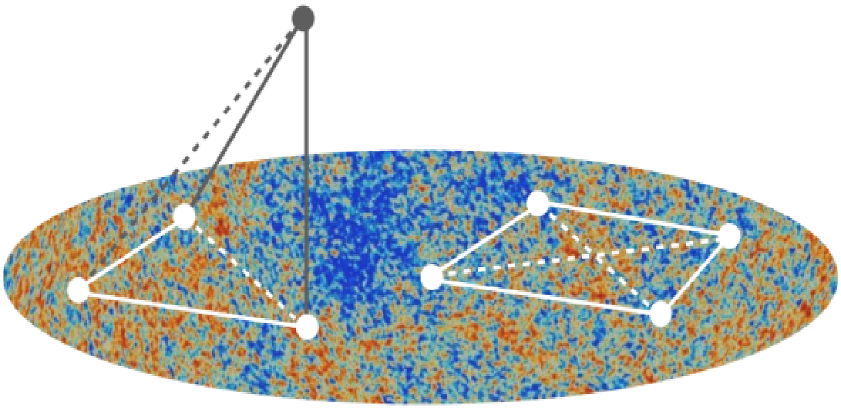

Figure 3.3: Schematic representation of the three-point correlation function (bispectrum, in Fourier space) and the four-point correlation function (trispectrum) in the CMB map. Taken from Kalaja et al. (2021).

Hence, the CMB trispectrum constitutes the connected part of the four-point correlation function of the a_{lm} coefficients in Fourier space and incorporates non-Gaussian statistics. Adhering to the formalism outlined in Hu (2001) and Okamoto and Hu (2002), the trispectrum can be defined as,

$$T_{l_1m_1l_2m_2l_3m_3l_4m_4} = \langle a_{l_1m_1}a_{l_2m_2}a_{l_3m_3}a_{l_4m_4}\rangle_c \,, \tag{3.15}$$

thus exploiting equation (3.10), which elucidates that the primordial potential Φ induces the multipole moments a_{lm} through a convolution involving the transfer functions $\Delta_l(k)$. As a result, the following expression is derived

$$\begin{aligned}\langle a_{l_1m_1}a_{l_2m_2}a_{l_3m_3}a_{l_4m_4}\rangle_c = (4\pi)^4\,(-i)^{\sum_i l_i}\int \frac{d^3\boldsymbol{k}_1 d^3\boldsymbol{k}_2 d^3\boldsymbol{k}_3 d^3\boldsymbol{k}_4}{(2\pi)^{12}}\Delta_{l_1}(k_1)\Delta_{l_2}(k_2)\times\\ \Delta_{l_3}(k_3)\Delta_{l_4}(k_4)\langle\Phi(\boldsymbol{k}_1)\Phi(\boldsymbol{k}_2)\Phi(\boldsymbol{k}_3)\Phi(\boldsymbol{k}_4)\rangle_c Y^*_{l_1m_1}(\hat{\boldsymbol{k}}_1)Y^*_{l_2m_2}(\hat{\boldsymbol{k}}_2)Y^*_{l_3m_3}(\hat{\boldsymbol{k}}_3)Y^*_{l_4m_4}(\hat{\boldsymbol{k}}_4)\,,\end{aligned} \tag{3.16}$$

where $k_i = |\boldsymbol{k}_i|$ represents the magnitude of the wavevector and the subscript c denotes the connected component. By employing the definition of the primordial trispectrum as presented in equation (2.42), and making the assumption of a statistically isotropic trispectrum that only depends on the magnitude of the wavevector, the so-called diagonal-free trispectra, we obtain that

$$T_{l_1m_1l_2m_2l_3m_3l_4m_4} = \int d\Omega(\hat{\boldsymbol{n}}) Y_{l_1m_1}(\hat{\boldsymbol{n}}) Y_{l_2m_2}(\hat{\boldsymbol{n}}) Y_{l_3m_3}(\hat{\boldsymbol{n}}) Y_{l_4m_4}(\hat{\boldsymbol{n}})\, t^{l_1l_2}_{l_3l_4}\,, \tag{3.17}$$

where $t^{l_1l_2}_{l_3l_4}$ is referred to as the extra-reduced trispectrum (as discussed in Fergusson et al., 2010). Subsequently,

$$t^{l_1l_2}_{l_3l_4} = \left(\frac{2}{\pi}\right)^4 \int r^2\, dr \int (k_1k_2k_3k_4)^2 T_\Phi(k_1,k_2,k_3,k_4) \Delta_{l_1}(k_1)\Delta_{l_2}(k_2)\Delta_{l_3}(k_3)\Delta_{l_4}(k_4) \times j_{l_1}(k_1r) j_{l_2}(k_2r) j_{l_3}(k_3r) j_{l_4}(k_4r)\,. \tag{3.18}$$

By analyzing the trispectrum of the CMB, diverse inflationary models can be tested, and insights into the physics governing the early Universe can be constrained. However, the study of the CMB trispectrum involves complex tasks requiring sophisticated data analysis techniques. Notice that the aforementioned expression explicitly establishes the direct connection between the CMB trispectrum and the four-point correlation of the primordial potential Φ, which originates from the inflationary epoch. Particularly, equation (3.18) was derived under the presumption of a diagonal-free trispectrum of the primordial potential. It is important to acknowledge that several ways exist to define the trispectrum of Φ. To offer a more comprehensive approach, we explore the case of the local non-Gaussian model in the subsequent section.

3.3.1 Trispectra in the local non-Gaussian model

Based on the formalism established by Okamoto and Hu (2002), we are enabled to calculate the temperature trispectra within the context of slow-roll inflation. In this scenario, non-Gaussianity emerges in the form of nonlinear corrections to the correspondence between a Gaussian inflaton fluctuation and the primordial potential Φ. Consequently, the higher-order terms can be expressed as follows

$$\Phi(\boldsymbol{x}) = \Phi_G(\boldsymbol{x}) + f_1\left(\Phi_G^2(\boldsymbol{x}) - \langle\Phi_G^2(\boldsymbol{x})\rangle\right) + f_2\,\Phi_G^3(\boldsymbol{x})\,, \tag{3.19}$$

where $\Phi_G(\boldsymbol{x})$ denotes the linear Gaussian component of the Bardeen curvature potential, and the non-Gaussian contributions are parametrized by f_1 and f_2. Furthermore, equation (3.19) can be equivalently expressed in Fourier space as a convolution which is given by

$$\Phi(\boldsymbol{k}) = \Phi_G(\boldsymbol{k}) + \Phi_A(\boldsymbol{k}) + \Phi_B(\boldsymbol{k})\,, \tag{3.20}$$

with the nonlinear contributions defined as follows

$$\Phi_A(\boldsymbol{k}) = f_1 \left[\int \frac{d^3\boldsymbol{p}}{(2\pi)^3} \, \Phi_G(\boldsymbol{k}+\boldsymbol{p}) \, \Phi_G(\boldsymbol{p}) - (2\pi)^2 \delta(\boldsymbol{k}) \langle \Phi_G^2(\boldsymbol{x}) \rangle \right] , \tag{3.21}$$

$$\Phi_B(\boldsymbol{k}) = f_2 \int \frac{d^3\boldsymbol{p}_1}{(2\pi)^3} \frac{d^3\boldsymbol{p}_2}{(2\pi)^3} \, \Phi_G(\boldsymbol{p}_1) \, \Phi_G(\boldsymbol{p}_2) \, \Phi_G(\boldsymbol{p}_1 + \boldsymbol{p}_2 + \boldsymbol{k}) \, . \tag{3.22}$$

Then, the connected part of the four-point correlation $\langle \Phi(\boldsymbol{k}_1)\Phi(\boldsymbol{k}_2)\Phi(\boldsymbol{k}_3)\Phi(\boldsymbol{k}_4)\rangle_c$ has leading order contribution from terms of the form $\langle \Phi_A(\boldsymbol{k}_1)\Phi_A(\boldsymbol{k}_2)\Phi_G(\boldsymbol{k}_3)\Phi_G(\boldsymbol{k}_4)\rangle_c$ and $\langle \Phi_B(\boldsymbol{k}_1)\Phi_G(\boldsymbol{k}_2)\Phi_G(\boldsymbol{k}_3)\Phi_G(\boldsymbol{k}_4)\rangle_c$. In particular, we focus on the term that involves cubic order contribution in Φ, which takes the following form

$$\langle \Phi_B(\boldsymbol{k}_1)\Phi_G(\boldsymbol{k}_2)\Phi_G(\boldsymbol{k}_3)\Phi_G(\boldsymbol{k}_4)\rangle_c \, .$$

In general, the primordial trispectrum can be defined as

$$\langle \Phi(\boldsymbol{k}_1)\Phi(\boldsymbol{k}_2)\Phi(\boldsymbol{k}_3)\Phi(\boldsymbol{k}_4)\rangle_c = (2\pi)^3 \, \delta(\boldsymbol{k}_1 + \boldsymbol{k}_2 + \boldsymbol{k}_3 + \boldsymbol{k}_4) T_\Phi(\boldsymbol{k}_1, \boldsymbol{k}_2, \boldsymbol{k}_3, \boldsymbol{k}_4) \, , \tag{3.23}$$

here, the four wavevectors form a quadrilateral as shown in figure 4.4. However, a more useful definition is to write

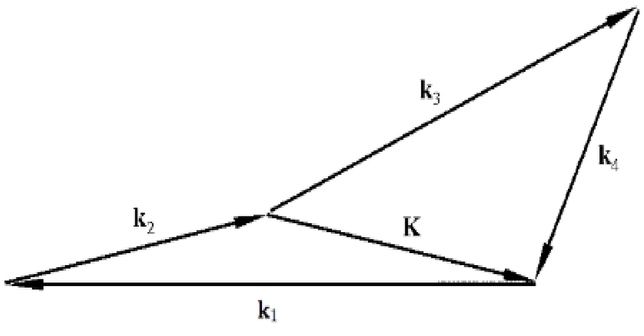

Figure 3.4: Quadrilateral configuration in terms of the wavevectors $\boldsymbol{k}_i$ and the diagonal $\boldsymbol{K}$. Taken from Regan et al. (2010).

$$\langle \Phi(\boldsymbol{k}_1)\Phi(\boldsymbol{k}_2)\Phi(\boldsymbol{k}_3)\Phi(\boldsymbol{k}_4)\rangle_c = (2\pi)^3 \int d^3\boldsymbol{K} \delta(\boldsymbol{k}_1 + \boldsymbol{k}_2 + \boldsymbol{K}) \delta(\boldsymbol{k}_3 + \boldsymbol{k}_4 - \boldsymbol{K}) \times T_\Phi(\boldsymbol{k}_1, \boldsymbol{k}_2, \boldsymbol{k}_3, \boldsymbol{k}_4, \boldsymbol{K}) \, , \tag{3.24}$$

in the above expression, the delta function indicates that the diagonal $\boldsymbol{K}$ makes triangles with $(\boldsymbol{k}_1, \boldsymbol{k}_2)$ and $(\boldsymbol{k}_3, \boldsymbol{k}_4)$, respectively. Since there are symmetries implicit in this definition of T_Φ, it is possible to form triangles with different combinations of the vectors. Then constructing

$$
\begin{aligned}
T_\Phi(\boldsymbol{k}_1, \boldsymbol{k}_2, \boldsymbol{k}_3, \boldsymbol{k}_4, \boldsymbol{K}) = P_\Phi(\boldsymbol{k}_1, \boldsymbol{k}_2, \boldsymbol{k}_3, \boldsymbol{k}_4, \boldsymbol{K}) + \int d^3\boldsymbol{K}' [\delta(\boldsymbol{k}_3 - \boldsymbol{k}_2 - \boldsymbol{K} + \boldsymbol{K}') \times \\
P_\Phi(\boldsymbol{k}_1, \boldsymbol{k}_3, \boldsymbol{k}_2, \boldsymbol{k}_4, \boldsymbol{K}') + \delta(\boldsymbol{k}_4 - \boldsymbol{k}_2 - \boldsymbol{K} + \boldsymbol{K}') P_\Phi(\boldsymbol{k}_1, \boldsymbol{k}_4, \boldsymbol{k}_3, \boldsymbol{k}_2, \boldsymbol{K}') \,,
\end{aligned}
\tag{3.25}
$$

where P_Φ are constructed using a reduced trispectrum $\mathcal{T}_\Phi$ according to

$$
\begin{aligned}
P_\Phi(\boldsymbol{k}_1, \boldsymbol{k}_2, \boldsymbol{k}_3, \boldsymbol{k}_4, \boldsymbol{K}) = \mathcal{T}_\Phi(\boldsymbol{k}_1, \boldsymbol{k}_2, \boldsymbol{k}_3, \boldsymbol{k}_4, \boldsymbol{K}) + \mathcal{T}_\Phi(\boldsymbol{k}_2, \boldsymbol{k}_1, \boldsymbol{k}_3, \boldsymbol{k}_4, \boldsymbol{K}) \\
+ \mathcal{T}_\Phi(\boldsymbol{k}_1, \boldsymbol{k}_2, \boldsymbol{k}_4, \boldsymbol{k}_3, \boldsymbol{K}) + \mathcal{T}_\Phi(\boldsymbol{k}_2, \boldsymbol{k}_1, \boldsymbol{k}_4, \boldsymbol{k}_3, \boldsymbol{K}) \,.
\end{aligned}
\tag{3.26}
$$

Therefore, considering only the reduced trispectrum for a particular arrangement of vectors is enough to form the other contribution by permuting the symbols. In particular, the leading order contribution to the reduced trispectrum $\mathcal{T}$ for the cubic contribution is given by

$$
\mathcal{T}_{\Phi_B}(\boldsymbol{k}_1, \boldsymbol{k}_2, \boldsymbol{k}_3, \boldsymbol{k}_4, \boldsymbol{K}) = f_2 \left[P_\Phi(k_2) P_\Phi(k_3) P_\Phi(k_4) + P_\Phi(k_1) P_\Phi(k_2) P_\Phi(k_4) \right] \,. \tag{3.27}
$$

On the other hand, we can express the harmonic four-point function using the relation between the multiple coefficients and the primordial potential, this leads to

$$
\begin{aligned}
\langle a_{l_1 m_1} a_{l_2 m_2} a_{l_3 m_3} a_{l_4 m_4} \rangle_c = (4\pi)^4 \, (-i)^{\sum_i l_i} \int \frac{d^3\boldsymbol{k}_1 ... d^3\boldsymbol{k}_4}{(2\pi)^{12}} \int d^3\boldsymbol{K} (2\pi)^3 \Delta_{l_1}(k_1) \Delta_{l_2}(k_2) \\
\times \Delta_{l_3}(k_3) \Delta_{l_4}(k_4) \delta(\boldsymbol{k}_1 + \boldsymbol{k}_2 + \boldsymbol{K}) \delta(\boldsymbol{k}_3 + \boldsymbol{k}_4 - \boldsymbol{K}) \\
\times T_\Phi(\boldsymbol{k}_1, \boldsymbol{k}_2, \boldsymbol{k}_3, \boldsymbol{k}_4, \boldsymbol{K}) Y^*_{l_1 m_1}(\hat{\boldsymbol{k}}_1) Y^*_{l_2 m_2}(\hat{\boldsymbol{k}}_2) Y^*_{l_3 m_3}(\hat{\boldsymbol{k}}_3) Y^*_{l_4 m_4}(\hat{\boldsymbol{k}}_4) \,,
\end{aligned}
\tag{3.28}
$$

applying the integral definition of the delta function and performing the Rayleigh expansion, we obtain that

$$
\begin{aligned}
\langle a_{l_1 m_1} a_{l_2 m_2} a_{l_3 m_3} a_{l_4 m_4} \rangle_c = \left(\frac{2}{\pi} \right)^5 \int r_1^2 dr_1 r_2^2 dr_2 (k_1 k_2 k_3 k_4 K)^2 dk_1 dk_2 dk_3 dk_4 dK j_L(K r_1) \\
\times j_L(K r_2) \left[\Delta_{l_1}(k_1) j_{l_1}(k_1 r_1) \right] \left[\Delta_{l_2}(k_2) j_{l_2}(k_2 r_1) \right] \left[\Delta_{l_3}(k_3) j_{l_3}(k_3 r_2) \right] \\
\times \left[\Delta_{l_4}(k_4) j_{l_4}(k_4 r_2) \right] \mathcal{T}_\Phi(k_1, k_2, k_3, k_4, K) h_{l_1 L l_2} h_{l_3 L l_4} \,,
\end{aligned}
\tag{3.29}
$$

where

$$
h_{l_1 L l_2} = \sqrt{\frac{(2l_1+1)(2l_2+1)(2L+1)}{4\pi}} \begin{pmatrix} l_1 & l_2 & L \\ 0 & 0 & 0 \end{pmatrix} \,, \tag{3.30}
$$

and j_l are the spherical Bessel functions. In order to derivate (3.29), we must choose an appropriate parametrization for $\mathcal{T}_\Phi$. Specifically, Regan et al. (2015) defined the quadrilateral configuration by the magnitudes of the four sides k_i, the diagonal length K and one angle θ which represents the deviation of the quadrilateral from planarity, in the case of local models is possible to consider $\theta = 0$, as a result, $\mathcal{T}_\Phi(k_1, k_2, k_3, k_4, K)$. Now, we substitute the expression (3.27) into the above equation. Subsequently, the CMB trispectrum linked to the cubic contribution can be expressed as

$$T_{l_1 m_1 l_2 m_2 l_3 m_3 l_4 m_4} = f_2 \, h_{l_1 L l_2} h_{l_3 L l_4} \int r^2 dr \beta_{l_2}(r) \beta_{l_4}(r) \left[\mu_{l_1}(r) \beta_{l_3}(r) + \beta_{l_1}(r) \mu_{l_3}(r) \right] , \tag{3.31}$$

with

$$\beta_l(r) = \frac{2}{\pi} \int k^2 dk P_\Phi(k) \Delta_l(k) j_l(kr) \, , \tag{3.32}$$

$$\mu_l(r) = \frac{2}{\pi} \int k^2 dk \Delta_l(k) j_l(kr) \, . \tag{3.33}$$

In order to evaluate the trispectrum, we need to numerically compute the radiation transfer function $\Delta_l(k)$ by solving the Einstein-Boltzmann equation. However, if our focus shifts to larger scales (where the multiple values are small, i.e. $l \ll 100$), we can assume that the dominant influence on temperature fluctuations is from gravitational potential fluctuations. Thus, we work under the assumption that the Sach-Wolfe effect stands as the only significant mechanism. As previously mentioned, the radiation transfer function takes on a simplified form $\Delta_l(k) \sim j_l(kr_*)/3$, where r_* denotes the conformal time elapsed from recombination to the present time. Moreover, equation (3.33) can be further simplified by exploiting the properties of the Bessel function

$$\int k^2 \, dk \, j_l(kr_*) \, j_l(kr) = \frac{\pi}{2r_*^2} \delta(r - r_*) \, , \tag{3.34}$$

$$\mu_l(r) = \frac{1}{3r_*^2} \delta(r - r_*) \, . \tag{3.35}$$

In this case, the temperature power spectrum in the SW approximation is given by

$$C_l^{SW} = \frac{2}{9\pi} \int dk \, k^2 \, P_\Phi(k) \, j_l^2(kr_*) \, , \tag{3.36}$$

and the other function becomes $\beta_l(k) = 3C_l^{SW}$. Therefore, the trispectrum can be expressed in terms of the temperature power spectrum as

$$T_{l_1l_2l_3l_4} = 9\,f_2\,C_{l_2}^{SW}\,C_{l_4}^{SW}\left(C_{l_1}^{SW} + C_{l_3}^{SW}\right) h_{l_1Ll_2}\,h_{l_3Ll_4}\,. \tag{3.37}$$

This formula serves as a concrete example of one trispectrum template of the CMB within the context of the local non-Gaussian model. This representation takes into account only the cubic-order contribution in the expansion of the primordial perturbations. The specific trispectrum structure involves products of the temperature angular power spectra, which we detailed in the previous section, the coefficient f_2 quantifying non-Gaussianity amplitude, and the coupling coefficients $h_{l_1Ll_2}$. The conventional approach to examining such expression requires the development of estimators that facilitate the numerical treatment of the obtained trispectrum.

Chapter 4

CMB Anomalies

Several unexpected features have been detected in the CMB radiation on larger angular scales, both by WMAP and Planck observations. Individually, these features manifest at significant levels, typically around 2-3σ, when tested against the ΛCDM model. Among those features are the hemispherical asymmetry, the presence of non-Gaussian cold/hot spots, the lack of large angular scales power, alignment of the quadrupole and octopole, and parity asymmetry. The emergence of these anomalies in the data has opened discussions regarding their origin and their potential implications for our current cosmological model.

Despite numerous detailed investigations, a comprehensive understanding of the anomalies remains elusive. Their presence in the data appears to challenge the statistical isotropy and scale invariance, as expected from the inflationary perturbations Schwarz et al. (2015). Therefore, it becomes intriguing to explore alternative models capable of reproducing the CMB anomalies and fitting better the observational data than the standard isotropic and Gaussian assumptions.

4.1 Large-scale hemispherical asymmetry

Evidence of this anomaly emerged when local estimates of the angular power spectrum on large scales within the WMAP data disclosed a power asymmetry between two hemispheres in the sky (Hansen et al., 2004; Eriksen et al. 2007). This hemispherical power asymmetry has subsequently been modeled as a dipolar modulation of an isotropic sky,

$$T(\hat{\boldsymbol{n}}) = T_0(\hat{\boldsymbol{n}}) \left[1 + A\, \hat{\boldsymbol{n}} \cdot \hat{\boldsymbol{d}}\right] , \tag{4.1}$$

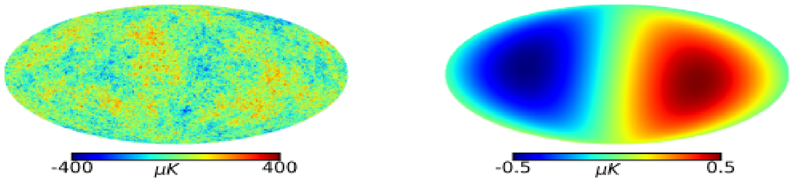

(a) Original map (b) Modulation field

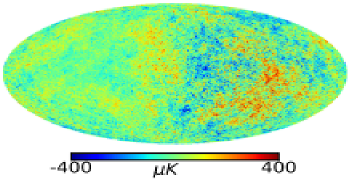

(c) Dipole modulated map

Figure 4.1: Example of a dipole modulation map leading to a pronounced large-scale hemispherical power asymmetry. Taken from Bjørklund (2021).

where $T(\hat{\boldsymbol{n}})$ and $T_0(\hat{\boldsymbol{n}})$ represent the modulated and unmodulated temperature fields, respectively, with $\hat{\boldsymbol{n}}$ denoting an arbitrary direction on the sky. The parameters A and $\hat{\boldsymbol{d}}$ correspond to the amplitude and preferred direction of the dipolar modulation. The result of the Planck 2015 analyses, employing the Commander map, yielded an estimate of $A = 0.066 \pm 0.021$, with the preferred direction $\hat{\boldsymbol{d}}$ aligning towards $(l, b) = (230^\circ, -16^\circ) \pm 24^\circ$ Ade et al. (2016). In figure 5.2, we provide a visual representation of the effect of a dipolar modulation. It can be noticed, that the fluctuations in one hemisphere are enhanced, while in the opposite hemisphere, they are suppressed. More refined analyses from the latest Planck release report an amplitude of $A = 0.0695$ and a dipole direction of $(l, b) = (221^\circ, -20^\circ)$, incorporating the combination of temperature, polarization, and cross-correlations (TT, EE, TE) from the component maps Commander, NILC, SEVEM, and SMICA Akrami et al. (2020b).

4.2 Small-scale hemispherical asymmetry

Similar to the hemispherical asymmetry observed on large scales, Hansen et al. (2009) identified the extension of this asymmetry to smaller scales (higher multipoles l). This observation was subsequently supported by studies conducted by Axelsson et al. (2013) and Ade et al. (2016), who confirmed the presence of this anomaly within both the WMAP and Planck datasets. It is noteworthy that this asymmetry does not arise from a dipolar modulation, as seen in the previous case. Since the observed amplitude of the dipolar modulation falls well within the expected range of Gaussian simulations. In the context of an isotropic and Gaussian sky, a random dipole component is always present.

4.3 The Cold Spot

Another anomaly identified in the WMAP first-year data is the existence of a large cold spot in the southern hemisphere of the CMB map, as illustrated in figure 4.2.

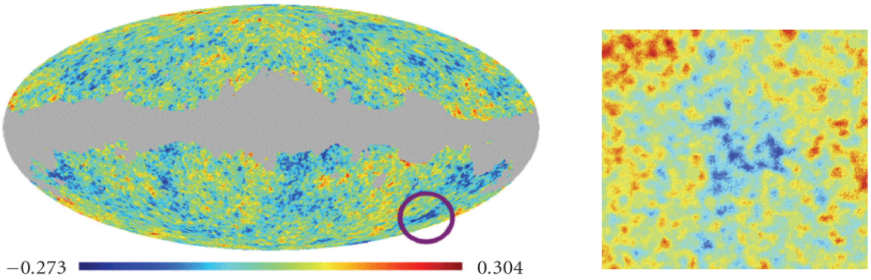

Figure 4.2: Cold spot in WMAP 7th year temperature maps. The left panel shows the complete map with a circle surrounding the anomaly. While the right panel is a more detailed view of the spot. The figures are adopted from Schwarz et al. (2015).

The cold spot's coordinates are situated at $(l, b) = (207°, -57°)$ Cruz et al. (2006) and it consists of several smaller spots, each with an approximate temperature of -350 μK and a size of about 1°. The spot's morphology is found to be isotropic and nearly circular, with an additional intriguing feature of being surrounded by a hot ring. Various hypotheses have been proposed to account for its presence in the data. These include exploring potential under-densities in the galaxy distribution and investigating possible links with cold spots in the CMB maps, or looking for some diffuse foregrounds that have not been considered up to now.

4.4 Large-scale power deficit

One of the extensively studied anomalies is the deficit of power in the power spectrum on large scales. Both the WMAP and Planck power spectra of the CMB temperature anisotropy, particularly at large scales ($l < 30$), exhibit values that are lower than what aligns with the predictions of the best-fit cosmological model. As depicted in figure 3.2, the Planck power spectrum is shown alongside the best-fit model. Notably, the quadrupole $l = 2$ exhibits a low value and a dip in the spectrum is around $l \simeq 21$. However, it is also important to consider the possibility that this diminished large-scale spectrum might arise as a statistical fluke, given the impact of cosmic variance at this scale. Nonetheless, the significance of this anomaly persists at the 2-3σ level Hansen et al. (2019).

4.5 Quadrupole and octopole alignment

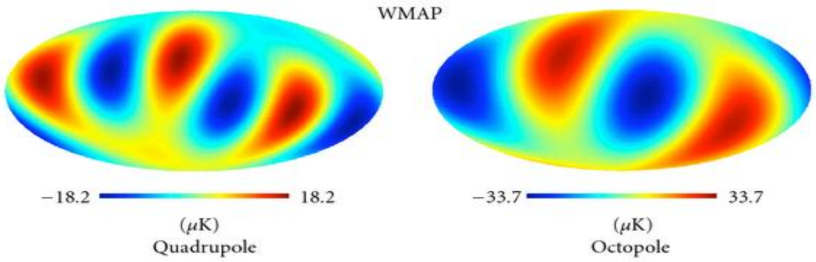

Figure 4.3: Quadrupole and octopole alignment detected by WMAP mission. Image credit Kavli Institute for Cosmological Physics, University of Chicago.

The current cosmological model assumes that temperature anisotropies possess random phases, which translates into uncorrelated orientations and shapes of multipole moments in harmonic space. However, an apparent alignment between the quadrupole ($l = 2$) and octopole ($l = 3$) was found in WMAP data by Tegmark et al. (2003). This alignment suggests that the patterns observed in the quadrupole and octopole moments exhibit a degree of correlation (not randomly distributed), contrary to what would be expected from the standard cosmological model.

The proposed explanations for this anomaly are often related to the Universe's topology. Considerations of a non-trivial topology on large scales could lead to specific correlations in the CMB temperature fluctuations. For instance, the plain bagel small universe model de Oliveira-Costa et al. (2004) and twisted back-to-back models Cornish et al. (2004). Nevertheless, it is also plausible that the observed alignment could arise from a statistical fluke, as random fluctuations can occasionally lead to unexpected patterns.

4.6 Parity asymmetry

This anomaly refers to the observation that the CMB does not exhibit symmetry under parity transformations. It is important to note that the standard cosmology model does not offer any specific predictions in this regard. Both the WMAP and Planck data reveal a significant odd-multipoles preference in the large scales of the CMB (e.g. Cheng et al. 2016), indicating a preferred axis in the CMB parity asymmetry. Specifically, the C_l values for the lowest even multipoles consistently appear lower than those for odd multipoles (Ade et al., 2016).

The precise origins of the parity asymmetry in the CMB temperature maps are still under investigation. Recent studies have shown the presence of this anomaly both on local and global scales. Additionally, the motion of the solar system might contribute to the asymmetry. Furthermore, certain inflationary models propose the presence of the parity violation, suggesting that the anomaly could be a consequence of the interaction between the inflaton field and other fields during the early universe.

4.7 Possible explanations

Even though extensive studies have been conducted in order to explain some of the CMB anomalies, we still do not have a consensus about their origins. Thus, many argue that they are the result of statistical fluctuations, having a low significance. Others, however, have explored the idea that they may share a common cosmological origin, with the efforts centered on finding an explanation within the context of the inflationary paradigm.

The attempts to model the observed statistical anisotropies in the CMB can be categorized into two groups: (i) explicit breaking of statistical isotropy, which implies a preferred direction in the Universe, or (ii) the statistical isotropy breaking is spontaneous due to some stochastic modulating field or primordial non-Gaussianity. In this brief review, we will particularly focus on some of the various ideas proposed to study the hemispherical power asymmetry.

Numerous studies have examined the observed power asymmetry and assessed its statistical significance using the WMAP and the Planck data. Several potential explanations for this asymmetry have already been discussed, as explored in detail in Dai et al. 2013). One particularly intriguing approach involves using superhorizon fluctuations to generate the asymmetry, achieved either by employing non-Gaussianity to couple them to observable perturbations or by postulating different primordial physics preceding the usual slow-roll inflation. Alternatively, one can also postulate scenarios that are fundamentally anisotropic on the largest scales.

In their study, Adhikari et al. (2016) systematically analyzed the statistical properties of the power asymmetry expected in the CMB under the assumption of non-Gaussian primordial perturbations existing on scales larger than we can observe. They investigated both local and non-local models of primordial non-Gaussianity, providing a general method for describing deviations from statistical isotropy in a finite sub-volume of an isotropic (but non-Gaussian) large volume. The study also explored various explanations for the hemispherical power asymmetry. Furthermore, the authors found that non-local models of non-Gaussianity and scale-dependent local non-Gaussianity have the potential to account for the observed scale dependence of the power asymmetry on large scales.

Moreover, it has been considered that if the primordial bispectrum (the Fourier counterpart of the three-point function) is sufficiently large, the CMB hemispherical power asymmetry may be explained by a large-scale mode of strong amplitude that perturbs the 2-point function. In response to this, Byrnes et al. (2016a) provided a method to compute the response of the two-point function in any model yielding a local-like bispectrum. In general, this analysis shows that it is not the reduced bispectrum $f_{NL}(k_1, k_2, k_3)$ that sources the amplitude and scale dependence of the mode coupling, but rather a combination of 'response functions'. Therefore, contrary to previous analyses, they concluded that it is possible to generate the asymmetry while respecting observational constraints on the bispectrum and low-l multipoles, even without tuning our location on the long-wavelength mode.

Other investigations have focused on studying several cosmological scenarios in which anomalies like hemispherical power asymmetry can arise. When considering only the power asymmetry, Erickcek et al. (2008) found that it cannot be produced during single-field slow-roll inflation without violating the assumption of homogeneity of the Universe. However, within the framework of multi-field inflationary theory, such as the curvaton model, this anomaly can emerge while preserving the condition of homogeneity. The physical mechanism requires the consideration of a large-amplitude super-horizon perturbation, as depicted in figure 4.4, possibly a pre-inflationary remnant. It is considered that this perturbation could introduce a preferred direction in the Universe, thus generating the observed asymmetry.

To support previous studies, Byrnes et al. (2016b) made also the assumption that explanations for this hemispherical asymmetry require non-Gaussian fluctuations that couple observable modes to those on much larger scales, and they conducted thorough analyses of these scenarios. The study of single-source scenarios presented numerous difficulties, so they chose not to further pursue these models. In contrast, multiple-source scenarios appear to be more flexible and offer a better description of the anomaly. However, it remains unclear whether the proposed inflationary model can be embedded within a viable early Universe scenario.

A more recent study of the anomaly by Adhikari et al. (2018) revealed that the

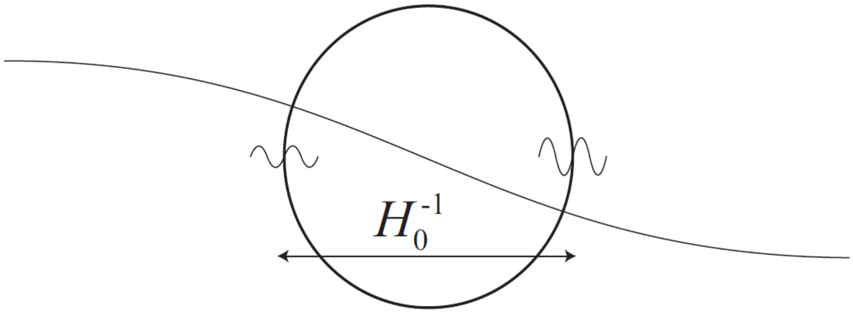

Figure 4.4: Representation of the modulation of short-wavelength (sub-horizon) perturbation modes due to the presence of a long-wavelength (super-horizon) one, ensured by the coupling provided by local non-Gaussianity. Taken from Erickcek et al. (2008).

hemispherical power asymmetry and the lack of power at large scales may arise in models featuring local-trispectra with strong scale-dependent τ_{NL} amplitude. In particular, this type of τ_{NL} trispectrum can originate from the modulation of the primordial curvature perturbation by a second uncorrelated field, as proposed by Byrnes et al. (2016b). It is worth mentioning that this specific work does not reproduce all the observed CMB anomalies.

However, the majority of the models proposed to study the CMB anomalies somehow fail to achieve the correct description of some features of the large-scale power asymmetry, or even to address several anomalies. These results provide evidence of the challenge of constructing a model that can accurately reproduce all anomalies while satisfying current constraints.

Another attempt to understand the CMB anomalies was made by Hansen et al. (2019), where they considered that these anomalous features share a common cosmological origin and proposed a toy model that can naturally reproduce six of the previously mentioned anomalies. Their methodology is based on the idea that the non-linear terms that appear in the primordial gravitational potential, in some inflationary models, introduce non-Gaussianity. It is the presence of non-Gaussianity that originates the apparent deviations from statistical isotropy and features in the power spectrum seen in the data. While this work does not explicitly construct an inflationary model, it focuses on determining the phenomenological properties a physical model should exhibit. In this thesis, our focus is on finding the properties of a possible inflationary model that can satisfy the conditions proposed for the toy model.

As we have seen, there are still many open questions about the CMB anomalies and various methodologies can be implemented for their comprehensive study. This chapter has highlighted some standard approaches to studying the hemispherical asymmetry, despite encountering some difficulties. In particular, the toy model that we plan to study in the next chapter incorporates some of the ideas proposed in previous work to construct a new model capable of effectively reproducing the anomalies discussed in this chapter. We hope this work can provide some insight into the physical model behind the phenomenological model constructed by Hansen et al. (2019).

To conclude this section, it is necessary to mention a relatively recent study that aims to explain the presence of CMB anomalies as a result of an unknown foreground in the CMB maps. Luparello et al. (2022) identified the presence of a new foreground in the CMB associated with extended galactic halos. They found that this foreground is statistically significant and proposed that it should be considered in detailed cosmological studies. Taking this effect into account, Hansen et al. (2023) investigated whether the new foreground might impact the CMB fluctuations map and produce the observed CMB anomalies. Their findings suggested a remarkable resemblance between the temperature model map based on nearby galaxies and the Planck CMB map. Therefore, it is highly probable that the largest scales of the CMB and the cosmological parameters may have important changes after proper corrections of this new foreground component. However, reliable CMB corrected maps can only be derived when suitable physical mechanisms are proposed and tested.

Chapter 5

Phenomenological Model

Chapter 4 revealed that the analysis of observational data from the CMB has brought to light the existence of certain statistical deviations from the standard cosmological model, collectively known as CMB anomalies. The origin of these features remains a topic of investigation and constitutes a central motivation for this thesis.

A recent investigation by Hansen et al. (2019) introduces a phenomenological model that can reproduce six of the most extensively studied CMB anomalies. The basis of this model lies in the assumption of initial perturbations exhibiting non-Gaussianity, which subsequently impacts the statistical properties of CMB radiation. Notably, the toy model's significance lies in its capability to account for multiple anomalies.

This chapter aims to present the relevant details of the toy model and demonstrate how it is possible to establish a connection between this proposed model and a plausible physical model. Specifically, this connection is explored within the framework of the inflationary paradigm.

5.1 Proposed model

The temperature field considered in the model developed by Hansen et al. (2019) follows a construction rooted in the conventional approach of modeling the power asymmetry through a dipolar modulation. However, to effectively replicate the six aforementioned anomalies, the model requires the incorporation of a set of filters. These filters serve to facilitate the emergence of additional anomalous features while preventing them from becoming more pronounced than expected. Additionally, the filters must ensure the production of temperature maps consistent with the observed

CMB maps. Thus, the structure of the toy model can be described as follows

$$T(\theta,\phi) = T_G(\theta,\phi) + \beta\left[T_G(\theta,\phi)T_F^2(\theta,\phi)\right]^{Filtered}, \tag{5.1}$$

where T_G represents an isotropic Gaussian CMB temperature realization, and T_F denotes the filter temperature field given by

$$T_F(\hat{\boldsymbol{n}}) = \sum_{lm} a_{lm}^F\, Y_{lm}(\hat{\boldsymbol{n}})\,, \tag{5.2}$$

with $\hat{\boldsymbol{n}} = (\theta,\phi)$. Furthermore, the filtered multiple coefficient a_{lm}^F is defined as follows

$$a_{lm}^F = \int d\Omega(\hat{\boldsymbol{n}})\, Y_{lm}^*(\hat{\boldsymbol{n}})\, T(\hat{\boldsymbol{n}})\, w_l = w_l\, a_{lm}^G\,, \tag{5.3}$$

with the low-pass filter w_l approaching zero for $l > 28$. Notably, equation (5.1) results in a non-Gaussian temperature field that possesses the structural attributes for replicating several of the CMB anomalies. To uncover the physical model that underlies this toy model, our task involves identifying a theory in which the introduction of non-Gaussianity is viable, analogous to how it was accomplished with the temperature field. This entails addressing cubic-order contributions within our theory. However, before working on this, it would be advantageous to expand the temperature field using its representation in spherical harmonics.

Let's consider equation (5.1) and express each term using the spherical harmonic formalism. As a result, we obtain

$$\sum_{lm} a_{lm}^{NG}\, Y_{lm}(\hat{\boldsymbol{n}}) = \sum_{lm} a_{lm}^G\, Y_{lm}(\hat{\boldsymbol{n}}) + \beta \sum_{lm} a_{lm}^F\, Y_{lm}(\hat{\boldsymbol{n}})\,. \tag{5.4}$$

In this case, our focus is only on the relationship between the multiple coefficients. Thus, we define that

$$a_{lm}^{NG} = a_{lm}^G + \beta\, a_{lm}^F\,, \tag{5.5}$$

where the filtered multiple coefficient a_{lm}^F can be defined as follows

$$\begin{aligned} a_{lm}^F &= \int d\Omega(\hat{\boldsymbol{n}}) Y_{lm}^*(\hat{\boldsymbol{n}})\, T_G(\hat{\boldsymbol{n}})\, T_F^2(\hat{\boldsymbol{n}}) \\ &= \sum_{\substack{l_i m_i \\ i=1,2}} \int d\Omega(\hat{\boldsymbol{n}}) Y_{lm}^*(\hat{\boldsymbol{n}}) a_{l_1m_1}^G Y_{l_1m_1}(\hat{\boldsymbol{n}})\, a_{l_2m_2}^{2F} Y_{l_2m_2}(\hat{\boldsymbol{n}})\,, \end{aligned} \tag{5.6}$$

$$a^F_{lm} = \sum_{\substack{l_i m_i \\ i=1,2,3,4}} \int d\Omega(\hat{\boldsymbol{n}}) Y^*_{lm}(\hat{\boldsymbol{n}}) a^G_{l_1 m_1} Y_{l_1 m_1}(\hat{\boldsymbol{n}}) Y_{l_2 m_2}(\hat{\boldsymbol{n}})$$

$$\times \int d\Omega(\hat{\boldsymbol{n}}') Y^*_{l_2 m_2}(\hat{\boldsymbol{n}}') a^F_{l_1 m_1} Y_{l_1 m_1}(\hat{\boldsymbol{n}}') a^F_{l_3 m_3} Y_{l_4 m_4}(\hat{\boldsymbol{n}}') \,, \tag{5.7}$$

in the above expression, we have defined that

$$a^{2F}_{lm} = \sum_{\substack{l_i m_i \\ i=1,2}} \int d\Omega(\hat{\boldsymbol{n}})\, Y^*_{lm}(\hat{\boldsymbol{n}})\, a^F_{l_1 m_1} Y_{l_1 m_1}(\hat{\boldsymbol{n}})\, a^F_{l_2 m_2} Y_{l_2 m_2}(\hat{\boldsymbol{n}}) \,. \tag{5.8}$$

By using the orthogonal properties of the spherical harmonic functions, we can further simplify equation (5.7)

$$\sum_{lm} Y^*_{lm}(\hat{\boldsymbol{n}}') Y_{lm}(\hat{\boldsymbol{n}}) = \delta^3(\hat{\boldsymbol{n}}' - \hat{\boldsymbol{n}}) \,, \tag{5.9}$$

we obtain the following expression

$$a^F_{lm} = \sum_{\substack{l_i m_i \\ i=1,2,3}} a^G_{l_1 m_1} a^F_{l_2 m_2} a^F_{l_3 m_3} \int d\Omega(\hat{\boldsymbol{n}}) Y^*_{lm}(\hat{\boldsymbol{n}}) Y_{l_1 m_1}(\hat{\boldsymbol{n}}) Y_{l_2 m_2}(\hat{\boldsymbol{n}}) Y_{l_3 m_3}(\hat{\boldsymbol{n}}) \,. \tag{5.10}$$

Notice that we can use the definition provided by equation (5.3) to express the filtered multiple coefficients. Consequently, we express the filtered contribution of the temperature field as follows

$$a^F_{lm} = \sum_{\substack{l_i m_i \\ i=1,2,3}} a^G_{l_1 m_1}\, a^G_{l_2 m_2}\, a^G_{l_3 m_3}\, w_{l_2} w_{l_3}\, \mathcal{B}^{l_1 m_1 l_2 m_2 l_3 m_3}_{lm} \,, \tag{5.11}$$

where,

$$\mathcal{B}^{l_1 m_1 l_2 m_2 l_3 m_3}_{lm} = \int d\Omega(\hat{\boldsymbol{n}}) Y^*_{lm}(\hat{\boldsymbol{n}}) Y_{l_1 m_1}(\hat{\boldsymbol{n}}) Y_{l_2 m_2}(\hat{\boldsymbol{n}}) Y_{l_3 m_3}(\hat{\boldsymbol{n}}) \,. \tag{5.12}$$

However, in order to optimally replicate the anomalies, it is essential for the final term itself to be filtered. This requires incorporating an additional filter g_l. Consequently, the final expression for the non-Gaussian contribution of the cubic temperature field in harmonic representation can be formulated as follows

$$a^{NG}_{lm} = \beta a^F_{lm} = \beta \sum_{\substack{l_i m_i \\ i=1,2,3}} a^G_{l_1 m_1}\, a^G_{l_2 m_2}\, a^G_{l_3 m_3}\, g_l\, w_{l_2}\, w_{l_3}\, \mathcal{B}^{l_1 m_1 l_2 m_2 l_3 m_3}_{lm} \,. \tag{5.13}$$

The amplitude β and filters w_l and g_l serve as adjustable parameters that can be

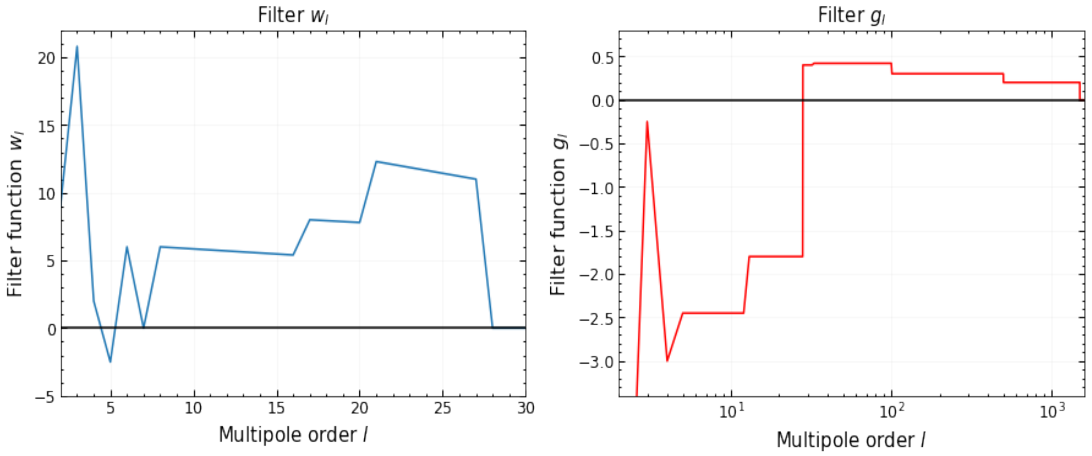

Figure 5.1: The filters w_l and g_l are plotted within the ranges $l = (2, 30)$ and $l = (2, 1500)$, respectively.

tuned to reproduce the anomalous features. Particularly, the parameter β quantifies the strength of the non-Gaussian contribution. Regarding the filters, one of the proposed shapes can be seen in figure 5.1. From the structure of the filters, we can infer that w_l acts as a filter for large scale (low l), while g_l operates on small scales (high l). Different filter shapes are illustrated in Figure 2 of Hansen et al. (2019).

5.2 g_{NL} model with strong scale-dependence

The form of non-Gaussianity incorporated in the toy model is based on the concept of the local model, as previously discussed in earlier chapters. This specific type of non-Gaussian model is employed to describe deviations from a purely Gaussian distribution of primordial fluctuations that are generated during inflation. It is commonly assumed that the primordial gravitational potential Φ (represented as Bardeen's gauge-invariant variable Φ_H) can be expressed as a local but nonlinear transformation of a linear random field Φ_G (Liguori et al. 2003). The term local refers to the fact that the model introduces a scale-dependent correction that varies according to the observed region in the sky. As a result, the level of non-Gaussianity can change depending on the angular scale of the CMB radiation. This leads to the following parametrization

$$\Phi(\boldsymbol{x}) = \Phi_G(\boldsymbol{x}) + f_{NL}\left[\Phi_G^2(\boldsymbol{x}) - \langle\Phi_G^2(\boldsymbol{x})\rangle\right] + g_{NL}\left[\Phi_G^3(\boldsymbol{x}) - \langle\Phi_G^3(\boldsymbol{x})\rangle\right] , \tag{5.14}$$

in real space, $\Phi_G(\boldsymbol{x})$ represents the linear Gaussian component of the primordial gravitational potential. The parameters f_{NL} and g_{NL} serve to quantify the amplitude of non-gaussianity within the model.

However, it proves convenient to consider a g_{NL}-type model with strong scale dependence. Given that the non-Gaussian contribution in the toy model operates at cubic order, our focus will be on models with a strong scale dependence, specifically involving the parameter g_{NL}.

Local effects within inflationary models can emerge when there are interactions or correlations across different scales of perturbations. In a standard single-field slow-roll inflation context, interactions between different Fourier modes are typically negligible, leading to a local Gaussian distribution of perturbations. Nevertheless, in scenarios where local interactions are significant, the statistical properties of the perturbations can deviate from Gaussianity, such that the non-linearity parameters are no longer constants, but dependent on a k mode in Fourier space.

One specific model that can give rise to local-type non-Gaussianity effects is the *Curvaton Model.* In this model, a secondary scalar field known as the curvaton contributes to the primordial fluctuations alongside the inflaton field. Interactions between the inflaton and the curvaton field can induce local effects in the perturbations, generating non-Gaussian features in the CMB temperature anisotropies. In our case, conducting more in-depth analyses of the relationship between the temperature field of the toy model and the inflationary quantity ζ becomes indispensable to clarify which inflationary model could produce the necessary conditions for generating the observed CMB anomalies.

Generally, as outlined by Schmidt and Kamionkowski (2010), the non-local function of the Gaussian field can be expressed as a convolution kernel. In other words, the constant parameter g_{NL} is substituted with a suitable convolution kernel. Consequently, the resulting expression in terms of the curvature perturbation ζ, which is related to Φ, takes the following form in real space

$$\begin{aligned}\zeta(\boldsymbol{x}) = \zeta_G(\boldsymbol{x}) + g_{NL} \int d^3\boldsymbol{x_1}\, d^3\boldsymbol{x_2}\, d^3\boldsymbol{x_3}\, \mathcal{W}(\boldsymbol{x_1}, \boldsymbol{x_2}, \boldsymbol{x_3})\, \zeta_G(\boldsymbol{x}+\boldsymbol{x_1}) \\ \times \zeta_G(\boldsymbol{x}+\boldsymbol{x_2})\, \zeta_G(\boldsymbol{x}+\boldsymbol{x_3})\,,\end{aligned} \tag{5.15}$$

where $\mathcal{W}$ represents the kernel function. The parameter g_{NL} quantifies the non-Gaussian amplitude. In Fourier space, after applying the properties of the Fourier transform and Dirac delta (see, Appendix A), the above expression can be written as follows

$$\zeta(\boldsymbol{k}) = \zeta_G(\boldsymbol{k}) + g_{NL} \prod_{i=1}^{2} \int \frac{d^3\boldsymbol{k}_i}{(2\pi)^3} \tilde{\mathcal{W}}(\boldsymbol{k}_1, \boldsymbol{k}_2, \tilde{\boldsymbol{k}}_{12}) \zeta_G(\boldsymbol{k}_1) \zeta_G(\boldsymbol{k}_2) \zeta_G(\tilde{\boldsymbol{k}}_{12})\,, \tag{5.16}$$

here, it is defined that $\tilde{\boldsymbol{k}}_{12} = \boldsymbol{k} - \boldsymbol{k}_1 - \boldsymbol{k}_2$. Therefore, the kernel is

$$\tilde{\mathcal{W}}(\boldsymbol{k}_1, \boldsymbol{k}_2, \tilde{\boldsymbol{k}}_{12}) = \prod_{i=1}^{3} \int d^3\boldsymbol{x}_i \mathcal{W}(\boldsymbol{x}_1, \boldsymbol{x}_2, \boldsymbol{x}_3)\, e^{i\boldsymbol{k}_1\cdot\boldsymbol{x}_1} e^{i\boldsymbol{k}_2\cdot\boldsymbol{x}_2} e^{i\tilde{\boldsymbol{k}}_{12}\cdot\boldsymbol{x}_3} \,. \tag{5.17}$$

By examining equation (5.16), we can derive an expression for the scale-dependent parameter g_{NL} as follows

$$g_{NL}(\boldsymbol{k}_1, \boldsymbol{k}_2, \tilde{\boldsymbol{k}}_{12}) = g_{NL}\, \tilde{\mathcal{W}}(\boldsymbol{k}_1, \boldsymbol{k}_2, \tilde{\boldsymbol{k}}_{12}) \,. \tag{5.18}$$

Furthermore, we can determine that the general form of the non-Gaussian curvature perturbation ζ in this model is

$$\zeta(\boldsymbol{k}) = \zeta_G(\boldsymbol{k}) + g_{NL}\, \zeta_{NG}(\boldsymbol{k}) \,. \tag{5.19}$$

The next step is to establish a connection between the curvature perturbation ζ given by equation (5.16) and the multipole coefficients a_{lm}, which contain the statistical information of the temperature field in harmonic space.

5.3 Relation between ζ and a_{lm} coefficient

It is always possible to introduce a transfer function $\Delta_l(k)$ to relate the curvature perturbation ζ and the temperature field. The expression is given by

$$a_{lm} = -\frac{12\pi}{5}\, i^l \int \frac{d^3\boldsymbol{k}}{(2\pi)^3}\, \Delta_l(k)\, Y^*_{lm}(\hat{\boldsymbol{k}})\, \zeta(\boldsymbol{k}) \,, \tag{5.20}$$

here, we have used equations (3.10) and (3.11). By substituting the definition of ζ from the g_{NL}-like scale dependent model as provided in (5.16), we can deduce that

$$a^G_{lm} = -\frac{12\pi}{5} i^l \int \frac{d^3\boldsymbol{k}}{(2\pi)^3} \Delta_l(k) Y^*_{lm}(\hat{\boldsymbol{k}})\, \zeta_G(\boldsymbol{k}) \,, \tag{5.21}$$

$$a^{NG}_{lm} = -g_{NL}\frac{12\pi}{5} i^l \int \frac{d^3\boldsymbol{k}}{(2\pi)^3} \Delta_l(k) Y^*_{lm}(\hat{\boldsymbol{k}}) \prod_{i=1}^{2} \int \frac{d^3\boldsymbol{k}_i}{(2\pi)^3} \tilde{\mathcal{W}}(\boldsymbol{k}_1, \boldsymbol{k}_2, \tilde{\boldsymbol{k}}_{12}) \times \zeta_G(\boldsymbol{k}_1)\zeta_G(\boldsymbol{k}_2)\zeta_G(\tilde{\boldsymbol{k}}_{12}) \,. \tag{5.22}$$

The first term corresponds to the Gaussian contribution, a^G_{lm}, while the second term denotes the non-Gaussian cubic-order contribution, a^{NG}_{lm}. From our previous results, we can establish a one-to-one correspondence between our multiple coefficients expressed in terms of ζ, as given in equations (5.21) and (5.22), and the coefficients obtained through the expansion of the temperature field as shown in equation (5.13). Consequently, we have $a_{lm}^{NG} = \beta a_{lm}^{F}$

$$\begin{aligned}
a_{lm}^{NG} &= -g_{NL}\frac{12\pi i^l}{5}\int\frac{d^3\boldsymbol{k}}{(2\pi)^3}\Delta_l(k)Y_{lm}^*(\hat{\boldsymbol{k}})\prod_{i=1}^{2}\int\frac{d^3\boldsymbol{k}_i}{(2\pi)^3}\tilde{\mathcal{W}}(\boldsymbol{k}_1,\boldsymbol{k}_2,\tilde{\boldsymbol{k}}_{12})\zeta_G(\boldsymbol{k}_1)\zeta_G(\boldsymbol{k}_2)\zeta_G(\tilde{\boldsymbol{k}}_{12})\\
&= \beta\sum_{\substack{l_i m_i\\ i=1,2,3}} a_{l_1m_1}^{G}\,a_{l_2m_2}^{G}\,a_{l_3m_3}^{G}\,g_l\,w_{l_2}\,w_{l_3}\,\mathcal{B}_{lm}^{l_1m_1l_2m_2l_3m_3}\\
&= \beta\sum_{\substack{l_i m_i\\ i=1,2,3}} a_{l_1m_1}^{G}\,a_{l_2m_2}^{G}\,a_{l_3m_3}^{G}\,\tilde{W}_{l_1m_1l_2m_2l_3m_3}^{lml_2l_3} = \beta a_{lm}^{F}\,.
\end{aligned} \tag{5.23}$$

For simplicity, we have defined that,

$$\tilde{W}_{l_1m_1l_2m_2l_3m_3}^{lml_2l_3} = g_l\,W_{l_1m_1l_2m_2l_3m_3}^{lml_2l_3} = g_l\,w_{l_2}\,w_{l_3}\,\mathcal{B}_{lm}^{l_1m_1l_2m_2l_3m_3}\,. \tag{5.24}$$

We have now established a comprehensive correlation between the two distinct definitions of the multipole coefficients, a_{lm}. Our current focus is to understand the relationship between the kernel proposed in the definition of the non-Gaussian curvature perturbation ζ and the filters used to generate the non-Gaussian temperature field, in other words, the relation between $\tilde{\mathcal{W}}(\boldsymbol{k}_1,\boldsymbol{k}_2,\tilde{\boldsymbol{k}}_{12})$ and $\tilde{W}_{l_1m_1l_2m_2l_3m_3}^{lml_2l_3}$. To find this association, working in terms of the perturbations in real space is advantageous as it facilitates the identification of this relation. Starting from equation (5.20), we can derive that

$$a_{lm} = -\frac{12\pi}{5}\,i^l\int\frac{d^3\boldsymbol{k}}{(2\pi)^3}Y_{lm}^*(\hat{\boldsymbol{k}})\Delta_l(k)\int d^3\boldsymbol{x}\,e^{-i\boldsymbol{x}\cdot\boldsymbol{k}}\zeta(\boldsymbol{x})\,, \tag{5.25}$$

expanding the exponential using expression (3.8), we obtain that

$$\begin{aligned}
a_{lm} &= -\frac{12\pi}{5}\,i^l\int\frac{d^3\boldsymbol{k}}{(2\pi)^3}Y_{lm}^*(\hat{\boldsymbol{k}})\Delta_l(k)\int d^3\boldsymbol{x}\,4\pi\sum_{l'm'}(-i)^{l'}j_{l'}(kr)Y_{l'm'}(\hat{\boldsymbol{k}})Y_{l'm'}^*(\hat{\boldsymbol{n}})\zeta(\boldsymbol{x})\\
&= -\frac{6}{5\pi}\int d\Omega(\hat{\boldsymbol{n}})Y_{lm}^*(\hat{\boldsymbol{n}})\int_0^\infty drr^2\int_0^\infty dkk^2\Delta_l(k)j_l(kx)\zeta(r,\hat{\boldsymbol{n}})\\
&= -\frac{6}{5\pi}\int d\Omega(\hat{\boldsymbol{n}})Y_{lm}^*(\hat{\boldsymbol{n}})\int_0^\infty drr^2D_l(r)\zeta(r,\hat{\boldsymbol{n}})\,,
\end{aligned} \tag{5.26}$$

here, we have made a change of coordinates from Cartesian to spherical coordinates, where $\boldsymbol{x} = (r,\hat{\boldsymbol{n}})$. Additionally, we can define the transfer function in real space and the curvature perturbation ζ, respectively, as follows

$$D_l(r) = \int_0^\infty dk k^2 \Delta_l(k) j_l(kr)\,, \tag{5.27}$$

$$\zeta(r, \hat{\boldsymbol{n}}) = \sum_{lm} \zeta_{lm}(r) Y_{lm}(\hat{\boldsymbol{n}})\,, \tag{5.28}$$

replacing (5.28) into (5.26), we find that

$$a_{lm} = -\frac{6}{5\pi} \int_0^\infty dr r^2\, D_l(r)\, \zeta_{lm}(r)\,. \tag{5.29}$$

In order to establish a correlation between the phenomenological model and the curvature perturbation in real space, we can employ the relationship (5.23). Subsequently, we substitute the expression (5.26), leading to

$$\begin{aligned} a_{lm}^{NG} = \beta a_{lm}^{F} = -\beta \left(\frac{6}{5\pi}\right)^3 \sum_{\substack{l_i m_i \\ i=1,2,3}} \tilde{W}^{l m l_2 l_3}_{l_1 m_1 l_2 m_2 l_3 m_3} \prod_{j=1}^{3} \int d^3\boldsymbol{x_j} Y^*_{l_1 m_1}(\hat{\boldsymbol{n}}_{\boldsymbol{1}}) D_{l_1}(r_1) \\ \times Y^*_{l_2 m_2}(\hat{\boldsymbol{n}}_{\boldsymbol{2}}) D_{l_2}(r_2) Y^*_{l_3 m_3}(\hat{\boldsymbol{n}}_{\boldsymbol{3}})\, D_{l_3}(r_3)\, \zeta_G(\boldsymbol{x_1})\, \zeta_G(\boldsymbol{x_2})\, \zeta_G(\boldsymbol{x_3})\,. \end{aligned} \tag{5.30}$$

On the other hand, using equation (5.26) and substituting the cubic-order definition of the curvature perturbation ζ derived from equation (5.15), we can determine that

$$\begin{aligned} a_{lm}^{NG} = -\frac{6}{5\pi} g_{NL} \int d\Omega(\hat{\boldsymbol{n}}) Y^*_{lm}(\hat{\boldsymbol{n}}) \int_0^\infty dr r^2 D_l(r) \\ \times \prod_{j=1}^{3} \int d^3\boldsymbol{x_j} \mathcal{W}(\tilde{\boldsymbol{x}}_{\boldsymbol{1}}, \tilde{\boldsymbol{x}}_{\boldsymbol{2}}, \tilde{\boldsymbol{x}}_{\boldsymbol{3}}) \zeta_G(\boldsymbol{x_1}) \zeta_G(\boldsymbol{x_2}) \zeta_G(\boldsymbol{x_3})\,, \end{aligned} \tag{5.31}$$

where $\tilde{\boldsymbol{x}}_{\boldsymbol{i}} = \boldsymbol{x_i} - \boldsymbol{x}$. We can use the definition $a_{lm}^{NG} = \beta a_{lm}^{F}$ to relate both of the previous expressions (5.30) and (5.31),

$$\begin{aligned} -\beta \left(\frac{6}{5\pi}\right)^3 \sum_{\substack{l_i m_i \\ i=1,2,3}} \tilde{W}^{l m l_2 l_3}_{l_1 m_1 l_2 m_2 l_3 m_3} \prod_{j=1}^{3} \int d^3\boldsymbol{x_j} Y^*_{l_j m_j}(\hat{\boldsymbol{n}}_{\boldsymbol{j}}) D_{l_j}(r_j) \zeta_G(\boldsymbol{x_j}) = \\ -\frac{6}{5\pi} g_{NL} \int d\Omega(\hat{\boldsymbol{n}}) Y^*_{lm}(\hat{\boldsymbol{n}}) \int_0^\infty dr r^2 D_l(r) \prod_{j=1}^{3} \int d^3\boldsymbol{x_j} \mathcal{W}(\tilde{\boldsymbol{x}}_{\boldsymbol{1}}, \tilde{\boldsymbol{x}}_{\boldsymbol{2}}, \tilde{\boldsymbol{x}}_{\boldsymbol{3}}) \zeta_G(\boldsymbol{x_j})\,, \end{aligned} \tag{5.32}$$

by comparing the two sides of the equality, we can propose the following form for the integral kernel. Equation (5.33) is a guess, as the equivalence of the integrands is not guaranteed, although the equality of the integrals remains valid,

$$\begin{aligned}\mathcal{W}(\tilde{\boldsymbol{x}}_{\mathbf{1}},\tilde{\boldsymbol{x}}_{\mathbf{2}},\tilde{\boldsymbol{x}}_{\mathbf{3}}) = \sum_{\substack{l_i m_i \\ i=1,2,3}} & Y^*_{l_1m_1}(\hat{\boldsymbol{n}}_{\mathbf{1}})D_{l_1}(r_1)\,Y^*_{l_2m_2}(\hat{\boldsymbol{n}}_{\mathbf{2}})D_{l_2}(r_2)\times \\ & \qquad Y^*_{l_3m_3}(\hat{\boldsymbol{n}}_{\mathbf{3}})D_{l_3}(r_3)\,F^{l_1m_1l_2m_2l_3m_3}(\boldsymbol{x})\,. \end{aligned} \tag{5.33}$$

The function $F^{l_1m_1l_2m_2l_3m_3}(\boldsymbol{x})$ constitutes the part of the kernel that contains the information about the filters applied to the temperature field, thereby generating CMB anomalies. It also provides insights into the convolutional operations acting on the primordial curvature perturbation on the LSS. Furthermore, the integral kernel $\mathcal{W}$ simplifies into an angular convolution when our observations are restricted to a fixed distance r, and the transfer functions $D_l(r)$ convey the physics encapsulated within the kernel to the observer. Consequently, the kernel satisfies the following relationship

$$\tilde{W}^{lml_2l_3}_{l_1m_1l_2m_2l_3m_3} = \int d\Omega(\hat{\boldsymbol{n}})Y^*_{lm}(\hat{\boldsymbol{n}})\int_0^\infty dr\,r^2\,D_l(r)\,F^{l_1m_1l_2m_2l_3m_3}(\boldsymbol{x})\,, \tag{5.34}$$

where the function F can be expanded in spherical harmonics as follows

$$F^{l_1m_1l_2m_2l_3m_3}(\boldsymbol{x}) = \sum_{l_4m_4} F^{l_1m_1l_2m_2l_3m_3}_{l_4m_4}(r)\,Y_{l_4m_4}(\hat{\boldsymbol{n}})\,,$$

plugging the expression of F in equation (5.34), we obtain that

$$\int_0^\infty dr\,r^2\,D_l(r)\,F^{l_1m_1l_2m_2l_3m_3}_{lm}(r) = \tilde{W}^{lml_2l_3}_{l_1m_1l_2m_2l_3m_3}\,. \tag{5.35}$$

We further simplify the above expression by computing the transfer function D_l in a convenient way, using the Sachs-Wolfe approximation $\Delta_l(k) = \frac{1}{3}j_l(kr_{dec})$. Then

$$\begin{aligned} D_l(r) &= \int_0^\infty dkk^2 j_l(kr)\Delta_l(k) \\ &= \frac{1}{3}\int_0^\infty dkk^2 j_l(kr)j_l(kr_{dec}) \\ &= \frac{\pi}{6\,r^2}\,\delta(r-r_{dec})\,, \end{aligned} \tag{5.36}$$

where we applied the property of the Bessel function, as given in (3.34). Replacing equation (5.36) into (5.35), we obtain an expression that relates the kernel component to the filters at the position of the LSS,

$$F^{l_1m_1l_2m_2l_3m_3}_{lm}(r_{dec}) = \frac{6}{\pi}\,\tilde{W}^{lml_2l_3}_{l_1m_1l_2m_2l_3m_3}\,. \tag{5.37}$$

The previous result is a specific case focused on the LSS. However, this expression can be applied to any distance r. Working with the LSS is advantageous because when the perturbation re-enters the horizon before decoupling, it leaves a distinct footprint on the Last Scattering Surface, which subsequently affects the CMB photons. Furthermore, equation (5.37) provides insights into the behavior of the $\mathcal{O}(g_{NL})$ term, giving the form of the filters, as presented in figure 5.1. Notably, the $\mathcal{O}(g_{NL})$ term tends to zero when $l_2, l_3 > 30$ or $l > 1500$.

On the other hand, let's now turn our attention to determining the form of the kernel in Fourier space for the toy model. By taking the Fourier transform of the expression (5.15), we obtain

$$\begin{aligned}
\zeta(\boldsymbol{k})|_{\mathcal{O}(g_{NL})} &= g_{NL} \prod_{j=1}^{3} \prod_{q=1}^{3} \int d^3\boldsymbol{x}_j d^3\boldsymbol{x} \int \frac{d^3\boldsymbol{k}_q}{(2\pi)^3} \mathcal{W}(\boldsymbol{x}_1 - \boldsymbol{x}, \boldsymbol{x}_2 - \boldsymbol{x}, \boldsymbol{x}_3 - \boldsymbol{x}) e^{i\boldsymbol{k}_1 \cdot \boldsymbol{x}_1} \\
&\times e^{i\boldsymbol{k}_2 \cdot \boldsymbol{x}_2} e^{i\boldsymbol{k}_3 \cdot \boldsymbol{x}_3} e^{-i\boldsymbol{k} \cdot \boldsymbol{x}} \zeta_G(\boldsymbol{k}_1)\zeta_G(\boldsymbol{k}_2)\zeta_G(\boldsymbol{k}_3) \\
&= g_{NL} \sum_{\substack{l_i m_i \\ i=1,2,3}} \prod_{j,q=1}^{3} \int d^3\boldsymbol{x}_j d^3\boldsymbol{x} \int \frac{d^3\boldsymbol{k}_q}{(2\pi)^3} e^{i\boldsymbol{k}_1 \cdot \boldsymbol{x}_1} e^{i\boldsymbol{k}_2 \cdot \boldsymbol{x}_2} e^{i\boldsymbol{k}_3 \cdot \boldsymbol{x}_3} e^{-i\boldsymbol{k} \cdot \boldsymbol{x}} F^{l_1 \dots m_3}(\boldsymbol{x}) \\
&\times Y^*_{l_1 m_1}(\hat{\boldsymbol{n}}_1) D_{l_1}(r_1) Y^*_{l_2 m_2}(\hat{\boldsymbol{n}}_2) D_{l_2}(r_2) Y^*_{l_3 m_3}(\hat{\boldsymbol{n}}_3) D_{l_3}(r_3) \zeta_G(\boldsymbol{k}_1)\zeta_G(\boldsymbol{k}_2)\zeta_G(\boldsymbol{k}_3) \\
&= g_{NL}(4\pi)^3 \sum_{\substack{l_i m_i \\ i=1,2,3}} \sum_{\substack{L_i M_i \\ i=1,2,3}} \prod_{j,q=1}^{3} \int d^3\boldsymbol{x}_j \frac{d^3\boldsymbol{k}_q}{(2\pi)^3} F^{l_1 \dots m_3}(\boldsymbol{k}) Y^*_{l_1 m_1}(\hat{\boldsymbol{n}}_1) D_{l_1}(r_1) \\
&\times Y^*_{l_2 m_2}(\hat{\boldsymbol{n}}_2) D_{l_2}(r_2) Y^*_{l_3 m_3}(\hat{\boldsymbol{n}}_3) D_{l_3}(r_3) Y^*_{L_1 M_1}(\hat{\boldsymbol{k}}_1) Y_{L_1 M_1}(\hat{\boldsymbol{n}}_1) Y^*_{L_2 M_2}(\hat{\boldsymbol{k}}_2) \\
&\times Y_{L_2 M_2}(\hat{\boldsymbol{n}}_2) Y^*_{L_3 M_3}(\hat{\boldsymbol{k}}_3) Y_{L_3 M_3}(\hat{\boldsymbol{n}}_3) j_{L_1}(k_1 r_1) j_{L_2}(k_2 r_2) j_{L_3}(k_3 r_3) \\
&\times \zeta_G(\boldsymbol{k}_1)\zeta_G(\boldsymbol{k}_2)\zeta_G(\boldsymbol{k}_3) ,
\end{aligned} \tag{5.38}$$

after applying the properties of the Bessel functions, the expression becomes

$$\begin{aligned}
\zeta(\boldsymbol{k})|_{\mathcal{O}(g_{NL})} = g_{NL} \sum_{\substack{l_i m_i \\ i=1,2,3}} i^{l_1+l_2+l_3} \prod_{q=1}^{3} \int \frac{d^3\boldsymbol{k}_q}{(2\pi)^3} F^{l_1 \dots m_3}(\boldsymbol{k}) \zeta_G(\boldsymbol{k}_q) \\
\times Y^*_{l_1 m_1}(\hat{\boldsymbol{k}}_1) D_{l_1}(k_1) \dots Y^*_{l_3 m_3}(\hat{\boldsymbol{k}}_3) D_{l_3}(k_3) ,
\end{aligned} \tag{5.39}$$

note that the function F can be expressed as

$$\begin{aligned}
F^{l_1 \dots m_3}(\boldsymbol{k}) &= \int d^3\boldsymbol{x} e^{-i\boldsymbol{k} \cdot \boldsymbol{x}} F^{l_1 \dots m_3}(\boldsymbol{x}) \\
&= \sum_{lm} Y_{lm}(\hat{\boldsymbol{k}}) F^{l_1 \dots m_3}(k) .
\end{aligned} \tag{5.40}$$

Moreover, in the Sach-Wolfe approximation, equation (5.39), takes the following form

$$\begin{aligned}\zeta(\boldsymbol{k})|_{\mathcal{O}(g_{NL})} = \left(\frac{1}{3}\right)^3 g_{NL} \sum_{\substack{l_i m_i\\ i=1,2,3}} i^{l_1+l_2+l_3} \prod_{q=1}^{3} \int \frac{d^3\boldsymbol{k}_q}{(2\pi)^3} F^{l_1...m_3}(\boldsymbol{k})\zeta_G(\boldsymbol{k}_q) \\ \times Y^*_{l_1 m_1}(\hat{\boldsymbol{k}}_{\boldsymbol{1}}) j_{l_1}(r_{dec}k_1)...Y^*_{l_3 m_3}(\hat{\boldsymbol{k}}_{\boldsymbol{3}}) j_{l_3}(r_{dec}k_3)\,.\end{aligned} \tag{5.41}$$

On the other hand, taking the Fourier transform of the definition of ζ in real space leads to

$$\begin{aligned}\zeta(\boldsymbol{k})|_{\mathcal{O}(g_{NL})} &= g_{NL} \int d^3\boldsymbol{x} e^{-i\boldsymbol{k}\cdot\boldsymbol{x}} \prod_{j=1}^{3} \int d^3\boldsymbol{x}_j \mathcal{W}(\boldsymbol{x}_1 - \boldsymbol{x}, \boldsymbol{x}_2 - \boldsymbol{x}, \boldsymbol{x}_3 - \boldsymbol{x}) \\ &\times \prod_{q=1}^{3} \int \frac{d^3\boldsymbol{k}_q}{(2\pi)^3} e^{i\sum_{j=1}^{3} \boldsymbol{x}_j\cdot\boldsymbol{k}_j} \zeta_G(\boldsymbol{k}_1)\zeta_G(\boldsymbol{k}_2)\zeta_G(\boldsymbol{k}_3) \\ &= g_{NL} \prod_{q=1}^{3} \int \frac{d^3\boldsymbol{k}_q}{(2\pi)^3} \tilde{\mathcal{W}}(\boldsymbol{k}, \boldsymbol{k}_1, \boldsymbol{k}_2, \boldsymbol{k}_3)\zeta_G(\boldsymbol{k}_1)\zeta_G(\boldsymbol{k}_2)\zeta_G(\boldsymbol{k}_3)\,,\end{aligned} \tag{5.42}$$

where the kernel is defined as follows

$$\tilde{\mathcal{W}}(\boldsymbol{k}, \boldsymbol{k}_1, \boldsymbol{k}_2, \boldsymbol{k}_3) = \int d^3\boldsymbol{x} e^{-i\boldsymbol{k}\cdot\boldsymbol{x}} \prod_{j=1}^{3} \int d^3\boldsymbol{x}_j \mathcal{W}(\tilde{\boldsymbol{x}}_{\boldsymbol{1}}, \tilde{\boldsymbol{x}}_{\boldsymbol{2}}, \tilde{\boldsymbol{x}}_{\boldsymbol{3}})\,. \tag{5.43}$$

Comparing equations (5.39) and (5.42), we obtain that the kernel is given by

$$\begin{aligned}\tilde{\mathcal{W}}(\boldsymbol{k}, \boldsymbol{k}_1, \boldsymbol{k}_2, \boldsymbol{k}_3) = \sum_{\substack{l_i m_i\\ i=1,2,3}} \sum_{lm} i^{l_1+l_2+l_3} F^{l_1...m_3}_{lm}(k) Y_{lm}(\hat{\boldsymbol{k}}) \\ \times Y^*_{l_1 m_1}(\hat{\boldsymbol{k}}_{\boldsymbol{1}}) D_{l_1}(k_1)...Y^*_{l_3 m_3}(\hat{\boldsymbol{k}}_{\boldsymbol{3}}) D_{l_3}(k_3)\,.\end{aligned} \tag{5.44}$$

The preceding expression defines the integral kernel in Fourier space, and it exhibits similarities with the expression provided in equation (5.33). It is important to note that both equations are complex, making it non-trivial to extract insights about the convolution inherent in this type of model through these formulations.

5.4 Second approach: filtered curvature perturbation

In the previous section, we developed a method to reconstruct the curvature perturbation starting from the phenomenological map of the temperature field, as shown in expression (5.1). This procedure aims to establish a relationship between the convolution kernel and the filters applied to the a_{lm} coefficients of the filtered temperature field, equations (5.33) and (5.44). However, we noted that these relationships have intrinsic limitations that make it difficult to extract information, such as the presence of transfer functions.

In this section, our goal is to directly reconstruct the curvature perturbation ζ in Fourier space. Unlike the previous method, this approach allows us to derive the expression without evaluating it on the surface of the last scattering. The methodology involves finding an expression for ζ by applying the same filters proposed for the temperature field. Thus, when we apply a filter to a specific temperature field, we are simultaneously applying a filter to the perturbation responsible for generating that part of the temperature.

In the toy model presented in equation (5.1), the filters g_l and w_l are given in harmonic space. In this case, we define two filters analogous to the previously encountered filters, but now tailored to rescale $g(k)$ and $w(k)$ in Fourier space. Starting with $w(k)$, we can define the filtered curvature perturbation as

$$\zeta_F(\boldsymbol{k}) = w(k)\zeta_G(\boldsymbol{k})\,, \tag{5.45}$$

where $w(k)$ (equivalent to w_l) is the filter function applied to the low multiples (large scales) and approaches zero for $l > 30$, as illustrated in figure 5.1.

Additionally, the Fourier transform of ζ in real space is

$$\zeta_F(\boldsymbol{x}) = \int \frac{d^3\boldsymbol{k}}{(2\pi)^3} e^{i\boldsymbol{k}\cdot\boldsymbol{x}} \zeta_G(\boldsymbol{k}) w(k)\,. \tag{5.46}$$

In the following steps, we can repeat the process we employed in the previous section with a_{lm}. We wrote the cubic term in Fourier space and applied a second filter, $g_l(k)$, which filters out high multiples (small scales) and becomes zero for $l > 1500$. Then,

$$\zeta_{NG}(\boldsymbol{x}) = \zeta_G(\boldsymbol{k}) + \beta\, \zeta_F^3(\boldsymbol{k})\,, \tag{5.47}$$

where

$$\begin{aligned} \zeta_F^3(\boldsymbol{k}) &= \int d^3\boldsymbol{x} e^{-i\boldsymbol{k}\cdot\boldsymbol{x}} \zeta_G(\boldsymbol{x}) \zeta_F^2(\boldsymbol{x}) \\ &= \int d^3\boldsymbol{x} e^{-i\boldsymbol{k}\cdot\boldsymbol{x}} \prod_{j=1}^{3} \int \frac{d^3\boldsymbol{k}_j}{(2\pi)^3} e^{i\boldsymbol{k}_j\cdot\boldsymbol{x}} w(k_1) w(k_2) \zeta_G(\boldsymbol{k}_1) \zeta_G(\boldsymbol{k}_2) \zeta_G(\boldsymbol{k}_3)\,, \end{aligned} \tag{5.48}$$

$$\zeta_F^3(\boldsymbol{k}) = \prod_{j=1}^{2}\int \frac{d^3\boldsymbol{k}_j}{(2\pi)^3} w(k_1)w(k_2)\zeta_G(\boldsymbol{k}_1)\zeta_G(\boldsymbol{k}_2)\zeta_G(\boldsymbol{k}-\boldsymbol{k}_1-\boldsymbol{k}_2)\,. \tag{5.49}$$

Finally, we incorporate the filter $g(k)$ to fully replicate the toy model

$$g(k)\zeta_F^3(\boldsymbol{k}) = \prod_{j=1}^{2}\int \frac{d^3\boldsymbol{k}_j}{(2\pi)^3} w(k_1)w(k_2)g(k)\zeta_G(\boldsymbol{k}_1)\zeta_G(\boldsymbol{k}_2)\zeta_G(\boldsymbol{k}-\boldsymbol{k}_1-\boldsymbol{k}_2)\,. \tag{5.50}$$

Comparing the above expression multiplied by β, with equation (5.16), we observe that

$$\beta = g_{NL} \text{ and } \tilde{\mathcal{W}}(\boldsymbol{k}_1,\, \boldsymbol{k}_2,\, \boldsymbol{k}-\boldsymbol{k}_1-\boldsymbol{k}_2) \equiv g(k)\, w(k_1)\, w(k_2)\,. \tag{5.51}$$

As we mentioned earlier, the filter $w(k)$ is designed to remove information from large scales (small k) and low multiples, while $g(k)$ filters out information on small scales (large k) and high multiples, for examples of filter shapes, see Hansen et al. (2019). Consequently, we consider the condition that $k \gg k_1, k_2$.

This approach is important because it simplifies the integral kernel expression found in the definition of the curvature perturbation. Thus,

$$g(k)\, w(k_1)\, w(k_2) = \prod_{i=1}^{3}\int d^3\boldsymbol{x}_i \mathcal{W}(\boldsymbol{x}_1, \boldsymbol{x}_2, \boldsymbol{x}_3) e^{i\boldsymbol{k}_1\cdot\boldsymbol{x}_1} e^{i\boldsymbol{k}_2\cdot\boldsymbol{x}_2} e^{i\tilde{\boldsymbol{k}}_{12}\cdot\boldsymbol{x}_3}\,. \tag{5.52}$$

The results presented in this chapter reveal a potential connection between the phenomenological model described by (5.1) and inflationary models where local non-Gaussianity with a strong scale dependence can induce non-Gaussian behavior in the temperature field. This non-Gaussianity has been represented as a convolution involving three perturbations, including the cubic-order term (g_{NL} term). Furthermore, we have established a relationship between the k modes of each perturbation, as given by equation (5.51). Additionally, we have determined the link between the integral kernel and filters, as in equation (5.37), providing insights into the type of convolution involved in the curvature perturbations ζ_G.

These outcomes serve as a starting point for understanding the conditions that the underlying inflationary model that gives rise to the toy model must satisfy. To explore these conditions further, we will examine the four-point correlation function, or trispectrum, in Fourier space.

5.4.1 Filters in Fourier space

To relate the filters in terms of the multiples moment l with the wavenumber k, we assume that the shape of the filters remains the same, but we need to find the relationship between a given l and a specific k mode. To do this, we consider two CMB photons, one hot and one cold, separated by a comoving distance $\lambda \sim k^{-1}$. These photons travel from recombination to the present time, starting with an angular separation θ. We can then define

$$d_L \theta \sim k^{-1} \longrightarrow \theta \sim \frac{k^{-1}}{\eta_0 - \eta_*} , \tag{5.53}$$

the linear distance between the photons can be approximated by the angular distance between them, where $d_L = \eta_0 - \eta_*$. Here, η_0 corresponds to the present time or the time of observation, while η_* represents an earlier epoch, such as the time of recombination. Furthermore, we know that in the CMB, the angular separation is $\theta \sim l^{-1}$, leading to

$$l \propto k(\eta_0 - \eta_*) , \tag{5.54}$$

where l represents the multipole moment, which is linked to the angular scale of fluctuations in the CMB. It quantifies the number of oscillations within a given angle in the sky. While, k represents the wavenumber, and characterizes the spatial scale or frequency of the fluctuations.

Following the results in Hansen et al. (2019) and using the relation in equation (5.54), we obtained the values presented in figure 5.2, where we have assumed that $\eta_0 = 14000$ Mpc and $\eta_* = 114$ Mpc.

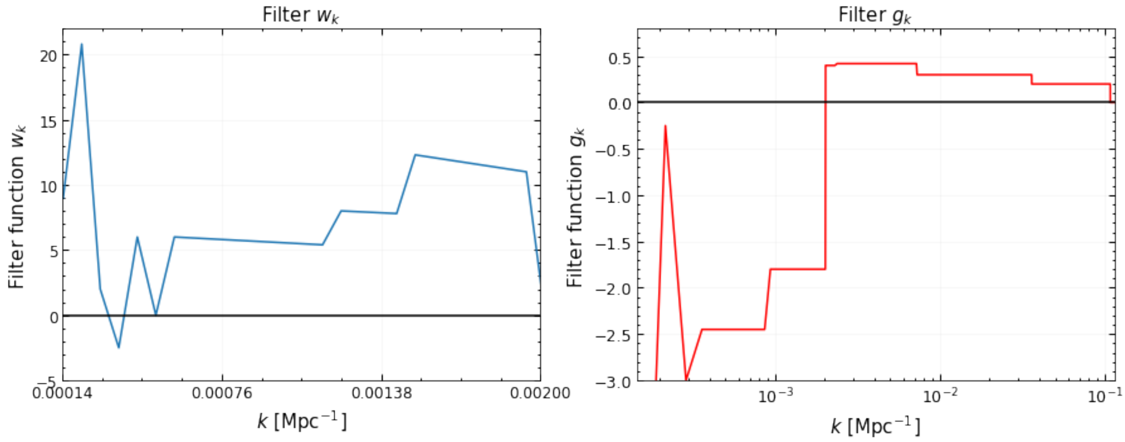

Figure 5.2: Filters $w(k)$ and $g(k)$ are plotted in the ranges $k = (1.4 \times 10^{-4}, 2 \times 10^{-3})\text{Mpc}^{-1}$ and $k = (1.4 \times 10^{-4}, 10^{-1})\text{Mpc}^{-1}$, respectively.

Chapter 6

Toy Model Trispectrum

The previous chapter has provided us with valuable insights into the connection between the temperature field of the toy model and the inflationary curvature perturbation, as introduced by Hansen et al. (2019). This understanding serves as a crucial foundation for uncovering the underlying physical model behind the proposed toy model.

Now, as we shift our focus toward investigating the impact of non-Gaussianity in our model, it becomes necessary to delve into higher-order statistics to understand the characteristics of the CMB radiation. Specifically, our interest lies in a g_{NL}-type non-Gaussian model with strong scale dependence, particularly at cubic order in the variable ζ. Working with the 4-point correlation function, known as the trispectrum in Fourier space, is useful to accomplish this.

The trispectrum, when expressed in Fourier space, not only provides statistical information about the correlation of four points in space, but also offers insights into the specific configuration that the four k modes must adhere to in order to form a closed quadrilateral in Fourier space.

In this chapter, we will work on a detailed calculation of the trispectrum associated with the toy model presented in Chapter 5. We will highlight the relevant equations and elucidate the key characteristics of this trispectrum.

6.1 Primordial trispectrum of ζ

The trispectrum is the connected part[1] of the four-point correlation function in Fourier space. It becomes non-zero when four $\boldsymbol{k}$ vectors form a closed quadrilateral, but one should keep in mind that these sets of four $\boldsymbol{k}$ vectors do not necessarily lie on the same plane. Note that the trispectrum is the lowest-order correlation where the connected part needs to be explicitly separated from the unconnected part. In other words, the ensemble average of four Fourier modes, where their $\boldsymbol{k}$ vectors form a closed quadrilateral, would generally not be zero even for a Gaussian random field. However, what provides additional information beyond the power spectrum is the connected part of that statistic (Verde and Heavens 2001; Gualdi et al. 2021).

To the lowest order in curvature perturbation ζ, the trispectrum is given by

$$\begin{aligned}\langle\zeta_1\,\zeta_2\,\zeta_3\,\zeta_4\rangle_c = {} & \langle\zeta_1^{NG}\,\zeta_2^{G}\,\zeta_3^{G}\,\zeta_4^{G}\rangle_c + \langle\zeta_1^{G}\,\zeta_2^{NG}\,\zeta_3^{G}\,\zeta_4^{G}\rangle_c \\ & + \langle\zeta_1^{G}\,\zeta_2^{G}\,\zeta_3^{NG}\,\zeta_4^{G}\rangle_c + \langle\zeta_1^{G}\,\zeta_2^{G}\,\zeta_3^{G}\,\zeta_4^{NG}\rangle_c\,,\end{aligned} \tag{6.1}$$

it is important to notice that the curvature perturbation ζ is defined as a combination of both Gaussian and non-Gaussian contributions, resembling the toy model structure in terms of the temperature field, where the non-Gaussian contribution is given by equation (5.16). It follows that

$$\zeta(\boldsymbol{k}) = \zeta_G(\boldsymbol{k}) + g_{NL}\,\zeta_{NG}(\boldsymbol{k})\,. \tag{6.2}$$

In particular, the leading order contributions to the connected part of the 4-point function come from terms such as

$$\langle\zeta_G(\boldsymbol{k_1})\zeta_G(\boldsymbol{k_2})\zeta_G(\boldsymbol{k_3})\zeta_{NG}(\boldsymbol{k_4})\rangle_c = (2\pi)^3\delta(\boldsymbol{k_1}+\boldsymbol{k_2}+\boldsymbol{k_3}+\boldsymbol{k_4})T_\zeta(\boldsymbol{k_1},\boldsymbol{k_2},\boldsymbol{k_3},\boldsymbol{k_4})\,. \tag{6.3}$$

It is important to keep in mind that the total contribution to $\langle\zeta_1\zeta_2\zeta_3\zeta_4\rangle_c$ is the sum of the contribution from all the terms presented in equation (6.1). In our case, we focus on the analysis of one particular arrangement given by expression (6.3) because the other contributions can be formed by permuting the symbols.

---

[1] The connected part of the trispectrum refers to the component that contains the signal that is sensitive to non-Gaussian features.

By substituting the definition of ζ in the ensemble average, we obtain that

$$\begin{aligned}\langle \zeta_G(\boldsymbol{k_1})\zeta_G(\boldsymbol{k_2})\zeta_G(\boldsymbol{k_3})\zeta_{NG}(\boldsymbol{k_4})\rangle = g_{NL}\int \frac{d^3\boldsymbol{k}_5}{(2\pi)^3}\frac{d^3\boldsymbol{k}_6}{(2\pi)^3}\tilde{\mathcal{W}}(\boldsymbol{k}_5,\boldsymbol{k}_6,\tilde{\boldsymbol{k}}_{56})\\ \langle \zeta_G(\boldsymbol{k}_1)\,\zeta_G(\boldsymbol{k}_2)\,\zeta_G(\boldsymbol{k}_3)\,\zeta_G(\boldsymbol{k}_5)\,\zeta_G(\boldsymbol{k}_6)\,\zeta_G(\boldsymbol{k}_4-\boldsymbol{k}_5-\boldsymbol{k}_6)\rangle\,, \end{aligned}\tag{6.4}$$

where we have defined that $\tilde{\boldsymbol{k}}_{56}=\boldsymbol{k}_4-\boldsymbol{k}_5-\boldsymbol{k}_6$. To compute the ensemble average containing the six curvature perturbation contributions, we employ the Wick theorem [2] that allows us to decompose this computation. As a result, one possible combination for computing the two-point correlation functions can be expressed as follows

$$\begin{aligned}&= g_{NL}\int \frac{d^3\boldsymbol{k}_5}{(2\pi)^3}\frac{d^3\boldsymbol{k}_6}{(2\pi)^3}\tilde{\mathcal{W}}(\boldsymbol{k}_5,\boldsymbol{k}_6,\tilde{\boldsymbol{k}}_{56})\Big[\langle\zeta_G(\boldsymbol{k}_1)\,\zeta_G(\boldsymbol{k}_2)\rangle\langle\zeta_G(\boldsymbol{k}_3)\zeta_G(\boldsymbol{k}_5)\rangle\\
&\langle\zeta_G(\boldsymbol{k}_6)\,\zeta_G(\boldsymbol{k}_4-\boldsymbol{k}_5-\boldsymbol{k}_6)\rangle+\langle\zeta_G(\boldsymbol{k}_1)\,\zeta_G(\boldsymbol{k}_5)\rangle\langle\zeta_G(\boldsymbol{k}_3)\zeta_G(\boldsymbol{k}_4-\boldsymbol{k}_5-\boldsymbol{k}_6)\rangle\\
&\times\langle\zeta_G(\boldsymbol{k}_2)\zeta_G(\boldsymbol{k}_6)\rangle+perm.\Big]\\
&= g_{NL}\int \frac{d^3\boldsymbol{k}_5}{(2\pi)^3}\frac{d^3\boldsymbol{k}_6}{(2\pi)^3}\tilde{\mathcal{W}}(\boldsymbol{k}_5,\boldsymbol{k}_6,\tilde{\boldsymbol{k}}_{56})\Big[(2\pi)^9\delta^3(\boldsymbol{k_1}+\boldsymbol{k_2})\delta^3(\boldsymbol{k_3}+\boldsymbol{k_5})\delta^3(\boldsymbol{k_4}-\boldsymbol{k_5})\\
&\times P_\zeta(k_1)P_\zeta(k_3)P_\zeta(k_6)+(2\pi)^9\delta^3(\boldsymbol{k_1}+\boldsymbol{k_5})\delta^3(\boldsymbol{k_3}+\boldsymbol{k_4}-\boldsymbol{k_5}-\boldsymbol{k_6})\delta^3(\boldsymbol{k_2}+\boldsymbol{k_6})\\
&\times P_\zeta(k_1)P_\zeta(k_3)P_\zeta(k_2)+perm.\Big]\\
&=(2\pi)^3 g_{NL}\int d^3\boldsymbol{k}_6\tilde{\mathcal{W}}(\boldsymbol{k}_4,\boldsymbol{k}_6,\tilde{\boldsymbol{k}}_{46})\delta^3(\boldsymbol{k_1}+\boldsymbol{k_2})\delta^3(\boldsymbol{k_3}+\boldsymbol{k_4})P_\zeta(k_1)P_\zeta(k_3)P_\zeta(k_6)+\\
&(2\pi)^3\delta^3(\boldsymbol{k_1}+\boldsymbol{k_2}+\boldsymbol{k_3}+\boldsymbol{k_4})g_{NL}\,\tilde{\mathcal{W}}(-\boldsymbol{k}_1,-\boldsymbol{k}_2,\tilde{\boldsymbol{k}}_{12})P_\zeta(k_1)P_\zeta(k_2)P_\zeta(k_3)+perm.\,,\end{aligned}\tag{6.5}$$

where we have applied the definition of the two-point correlation function in terms of the power spectrum, equation (2.36). From the last line, we notice that the first term is an unconnected part (as can be seen from Dirac's deltas) of the four-point correlation function because the Gaussian part involves products of two Dirac delta functions, whereas the connected part has only one (Verde and Heavens 2001). This implies that we need combinations of the Gaussian field with the fields contained in the non-gaussian definition in order to obtain the connected components. Thus, the connected part for this specific arrangement can be written as

$$\begin{aligned}\langle\zeta_G(\boldsymbol{k_1})\zeta_G(\boldsymbol{k_2})\zeta_G(\boldsymbol{k_3})\zeta_{NG}(\boldsymbol{k_4})\rangle_c=(2\pi)^3\delta^3(\boldsymbol{k_1}+\boldsymbol{k_2}+\boldsymbol{k_3}+\boldsymbol{k_4})g_{NL}\tilde{\mathcal{W}}(-\boldsymbol{k}_1,-\boldsymbol{k}_2,\tilde{\boldsymbol{k}}_{12})\\ \times P_\zeta(k_1)\,P_\zeta(k_2)\,P_\zeta(k_3)+perm.\,,\end{aligned}\tag{6.6}$$

---

[2] The Wick theorem states that any ensemble average of Gaussian random variables can be obtained by products of ensemble averages of pairs.

from equation (6.3) we can identify that,

$$T_\zeta(\boldsymbol{k}_1,\boldsymbol{k}_2,\boldsymbol{k}_3,\boldsymbol{k}_4) = g_{NL}\,\tilde{\mathcal{W}}(-\boldsymbol{k}_1,-\boldsymbol{k}_2,\,\tilde{\boldsymbol{k}}_{12})\,P_\zeta(k_1)\,P_\zeta(k_2)\,P_\zeta(k_3) + perm\,. \tag{6.7}$$

We can further simply the aforementioned expression, considering the last term of equation (6.5) from which we can extract the following relations

$$\boldsymbol{k}_5 = -\boldsymbol{k}_1 \;\longrightarrow\; k_5 = |\boldsymbol{k}_5|\,;\; k_1 = |-\boldsymbol{k}_1| \;\longrightarrow\; k_5 = k_1\,, \tag{6.8}$$

$$\boldsymbol{k}_6 = -\boldsymbol{k}_2 \;\longrightarrow\; k_6 = |\boldsymbol{k}_6|\,;\; k_2 = |-\boldsymbol{k}_2| \;\longrightarrow\; k_6 = k_2\,, \tag{6.9}$$

considering the definition of the kernel given in the previous chapter, equation (5.51), and using equations (6.8) and (6.9), this leads to

$$T_\zeta(k_1,k_2,k_3,k_4) = \; g_{NL}\,g(k_4)\,w(k_1)\,w(k_2)P_\zeta(k_1)\,P_\zeta(k_2)\,P_\zeta(k_3) + perm.\,, \tag{6.10}$$

where we have defined $\tilde{\mathcal{W}}(-\boldsymbol{k}_1,-\boldsymbol{k}_2,\,\tilde{\boldsymbol{k}}_{12}) \equiv g(k_4)w(k_1)w(k_2)$. It is worth highlighting that equation (6.10) resembles the primordial trispectrum found by Akrami et al. (2020a) for a local model. However, in our case, the g_{NL} parameter is scale-dependent, accounting for the presence of the filters in the expression.

On the other hand, figure 5.2 allows us to extract some additional information about the k modes associated with the filters g and w, then we have the following ranges

$$1.4\times10^{-4} \le k_1, k_2 \le 2\times10^{-3} \;\text{ and } 1.4\times10^{-4} \le k_4 \le 10^{-1}\,. \tag{6.11}$$

Otherwise, the filter w and g go to zero when $k > 2\times10^{-3}$ and $k > 10^{-1}$, respectively. Note that we cannot extract any information from the filters for the mode k_3. Additionally, we have the condition that $k_4 \gg k_5, k_6$, which implies that $k_4 \gg k_1, k_2$.

It is necessary to clarify that equation (6.10) represents only one possible term among the different permutations for the case $\langle\zeta_G(\boldsymbol{k_1})\zeta_G(\boldsymbol{k_2})\zeta_G(\boldsymbol{k_3})\zeta_{NG}(\boldsymbol{k_4})\rangle_c$. The general expression of the primordial trispectrum of ζ in our g_{NL}-type model with scale dependence due to the filters, can be expressed as follows

$$\begin{aligned}T_\zeta(k_1,k_2,k_3,k_4) = 2\,g_{NL}\Big[\,g(k_4)\,P_\zeta(k_1)\,P_\zeta(k_2)\,P_\zeta(k_3)\Big(w(k_1)\,w(k_2) + w(k_1)\,w(k_3)\\ + w(k_2)\,w(k_3)\Big) + 3\,perm.\Big]\,.\end{aligned} \tag{6.12}$$

The additional permutations can be obtained considering the other terms in the definition given by equation (6.1). In the case of considering the filters g and w as constant equal to 1 in our expression, we obtain the following instead

$$T_\zeta(k_1,k_2,k_3,k_4) = 6\, g_{NL}\Big[P_\zeta(k_1)\,P_\zeta(k_2)\,P_\zeta(k_3) + 3\,perm.\Big]\,. \tag{6.13}$$

The two equations (6.12) and (6.13) can be used to understand the type of model that we are implementing in this work. On one side, equation (6.13) reflects what is commonly known as the trispectrum of a local g_{NL}-shape non-Gaussian model, as seen in, e.g. Regan et al. (2015) and Akrami et al. (2020a). Meanwhile, equation (6.12), which considers the effect of the filters and embodies the properties of the phenomenological model, can be considered as a g_{NL}-like non-Gaussian model with strong scale dependence introduced by the filters.

6.1.1 Second approach

In this part, we expand explicitly all the terms involved in the connected contribution of equation (6.4), leading to

$$\begin{aligned}\langle\zeta_G(\boldsymbol{k_1})\zeta_G(\boldsymbol{k_2})\zeta_G(\boldsymbol{k_3})\zeta_{NG}(\boldsymbol{k_4})\rangle = g_{NL}\int\frac{d^3\boldsymbol{k}_5}{(2\pi)^3}\frac{d^3\boldsymbol{k}_6}{(2\pi)^3}\tilde{\mathcal{W}}(\boldsymbol{k}_5,\boldsymbol{k}_6,\tilde{\boldsymbol{k}}_{56})\\ \langle\zeta_G(\boldsymbol{k}_1)\,\zeta_G(\boldsymbol{k}_5)\rangle\langle\zeta_G(\boldsymbol{k}_3)\,\zeta_G(\boldsymbol{k}_{\tilde{56}})\rangle\langle\zeta_G(\boldsymbol{k}_2)\,\zeta_G(\boldsymbol{k}_6)\rangle + perm\,.\end{aligned} \tag{6.14}$$

Firstly, we apply the Wick theorem, and subsequently, we compute the two-point correlation functions,

$$\begin{aligned}\langle\zeta_G(\boldsymbol{k}_1)\,\zeta_G(\boldsymbol{k}_5)\rangle = 16\pi^2\sum_{\substack{l_i m_i\\ i=1,5}}(-i)^{l_1+l_5}(-1)^{m_1}\delta_{l_1 l_5}\delta_{-m_1 m_5}\int dr r^2 j_{l_1}(k_1 r)j_{l_5}(k_5 r)\\ \times P_\zeta(k_1)Y_{l_1 m_1}(\hat{\boldsymbol{k}}_1)Y_{l_5 m_5}(\hat{\boldsymbol{k}}_5)\,,\end{aligned} \tag{6.15}$$

$$\begin{aligned}\langle\zeta_G(\boldsymbol{k}_2)\,\zeta_G(\boldsymbol{k}_6)\rangle = 16\pi^2\sum_{\substack{l_i m_i\\ i=2,6}}(-i)^{l_2+l_6}(-1)^{m_2}\delta_{l_2 l_6}\delta_{-m_2 m_6}\int dr r^2 j_{l_2}(k_2 r)j_{l_6}(k_6 r)\\ \times P_\zeta(k_2)Y_{l_2 m_2}(\hat{\boldsymbol{k}}_2)Y_{l_6 m_6}(\hat{\boldsymbol{k}}_6)\,,\end{aligned} \tag{6.16}$$

$$\begin{aligned}\langle\zeta_G(\boldsymbol{k}_3)\,\zeta_G(\tilde{\boldsymbol{k}}_{56})\rangle = 256\pi^4\sum_{\substack{l_i m_i\\ i=3,4,5,6}}(-i)^{l_3+l_4}(i)^{l_5+l_6}\int dr r^2 j_{l_3}(k_3 r)j_{l_4}(k_4 r)j_{l_5}(k_5 r)j_{l_6}(k_6 r)\\ \times\int d\Omega(\hat{\boldsymbol{n}})Y^*_{l_3 m_3}(\hat{\boldsymbol{n}})Y^*_{l_4 m_4}(\hat{\boldsymbol{n}})Y_{l_5 m_5}(\hat{\boldsymbol{n}})Y_{l_6 m_6}(\hat{\boldsymbol{n}})Y^*_{l_5 m_5}(\hat{\boldsymbol{k}}_5)Y^*_{l_6 m_6}(\hat{\boldsymbol{k}}_6)\\ \times P_\zeta(k_3)Y_{l_3 m_3}(\hat{\boldsymbol{k}}_3)Y_{l_4 m_4}(\hat{\boldsymbol{k}}_4)\,,\end{aligned} \tag{6.17}$$

here, we have used the definition of the delta function in terms of exponentials (A.4) and then expanded these terms using equation (3.8). Subsequently, by plugging the previous terms into equation (6.14), we obtain

$$
\begin{aligned}
&= g_{NL}\, 1024\pi^2 \sum_{\substack{l_i m_i \\ i=1,2,3,4}} (-i)^{l_1+l_2+l_3+l_4}(-1)^{m_1+m_2}\delta_{l_1 l_5}\delta_{-m_1 m_5}\delta_{l_2 l_6}\delta_{-m_2 m_6}\int dk_5 dk_6 \times \\
&(k_5 k_6)^2\, g(k_4) w(k_5) w(k_6) P_\zeta(k_1) P_\zeta(k_2) P_\zeta(k_3) Y_{l_1 m_1}(\hat{\boldsymbol{k}}_1) Y_{l_2 m_2}(\hat{\boldsymbol{k}}_2) Y_{l_3 m_3}(\hat{\boldsymbol{k}}_3) Y_{l_4 m_4}(\hat{\boldsymbol{k}}_4) \\
&\int dr r^2 j_{l_1}(k_1 r) j_{l_5}(k_5 r) \int dr r^2 j_{l_2}(k_2 r) j_{l_6}(k_6 r) \int dr r^2 j_{l_3}(k_3 r) j_{l_4}(k_4 r) j_{l_5}(k_5 r) j_{l_6}(k_6 r) \\
&\int d\Omega(\hat{\boldsymbol{n}}) Y^*_{l_3 m_3}(\hat{\boldsymbol{n}}) Y^*_{l_4 m_4}(\hat{\boldsymbol{n}}) Y_{l_5 m_5}(\hat{\boldsymbol{n}}) Y_{l_6 m_6}(\hat{\boldsymbol{n}}) + perm.\,,
\end{aligned}
\tag{6.18}
$$

by exploiting the property of the Bessel function as shown in equation (3.34), we further simplify the above expression to obtain that

$$
\begin{aligned}
\langle \zeta_G(\boldsymbol{k_1})\zeta_G(\boldsymbol{k_2})\zeta_G(\boldsymbol{k_3})\zeta_{NG}(\boldsymbol{k_4})\rangle_c &= g_{NL} 256\pi^4 \sum_{\substack{l_i m_i \\ i=1,2,3,4}} (-i)^{\sum l_i} g(k_4) w(k_1) w(k_2) P_\zeta(k_1) \\
&\times P_\zeta(k_2) P_\zeta(k_3) \int dr r^2 j_{l_3}(k_3 r) j_{l_4}(k_4 r) j_{l_2}(k_2 r) j_{l_1}(k_1 r) Y_{l_1 m_1}(\hat{\boldsymbol{k}}_1) Y_{l_2 m_2}(\hat{\boldsymbol{k}}_2) \\
&\times Y_{l_3 m_3}(\hat{\boldsymbol{k}}_3) Y_{l_4 m_4}(\hat{\boldsymbol{k}}_4) \int d\Omega(\hat{\boldsymbol{n}}) Y^*_{l_3 m_3}(\hat{\boldsymbol{n}}) Y^*_{l_4 m_4}(\hat{\boldsymbol{n}}) Y^*_{l_1 m_1}(\hat{\boldsymbol{n}}) Y^*_{l_2 m_2}(\hat{\boldsymbol{n}}) + perm\,.
\end{aligned}
\tag{6.19}
$$

It is important to realise that from equation (6.19), it is possible to recover our previous result in equation (6.6), where

$$
\begin{aligned}
\delta^3(\boldsymbol{k_1}+\boldsymbol{k_2}+\boldsymbol{k_3}+\boldsymbol{k_4}) &= 256\pi^4 \sum_{\substack{l_i m_i \\ i=1,2,3,4}} (-i)^{\sum l_i} \int dr r^2 j_{l_3}(k_3 r) j_{l_4}(k_4 r) j_{l_2}(k_2 r) j_{l_1}(k_1 r) \\
& Y_{l_1 m_1}(\hat{\boldsymbol{k}}_1) Y_{l_2 m_2}(\hat{\boldsymbol{k}}_2) Y_{l_3 m_3}(\hat{\boldsymbol{k}}_3) Y_{l_4 m_4}(\hat{\boldsymbol{k}}_4) \int d\Omega(\hat{\boldsymbol{n}}) Y^*_{l_3 m_3}(\hat{\boldsymbol{n}}) Y^*_{l_4 m_4}(\hat{\boldsymbol{n}}) Y^*_{l_1 m_1}(\hat{\boldsymbol{n}}) Y^*_{l_2 m_2}(\hat{\boldsymbol{n}})\,.
\end{aligned}
\tag{6.20}
$$

6.1.2 Shape of the ζ trispectrum

The general expression of the primordial trispectrum T_ζ is given by equation (6.12), where the filters are defined by the step functions depicted in figure 5.2. The power spectrum $P(k)$ can be expressed in terms of the dimensionless power spectrum $\mathcal{P}(k)$, as given in equation (2.37). In this context, $\mathcal{P}(k)$ is defined as presented in equation (2.40). In order to simplify the analysis, we consider only the first term in equation (6.12). After taking into consideration the previous assumptions, we can write this specific contribution to the trispectrum as follows

$$\begin{aligned} T_\zeta(k_1,k_2,k_3,k_4) &= 16\pi^6\, g_{NL}\, g(k_4)\, w(k_1)\, w(k_2)\, \frac{\mathcal{P}_\zeta(k_1)\,\mathcal{P}_\zeta(k_2)\,\mathcal{P}_\zeta(k_3)}{(k_1\,k_2\,k_3)^3} \\ &= 16\pi^6\, g_{NL}\, g(k_4)\, w(k_1)\, w(k_2)\, \frac{\mathcal{P}^3_\zeta(k_0)}{(k_1\,k_2\,k_3)^3}\left(\frac{k_1\,k_2\,k_3}{k_0^3}\right)^{n_s-1} . \end{aligned} \tag{6.21}$$

The aim of this section is to study the shape of the primordial trispectrum of ζ associated with the toy model. The shape is of particular importance because it is a way to identify in which configuration the trispectrum peaks and the arrangement follows for the k modes in order to form a closed tetrahedron. The correct characterization of this property can provide insight into the physical mechanism that gives rise to a specific form of non-Gaussianity, helping to identify the initial conditions of the early Universe.

To properly characterize the shape followed by our primordial trispectrum, we make use of the conditions presented in section 2.5.2, as outlined in the work developed by Chen et al. (2009) about the shape of trispectrum. Here, we explore the folded limit and the specialized planar limit. Given that one of the conditions found for the filters established that $k_4 \gg k_1, k_2$, we have decided not to study the equilateral limit because it does not apply to our case.

In order to plot equation (6.21) is convenient to multiply by $\prod_{i=1}^4 k_i^3$, which is a standard technique used to analyze the shape of the bispectrum. This leads to the following function

$$T_\zeta(k_1,k_2,k_3,k_4) = 16\pi^6\, g_{NL}\, g(k_4)\, w(k_1)\, w(k_2)\, k_4^3\, \mathcal{P}^3_\zeta(k_0)\left(\frac{k_1\,k_2\,k_3}{k_0^3}\right)^{n_s-1} . \tag{6.22}$$

Note that to plot the above expression, we only take into account the functions in terms of k, e.g. the filters and the dependence on the different k modes. Moreover, we assume the values of $n_s = 0.96$ and $k_0 = 0.05\text{Mpc}^{-1}$. However, the parameters g_{NL} and $\mathcal{P}^3_\zeta(k_0)$ are not included it.

6.1.2.1 Folded limit

In the folded limit, we assume that $k_1 = k_2$, $k_3 = k_4$ and the diagonal k_{12} goes to zero. In this part, we plan to explore the shape of one of the contributions to the trispectrum. We have two cases: when we consider the filters and constant filters.

In these cases, the equations become

$$T_\zeta^{loc_1}(k_1,k_4) = 48\pi^6\, k_4^3 \left(\frac{k_1^2\, k_4}{k_0^3}\right)^{n_s-1} ,$$

$$T_\zeta^{loc_2}(k_1,k_4) = 16\pi^6\, g(k_4)\, w(k_1)\, w(k_1)\, k_4^3 \left(\frac{k_1^2\, k_4}{k_0^3}\right)^{n_s-1} . \tag{6.23}$$

Case 1:

Firstly, we plot $T_\zeta^{loc_1}$ equation (6.23) considering constant filters $g = w = 1$, and we used the following values: $k_4 = 1$ and k_1 in the range of $(0, 1)$, in contrast to the condition in section 2.5.2 where $k_1 > k_4$. The diagonal k_{14} can take values between 0 and 2. Notice that figure 6.1 has the same shape as presented in figure 2.5, however, in our case, $T_\zeta^{loc_1}$ has a greater value. We can then conclude that without the filter contributions, the shape of our trispectrum resembles the result of Chen et al. (2009).

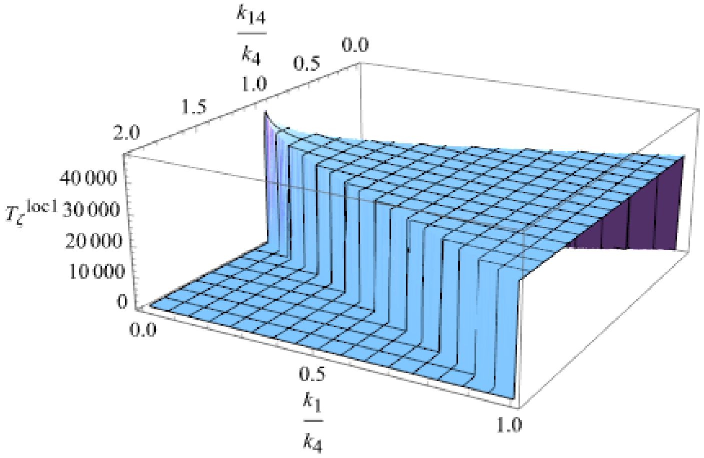

Figure 6.1: Shape function $T_\zeta^{loc_1}$ in the folded limit, where $k_1 = k_2$ and $k_3 = k_4$, with constant filters $g = w = 1$.

The full expression considering all the permutations for $T_\zeta^{loc_1}$ can be expressed as follows (see figure 6.2)

$$T_\zeta^{loc_1}(k_1,k_4) = 48\pi^6 \left[2k_4^3 \left(\frac{k_1^2\, k_4}{k_0^3}\right)^{n_s-1} + 2k_1^3 \left(\frac{k_4^2\, k_1}{k_0^3}\right)^{n_s-1}\right] . \tag{6.24}$$

Case 2:

The subsequent step is to plot $T_\zeta^{loc_2}$ to assess the filters' impact on the trispectrum's shape. In this case, we limit the range of the k variables to the one presented in figure 5.2. Particularly, we assume that $k_4 = 0.1$ and k_1 takes values in the range of $(0,\ 0.002)$. We decided to consider all the contributions to get a better idea of the

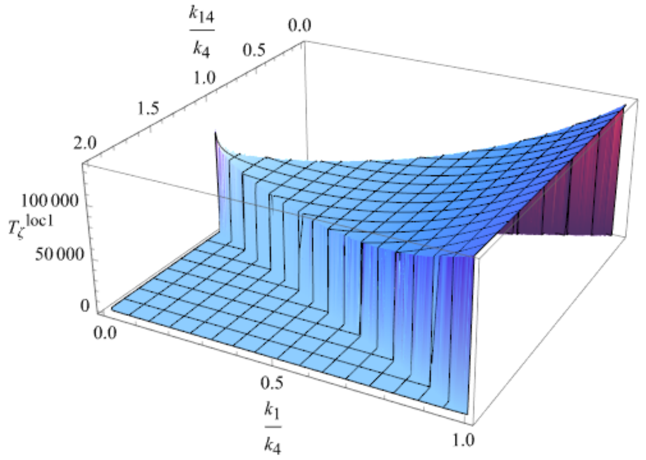

Figure 6.2: Shape function $T_\zeta^{loc_1}$ in the folded limit taking into account all the contributions, equation (6.24) (where $k_1 = k_2$ and $k_3 = k_4$) with the filters $g = w = 1$. The shape resembles the one of a local model similar to Chen et al. (2009).

shape in this particular case. Consequently, equation (6.12) is modified to include the additional terms. Thus, we obtain the following for the first contribution

$$T_\zeta^{loc_2}(k_1, k_4) = 16\pi^6\, g(k_4)\, k_4^3 \left(\frac{k_1^2\, k_4}{k_0^3}\right)^{n_s-1} \Big(w(k_1)\, w(k_2) + w(k_1)\, w(k_3) + w(k_2)\, w(k_3)\Big)\,. \tag{6.25}$$

On the other hand, the full expression of the primordial trispectrum in the folded limit under this specific condition can be defined as

$$\begin{aligned} T_\zeta^{loc_2}(k_1, k_4) = 16\pi^6 \Big[& 2g(k_4)\, k_4^3 \left(\frac{k_1^2\, k_4}{k_0^3}\right)^{n_s-1} \Big(w(k_1)\, w(k_1) + 2w(k_1)\, w(k_4)\Big) \\ & + 2g(k_1)\, k_1^3 \left(\frac{k_1\, k_4^2}{k_0^3}\right)^{n_s-1} \Big(w(k_4)\, w(k_4) + 2w(k_1)\, w(k_4)\Big)\Big]\,. \end{aligned} \tag{6.26}$$

From figure 6.3, it is immediately noticeable that the shape of the trispectrum is significantly affected by the presence of the filters, considerably restricting the range over which the function T_ζ is non-zero. Another important feature is that the shape resembles the structure of the filter w, which introduces a significant scale dependence. Moreover, it is interesting to note that the diagonal k_{14} in both cases needs to have approximately the same value as k_4 for the configuration to satisfy the conditions to form a closed quadrilateral. Additionally, it is possible to evidentiate that the trispectrum peaks when $k_4 > k_1$.

Figures 6.2 and 6.3 reveal how different the shape of the g_{NL} local model is compared to the model with scale dependence. In particular, we can observe the strong effect of the filters, where we can infer that under these initial conditions, the structure of

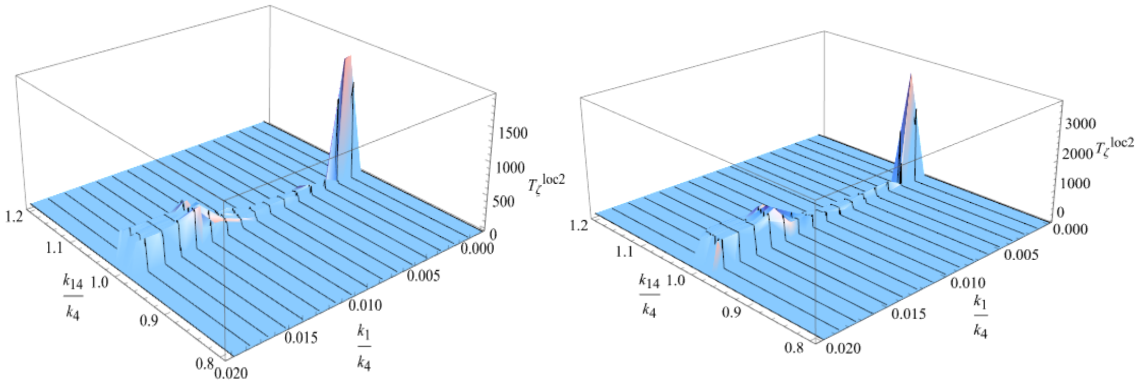

Figure 6.3: Shape function $T_\zeta^{loc_2}$ in the folded limit, where $k_1 = k_2$ and $k_3 = k_4$. On the left, we present the shape of a single contribution, as given by equation (6.25). On the right, we plot the shape accounting for all the permutations, according to equation (6.26).

the filter g becomes less significant in the overall shape function, and the shape is predominantly determined by filter w. This effect arises from the way we propose our initial conditions.

In contrast, when k_1 is set to a value between (0, 0.002) and we examine the range of k_4 between (0, 0.1), we cannot distinguish any particular shape associated with the filters, and the values of $T_\zeta^{loc_2}$ is lower than in the previous case, as depicted in figure 6.4. Additional cases can be explored to gain more insights into the possible shapes in the folded limit. For instance, consider the range of k_1 and k_4 as either (0, 0.002) or (0, 0.1). However, the results are not satisfactory and we cannot extract any shape from the plots. Given the previous cases, we find that the most informative scenario arises when $k_4 > k_1$, with $k_4 = 0.1$ and k_1 varying within the range of (0, 0.002). The value of k_4 does not necessarily have to be set to 0.1, it can be any value within the range of (0, 0.1).

Possible interpretation:

The shape of the configuration is a tool to study the features of non-Gaussianity and potentially probe new particles that decay into the primordial fluctuations. In particular, the physics behind the folded limit (or collapsed limit) considers that it is possible to correlate two collections of modes generated late in inflation mediated by a pair produced at early times, with long wavelength (Kalaja et al. 2021). In other to probe such a process, it is standard to consider a collapsing quadrilateral by making a diagonal very small. More generally, the momenta k can be bundled in two groups, as shown in figure 6.7 all the momenta on each bundle have similar magnitude, although the right and left momenta can be different. Additionally,

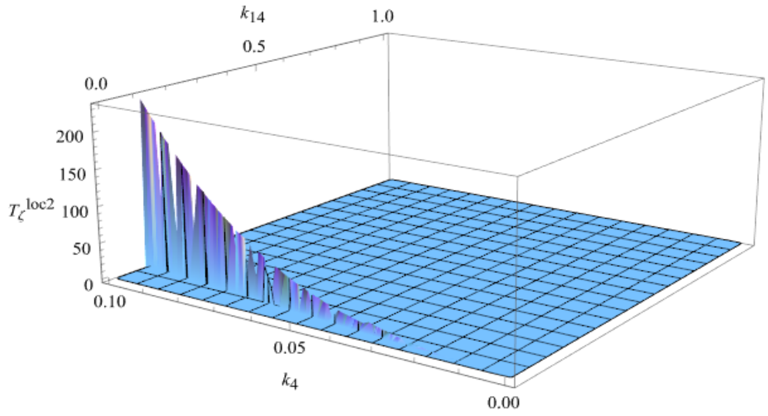

Figure 6.4: Shape function $T_\zeta^{loc_2}$ in the folded limit, where the value of $k_1 = 0.008$ and k_4 varies in a range of (0, 0.1).

in the figure, left and right momenta are produced at similar times, however, the correlation is mediated by σ which is generated earlier.

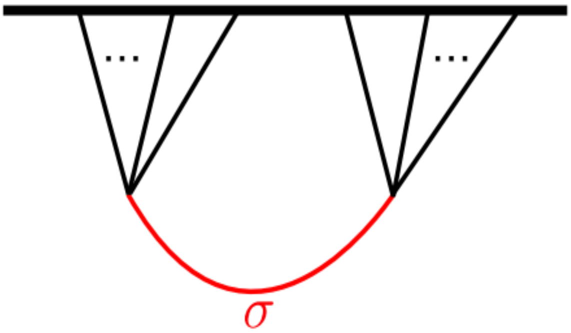

Figure 6.5: Cartoon of a folded N-point function configuration. Time grows along the vertical direction and the horizontal line presents the end of inflation. The momenta on each bundle have similar magnitude, but the left and right momenta can be different. It assumes that left and right momenta are sourced at similar times, but the correlation is mediated by σ which is generated earlier. Adopted from Kalaja et al. (2021).

In our case, conducting an analysis like the one illustrated in figure 6.7 requires a different parametrization of the shape function. This parametrization should allow us to incorporate the effect of the mass of the particle mediating the interaction and necessitates a more detailed numerical implementation. For additional information, refer to Kalaja et al. (2021) and the references therein. This specific approach to analyzing the physics behind the shape of the trispectrum serves as an example that underscores the fundamental role of shape analysis in comprehending the interactions that can occur in the early Universe, ultimately leading to specific configurations.

On the other hand, even though our exploration of the shape only considers some cases, we can still extract insights useful for further in-depth studies. We find that the configuration studied can be associated with the case of a folded kite (see, figure 6.6), where $k_{12} \ll k_1 \sim k_2, k_3 \sim k_4$. In fact, the diagonal k_{12} for our case goes to zero, so we should expect that $k_{14} \sim k_4$, as evident from figure 6.2. While we cannot strictly claim that this is the only valid configuration associated with the shape of our trispectrum, it is the one that provides the most reasonable result for now following the approach based on the work of Chen et al. (2009).

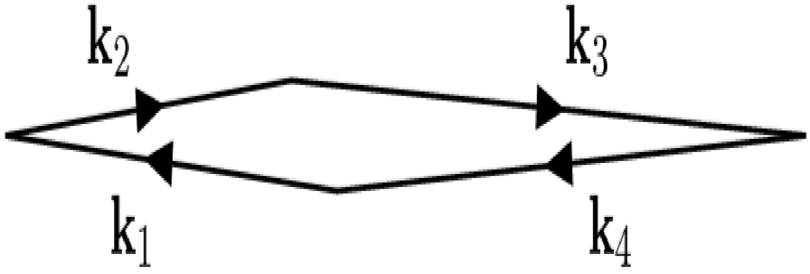

Figure 6.6: Representation of the folded kite shape of the trispectrum where $k_{12} \ll k_1 \sim k_2, k_3 \sim k_4$. Adopted from Bellomo et al. (2018).

6.1.2.2 Specialized planar limit

It is characterized by the relation $k_1 = k_3 = k_{14}$ and a specific form for the diagonal k_{12}, as given by equation (2.56). In this case, the equations take the following form

Case 1:

$$T_\zeta^{loc_1}(k_1, k_2, k_4) = 48\pi^6 \Big[2k_1^3 \left(\frac{k_1 k_2 k_4}{k_0^3} \right)^{n_s - 1} + k_2^3 \left(\frac{k_1^2 k_4}{k_0^3} \right)^{n_s - 1} + k_4^3 \left(\frac{k_1^2 k_2}{k_0^3} \right)^{n_s - 1} \Big] . \tag{6.27}$$

In this case, we have plotted the equation (6.27) taking the filters as constant. Similar to the folded limit case, we find that we recover the shape of a local model. Additionally, we can observe that the shape is very similar to the one presented in section 2.5.2. When we compare the graphs obtained for the local case in both limits figures 6.2 and 6.7, we notice that the amplitude of the shape function is larger in the folded limit.

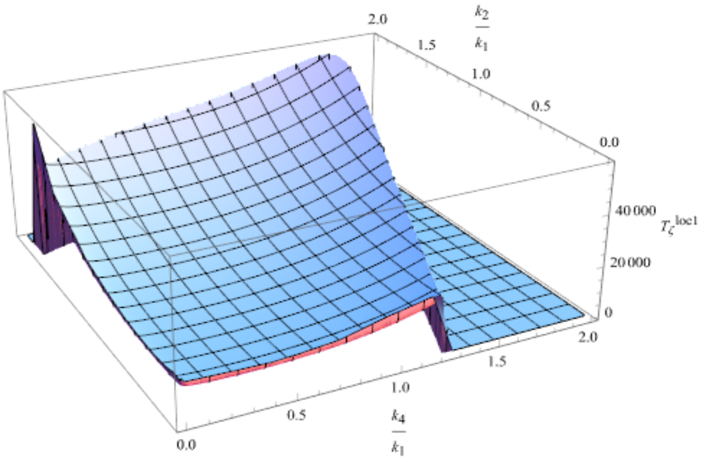

Figure 6.7: Shape function $T_\zeta^{loc_1}$ in the specialized planar limit ($k_1 = k_3 = k_{14}$) with constant filters. We recover the local shape obtained by Chen et al. (2009).

Case 2: When considering the shape function that incorporates the contributions of the filters equation (6.28), it becomes challenging to identify a specific shape. This complexity may arise from the limited number of configurations that meet the conditions for forming a closed quadrilateral. Consequently, these configurations may not adequately represent the general behavior of the trispectrum's shape

$$\begin{aligned} T_\zeta^{loc_2}(k_1, k_2, k_4) = 16\pi^6 \Big[& 2g(k_1)\, k_1^3 \left(\frac{k_1\, k_2\, k_4}{k_0^3} \right)^{n_s - 1} \Big(w(k_1)\, w(k_2) + w(k_2)\, w(k_4) \\ & + w(k_1)\, w(k_4) \Big) + g(k_2)\, k_2^3 \left(\frac{k_1^2\, k_4}{k_0^3} \right)^{n_s - 1} \Big(w(k_1)\, w(k_1) + 2w(k_1)\, w(k_4) \Big) + \\ & g(k_4)\, k_4^3 \left(\frac{k_1^2\, k_2}{k_0^3} \right)^{n_s - 1} \Big(w(k_1)\, w(k_1) + 2w(k_1)\, w(k_2) \Big) \Big] . \end{aligned} \tag{6.28}$$

Investigating the shape of our trispectrum in this limit, we considered various cases, some of which are illustrated in figures 6.8 and 6.9. In this approach, we opted to fix the value of one k, while the other two are treated as free parameters within specific ranges. In the first plot, we assume initial conditions where k_1 takes on a particular value from the range (0, 0.1), while k_2 and k_4 vary within the ranges (0, 0.002) and (0, 0.1), respectively. However, it becomes evident from the figure that distinguishing a specific shape is challenging. The plot presents a predominant peak along with some additional features, but extracting meaningful information from this configuration proves to be complicated.

In figure 6.9, the value of k_1 is fixed within the range (0, 0.002) while allowing k_4 and k_2 to vary, similar to the previous case (graph on the left). On the right plot,

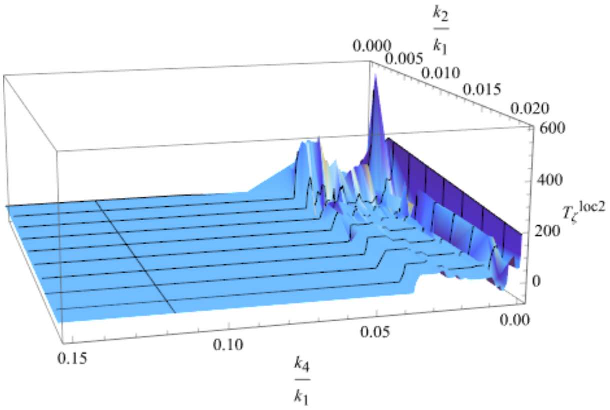

Figure 6.8: Shape function $T_\zeta^{loc_2}$ in the specialized planar limit, with $k_1 = k_3 = k_{14} = 0.05$, and k_2, k_4 varying in the ranges (0, 0.002) and (0, 0.1), respectively.

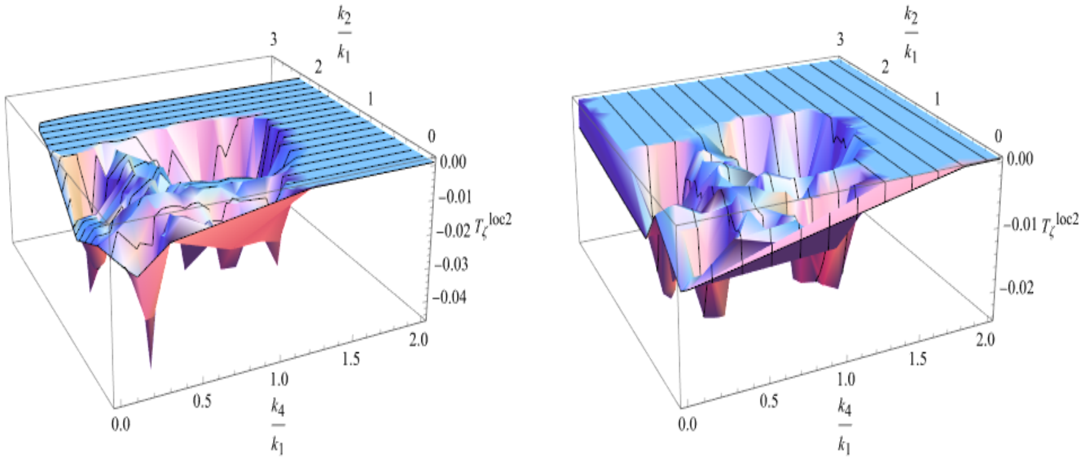

Figure 6.9: Shape function $T_\zeta^{loc_2}$ in the specialized planar limit, where $k_1 = k_3 = k_{14}$. On the left, we present the shape when $k_1 = 0.0008$ and k_2, k_4 vary within the ranges (0, 0.1) and (0, 0.002), respectively. On the right, we plot the shape interchanging the ranges of k_2 and k_4.

we interchanged the ranges of k_4 and k_2, setting them to (0, 0.002) and (0, 0.1), respectively. Once again, the shape of $T_\zeta^{loc_2}$ appears complex in both cases, exhibiting negative values. These negative values might suggest that, in these scenarios, the filter g has more relevance. The presence of multiple peaks indicates that specific configurations satisfy the conditions and yield a non-zero $T_\zeta^{loc_2}$. However, the parameter space is confined to cases where $k_1 \geq k_4, k_2$, which may suggest that most relevant contributions come from $\langle \zeta_1^{NG}\, \zeta_2^{G}\, \zeta_3^{G}\, \zeta_4^{G} \rangle_c$ and $\langle \zeta_1^{G}\, \zeta_2^{G}\, \zeta_3^{NG}\, \zeta_4^{G} \rangle_c$. Nevertheless, a more in-depth analysis of this limit is necessary to comprehend the features exhibited in the plots.

Based on the previous discussion, we conclude that the folded limit appears to be the scenario that best describes our trispectrum. This conclusion is drawn from the fact that the amplitude of $T_\zeta^{loc_2}$ is larger in this case. It is important to note that this is our current assumption based on the results presented in this section, and further investigation may lead to different conclusions if we explore additional shapes and the physical significance of the filters.

6.2 Trispectrum of the CMB temperature

The CMB trispectrum is related to the third-order perturbations in the primordial curvature ζ through the coupling parameter g_{NL}. This parameter is often introduced as a constant, relating to the amplitude of the trispectrum. In the simplest model of inflation, a single-field slow-roll model infers that the amplitude and scale-dependence of the higher-order correlation functions are of the order of the slow-roll parameters, meaning they are too small to observe at present time. However, several inflationary scenarios allow for a scale-dependent trispectrum, in which the non-linearity parameters are no longer constants, but depend on a k mode in Fourier space, as is the case with the trispectrum that we will explore in this section.

Similarly to Okamoto and Hu (2002), the leading order contributions to the CMB trispectrum under the assumption of the toy model are

$$\begin{aligned} T = {} & \langle a^{NG}_{l_1m_1} a^{G}_{l_2m_2} a^{G}_{l_3m_3} a^{G}_{l_4m_4}\rangle_c + \langle a^{G}_{l_1m_1} a^{NG}_{l_2m_2} a^{G}_{l_3m_3} a^{G}_{l_4m_4}\rangle_c + \\ & \langle a^{G}_{l_1m_1} a^{G}_{l_2m_2} a^{NG}_{l_3m_3} a^{G}_{l_4m_4}\rangle_c + \langle a^{G}_{l_1m_1} a^{G}_{l_2m_2} a^{G}_{l_3m_3} a^{NG}_{l_4m_4}\rangle_c \,. \end{aligned} \tag{6.29}$$

In our case, the Gaussian and non-Gaussian contribution of the a_{lm} coefficients are given by equations (5.21) and (5.22), respectively. As a result, we obtain for the $\langle a^{G}_{l_1m_1} a^{G}_{l_2m_2} a^{G}_{l_3m_3} a^{NG}_{l_4m_4}\rangle$ contribution that

$$\begin{aligned} \langle a^{G}_{l_1m_1} a^{G}_{l_2m_2} a^{G}_{l_3m_3} a^{NG}_{l_4m_4}\rangle_c = g_{NL} \left(\frac{12\pi}{5}\right)^4 \prod_{j=1}^{4} i^{\sum l_j} \int \frac{d^3\boldsymbol{k_j}}{(2\pi)^3} \Delta_{l_1}(k_1)\, \Delta_{l_2}(k_2)\, \Delta_{l_3}(k_3) \\ \times \Delta_{l_4}(k_4)\, Y^*_{l_1m_1}(\boldsymbol{\hat{k}_1}) Y^*_{l_2m_2}(\boldsymbol{\hat{k}_2}) Y^*_{l_3m_3}(\boldsymbol{\hat{k}_3}) Y^*_{l_4m_4}(\boldsymbol{\hat{k}_4}) \\ \times \langle \zeta_G(\boldsymbol{k}_1)\, \zeta_G(\boldsymbol{k}_2)\, \zeta_G(\boldsymbol{k}_3)\, \zeta_{NG}(\boldsymbol{k}_4)\rangle_c \,. \end{aligned} \tag{6.30}$$

Then, one of the connected contributions to this specific term is

$$\begin{aligned}\langle a^{G}_{l_1m_1}a^{G}_{l_2m_2}a^{G}_{l_3m_3}a^{NG}_{l_4m_4}\rangle_c = g_{NL}\left(\frac{12\pi}{5}\right)^4 \prod_{j=1}^{4} i^{\sum l_j}\int \frac{d^3\boldsymbol{k_j}}{(2\pi)^3}\Delta_{l_1}(k_1)\,\Delta_{l_2}(k_2)\\ \times\Delta_{l_3}(k_3)\,\Delta_{l_4}(k_4)\,Y^*_{l_1m_1}(\boldsymbol{\hat{k}_1})Y^*_{l_2m_2}(\boldsymbol{\hat{k}_2})Y^*_{l_3m_3}(\boldsymbol{\hat{k}_3})Y^*_{l_4m_4}(\boldsymbol{\hat{k}_4})\\ \times\langle\zeta_G(\boldsymbol{k}_1)\,\zeta_G(\boldsymbol{k}_5)\rangle\langle\zeta_G(\boldsymbol{k}_3)\,\zeta_G(\boldsymbol{\tilde{k}}_{56})\rangle\langle\zeta_G(\boldsymbol{k}_2)\,\zeta_G(\boldsymbol{k}_6)\rangle + perm.\,,\end{aligned} \tag{6.31}$$

by substituting equation (6.19) into equation (6.31) the expression becomes

$$\begin{aligned}\langle a^{G}_{l_1m_1}a^{G}_{l_2m_2}a^{G}_{l_3m_3}a^{NG}_{l_4m_4}\rangle_c = g_{NL}\,\frac{1296}{625\pi^4}\int dk_1\,dk_2\,dk_3\,dk_4(k_1\,k_2\,k_3\,k_4)^2\times\\ \Delta_{l_1}(k_1)\,\Delta_{l_2}(k_2)\Delta_{l_3}(k_3)\,\Delta_{l_4}(k_4)\,g(k_4)\,w(k_1)\,w(k_2)\,P_\zeta(k_1)\,P_\zeta(k_2)\,P_\zeta(k_3)\times\\ \int drr^2 j_{l_3}(k_3r)j_{l_4}(k_4r)j_{l_1}(k_1r)j_{l_2}(k_2r)\times\\ \int d\Omega(\boldsymbol{\hat{n}})Y^*_{l_3m_3}(\boldsymbol{\hat{n}})Y^*_{l_4m_4}(\boldsymbol{\hat{n}})Y^*_{l_1m_1}(\boldsymbol{\hat{n}})Y^*_{l_2m_2}(\boldsymbol{\hat{n}}) + perm\,.\end{aligned} \tag{6.32}$$

In order to further simplify the above expression, we can follow the approach outlined in section 3.1. We can begin by defining the trispectrum as

$$T_{l_1m_1l_2m_2l_3m_3l_4m_4} = \int d\Omega(\boldsymbol{\hat{n}})Y^*_{l_1m_1}(\boldsymbol{\hat{n}})Y^*_{l_2m_2}(\boldsymbol{\hat{n}})Y^*_{l_3m_3}(\boldsymbol{\hat{n}})Y^*_{l_4m_4}(\boldsymbol{\hat{n}})\,t^{l_1l_2}_{l_3l_4}\,, \tag{6.33}$$

where the reduced trispectrum is given by

$$\begin{aligned}t^{l_1l_2}_{l_3l_4} = g_{NL}\,\frac{1296}{625\pi^4}\int dk_1\,dk_2\,dk_3\,dk_4(k_1\,k_2\,k_3\,k_4)^2\Delta_{l_1}(k_1)\,\Delta_{l_2}(k_2)\Delta_{l_3}(k_3)\,\Delta_{l_4}(k_4)\\ g(k_4)\,w(k_1)\,w(k_2)\,P_\zeta(k_1)\,P_\zeta(k_2)\,P_\zeta(k_3)\int drr^2 j_{l_1}(k_1r)j_{l_2}(k_2r)j_{l_3}(k_3r)j_{l_4}(k_4r) + perm\,.\end{aligned} \tag{6.34}$$

Additionally, we can write equation (6.34) in the following form

$$t^{l_1l_2}_{l_3l_4} = \frac{1296}{625\pi^4}\int drr^2\beta_{l_1}(r)\,\beta_{l_2}(r)\,\alpha_{l_3}(r)\,\mu_{l_4}(r) + perm\,, \tag{6.35}$$

where we have defined that

$$\beta_l(r) = \int dk\,k^2\,w(k)\,P_\zeta(k)\,\Delta_l(k)\,j_l(kr)\,, \tag{6.36}$$

$$\alpha_l(r) = \int dk\,k^2\,P_\zeta(k)\,\Delta_l(k)\,j_l(kr)\,, \tag{6.37}$$

$$\mu_l(r) = \int dk\,k^2\,g_{NL}\,g(k)\,\Delta_l(k)\,j_l(kr)\,. \tag{6.38}$$

It should be noted that the above development only considers one of the contributions within the term $\langle a^G_{l_1m_1}a^G_{l_2m_2}a^G_{l_3m_3}a^{NG}_{l_4m_4}\rangle_c$. We must also account for the other permutations to obtain the complete reduced trispectrum associated with this term. As a result, we obtain that

$$t^{l_1l_2}_{l_3l_4} = \frac{2592}{625\pi^4}\int drr^2\mu_{l_4}(r)\left[\beta_{l_1}(r)\,\beta_{l_2}(r)\alpha_{l_3}(r)+\beta_{l_1}(r)\beta_{l_3}(r)\alpha_{l_2}(r)+\beta_{l_2}(r)\beta_{l_3}(r)\alpha_{l_1}(r)\right]. \tag{6.39}$$

On the other hand, to further simplify the expression provided in equation (6.39), let us assume a constant kernel (constant filters) leading to

$$\tilde{\mathcal{W}} \equiv g(k_4)w(k_1)w(k_2) \equiv g\,w^2\,. \tag{6.40}$$

Additionally, we consider the Sachs-wolfes approximation where the transfer function has a simple form given by $\Delta_l(k) = 1/3\,j_l(kr_*)$, this assumption leads to the following result

$$\mu_l(r) = g_{NL}\frac{g\,\pi}{6\,r_*^2}\,\delta(r-r_*)\,. \tag{6.41}$$

Since the temperature power spectrum has been defined as

$$C_l^{SW} = \frac{2}{9\pi}\int dk\,k^2\,P_\zeta(k)\,j_l^2(kr_*)\,, \tag{6.42}$$

we can express then $\beta_l(r_*) = \frac{3\pi}{2}wC_l^{SW}$ and $\alpha_l(r_*) = \frac{3\pi}{2}C_l^{SW}$. The reduced trispectrum for this term is therefore given by

$$t^{l_1l_2}_{l_3l_4} = \frac{4374}{625}\,g\,w^2\,g_{NL}C^{SW}_{l_1}C^{SW}_{l_2}C^{SW}_{l_3}\,. \tag{6.43}$$

So far, we have discussed how to calculate one component of the trispectrum and derived a simplified expression for this case when we assume the Sachs-Wolfe approximation and that the filters are constants, resulting in equation (6.43), where we observe that it is the product of three angular power spectra. It is worth noting that the calculation of the additional terms of the trispectrum (T) follows the same procedure as above. Thus, the complete expression for the total trispectrum of the CMB is given by

$$
\begin{aligned}
t^{l_1 l_2}_{l_3 l_4} = \frac{2592}{625\pi^4} \int dr r^2 \Big[& \mu_{l_1}(r) \Big(\beta_{l_2}(r)\beta_{l_3}(r)\alpha_{l_4}(r) + \beta_{l_2}(r)\beta_{l_4}(r)\alpha_{l_3}(r) \\
& + \beta_{l_3}(r)\beta_{l_4}(r)\alpha_{l_2}(r) \Big) + \mu_{l_2}(r) \Big(\beta_{l_1}(r)\beta_{l_3}(r)\alpha_{l_4}(r) + \beta_{l_1}(r)\beta_{l_4}(r)\alpha_{l_3}(r) \\
& + \beta_{l_3}(r)\beta_{l_4}(r)\alpha_{l_1}(r) \Big) + \mu_{l_3}(r) \Big(\beta_{l_1}(r)\beta_{l_2}(r)\alpha_{l_4}(r) + \beta_{l_1}(r)\beta_{l_4}(r)\alpha_{l_2}(r) \\
& + \beta_{l_2}(r)\beta_{l_4}(r)\alpha_{l_1}(r) \Big) + \mu_{l_4}(r) \Big(\beta_{l_1}(r)\, \beta_{l_2}(r)\alpha_{l_3}(r) + \beta_{l_1}(r)\beta_{l_3}(r)\alpha_{l_2}(r) \\
& + \beta_{l_2}(r)\beta_{l_3}(r)\alpha_{l_1}(r) \Big) \Big] \, . \qquad (6.44)
\end{aligned}
$$

Equations (6.33), (6.36), (6.37), (6.38) and (6.44) must be evaluated numerically to better elucidate the type of trispectrum we are dealing with. For this purpose, codes such as CMBFAST or CAMB can be employed to compute the full radiation transfer $\Delta_l(k)$ and perform the integration over k. However, this analysis is out of the scope of the results presented in this thesis and is proposed as a possible continuation of this work.

Considering the challenge of understanding equation (6.33) without numerical implementation, let us return to the simple case where the filters are constant and are in the Sachs-Wolfe approximation. As a result, equation (6.44) is simplified to

$$
\begin{aligned}
t^{l_1 l_2}_{l_3 l_4} = \frac{4374}{625}\, g\, w^2\, g_{NL} \Big[& C^{SW}_{l_2} C^{SW}_{l_3} C^{SW}_{l_4} + C^{SW}_{l_1} C^{SW}_{l_3} C^{SW}_{l_4} \\
& + C^{SW}_{l_1} C^{SW}_{l_2} C^{SW}_{l_4} + C^{SW}_{l_1} C^{SW}_{l_2} C^{SW}_{l_3} \Big] \, . \qquad (6.45)
\end{aligned}
$$

In the previous case, equation (6.45) contains the contribution of the angular power spectrum C^{SW}_l in the Sachs-Wolfe approximation. Implementing equations (6.33) and (6.45) numerically is necessary to obtain the CMB trispectrum in the Sachs-Wolfe case.

In this section, we have presented the methodology for calculating the trispectrum associated with the toy model. The most relevant equations are (6.33) and (6.44), where we notice the influence of the filters in all expressions. Another interesting case arises when we consider the filters as constants and obtain the expressions under the Sachs-Wolfe approximation (equation (6.45)). It is evident that the implementation of these equations is the next step in comprehending the model we are proposing, where non-Gaussianity is the foundation. From this trispectrum template that we are proposing, we could potentially analyze and explore this non-Gaussianity further.

6.3 Future prospects

Further extensions of this work can take various approaches, each tailored to the specific information we aim to extract from the equations. Some potential points for future exploration include:

- Simulations of the coefficients a_{lm} using the equations expressed in terms of the curvature perturbation ζ in real space, as described in equation (5.26), can be a valuable approach to understanding the effects of the non-Gaussian model and its ability to accurately reproduce the observed CMB map.

- Investigating the physical mechanism behind the convolution kernel proposed to construct the definition of the curvature perturbation is an important step in understanding the underlying inflationary model that gives rise to the characteristic of the toy model developed by Hansen et al. (2019). Further explorations of the shape of the trispectum could be the key to gaining information about the kernel in our model, see e.g. Kalaja et al. (2021).

- A numerical solution of the set of equations (6.33), (6.36), (6.37), (6.38) and (6.44) is essential to assess the properties of the toy model's trispectrum. Additionally, conducting a Fisher forecasting analysis of our trispectrum template would be a valuable endeavor when working with Planck data. This analysis aims to obtain constraints on non-Gaussianity through the g_{NL} parameter, as demonstrated in previous studies Kogo and Komatsu (2006), Regan et al. (2015), Akrami et al. (2020a).

The potential of these analyses is immense and demands advanced numerical techniques and further considerations beyond what we have developed in this thesis. Therefore, there is still much to uncover about the CMB anomalies and their possible connection to the initial conditions of the early Universe. This work can be considered as an initial exploration that can be refined to gain deeper insights into the physical mechanism responsible for the presence of these anomalies in the CMB maps.

Chapter 7

Discussion and Conclusions

In this thesis, we have addressed the issue of the CMB anomalies which are statistical deviations observed when comparing observational data with our standard model, ΛCDM (see, e.g. Schwarz et al. 2015). The primary aim of this work was to investigate the characteristics of a possible physical model capable of generating these anomalous features. To achieve this, we explored the properties of a phenomenological model proposed by Hansen et al. (2019).

The CMB anomalies have been extensively explored since their discovery in the data. However, we still do not have a satisfactory explanation for their presence in the CMB. A brief review of some of the anomalies can be found in Chapter 4. The literature on this topic contains numerous models and studies, with common explanations falling into two categories: those that consider the breaking of isotropy as a possible explanation and those that attribute the anomalies to the presence of non-Gaussianity in the primordial perturbations. For instance, the modeling of the hemispherical power asymmetry is often treated as a result of a dipolar modulation of the temperature. Additionally, local non-Gaussian models, which can arise from certain inflationary models such as the Curvaton inflation, have been proposed as possible cosmological mechanisms to explain the anomalies in the CMB radiation. However, some difficulties are encountered in these explanations.

Given the complexity of studying all the anomalies together, it has been standard practice to focus on one, or at most, two of them. An intriguing proposal by Hansen et al. (2019) successfully reproduces six of the CMB anomalies simultaneously. This toy model is based on the construction of a non-Gaussian temperature field which involves the contribution of a cubic order temperature field term. Additionally, the model requires the introduction of an amplitude parameter, β, and some filters, w_l and g_l, which can be tuned to test whether the anomalies can be reproduced, see equation (5.1). Intrigued by the model's properties, Hansen et al. (2019) suggest that this class of toy model resembles models of primordial non-Gaussianity characterized by strongly scale-dependent g_{NL}-like trispectra. Subsequent developments by the same authors aimed to establish a connection between the toy model's temperature field ($T(\hat{\boldsymbol{n}})$) and the inflationary quantity known as the curvature perturbation, denoted by ζ.

We explored this connection between the temperature field and the curvature perturbation in Chapter 5. The methodology involves mimicking the behavior of the non-Gaussian $T(\hat{\boldsymbol{n}})$ in the definition of ζ. To achieve this, we used an integral convolution kernel in Fourier space, where the convolution comprises the product of three perturbations. This ansatz is commonly employed in non-Gaussian models to account for non-linear corrections in the primordial potentials that generate non-Gaussian features. In our case, the non-linear parameter associated with the cubic order contribution is g_{NL}, which measures the strength of non-Gaussianity. The convolution kernel $\tilde{\mathcal{W}}$ is then related to the filters introduced in the temperature field. Furthermore, the presence of these filters imparts a scale dependence to our model.

To establish the relation between the convolution kernel and the filters applied to the toy model, two approaches were used: (1) an expansion of the temperature field $T(\hat{\boldsymbol{n}})$ in spherical harmonics was performed, obtaining equations (5.13) and (5.30) for the multiple coefficients a_{lm} in terms of ζ. Subsequently, we defined another relation for a_{lm} in terms of the convolution definition of ζ, equation (5.31). Comparing these two different expressions of the multiple coefficients we found a relationship between the kernel and the filters, equation (5.33) and (5.44), however, we did not explore these expressions due to their complicated form containing the transfer function $\Delta_l(k)$. (2) Instead, it was found convenient to reconstruct the curvature perturbation by directly applying analogous filters to w and g in Fourier space to the curvature perturbation ζ, see figure 5.2. As a result, we obtained equation (5.51), which is a significant result because it provides a simplified expression for relating the filters to the behavior of the convolution kernel, which can provide insights into the interactions between the perturbations.

The expressions in Chapter 5 serve as the basis for the subsequent analysis required to characterize the non-Gaussian model with strong scale dependence that we are investigating as a potential physical model underlying the toy model's properties. To explore non-Gaussianity, we employ higher-order correlation functions. In particular, since we worked with a cubic order contribution in ζ, our analysis extends to the four-point correlation function or trispectrum in Fourier space. When dealing with the 4-point correlation function, we must distinguish between unconnected terms that contain Gaussian information and the connected terms that encapsulate non-Gaussian statistics. In our analysis, we focus on the connected terms that satisfy equation (6.4).

In Chapter 6, we delve into the computation of the trispectrum associated with the toy model. As discussed in Chapter 3, the statistical properties of the multiple moments a_{lm} are inherited from $\zeta(\boldsymbol{k})$, so that, the CMB trispectrum is directly related to integrals of the 4-point correlation function of $\zeta(\boldsymbol{k})$. Specific trispectrum templates are detailed in section 3.3. Therefore, we initially focus on the primordial trispectrum of ζ. During the calculation, it becomes evident that to obtain the connected contributions, we must consider combinations of the Gaussian perturbations ζ_G with the perturbations contained in the definition of ζ_{NG}, as given by equation (5.16). The resulting primordial trispectrum is presented in equation (6.12), where the significant modification caused by the filters in the expression is noticeable when compared to the local trispectrum with a constant g_{NL}, as shown in equation (2.45) Akrami et al. (2020a). Among the various results, equation (6.12) is one of the most important ones. Additionally, we compute the local trispectrum for our case, as described in equation (6.13), considering the filters as constant in the expression. These two equations allow us to observe the distinction between a local-type model with scale dependence introduced by the filters and a local-type model.

A more quantitative approach to studying the primordial trispectrum, T_ζ, involves analyzing its shape, which provides crucial information about the configurations of the wavevectors k, where the trispectrum peaks or exhibits significant values. This feature is of great significance as it offers insight into the specific physical mechanisms that can generate a particular shape. In section 2.5.2, we illustrated the methodology employed by Chen et al. (2009) to investigate the shape of the trispectrum within a local model parametrized by the four wavevector magnitudes k and two diagonals k_{12} and k_{14}, as depicted in figure 2.3. Chen et al. (2009) explored the local trispectrum in various limits: equilateral ($k_1 = k_2 = k_3 = k_4$), folded limit ($k_1 = k_2, k_3 = k_4, k_{12} = 0$) and specialized planar limit ($k_1 = k_3 = k_{14}$). We have reproduced some of their results in figures 2.4 and 2.5. In this work, we have used a similar methodology to investigate the shape of T_ζ. To facilitate this analysis, we assumed that the power spectrum $P(k)$ can be expressed in terms of the dimensionless power spectrum $\mathcal{P}(k)$, which is often parametrized as a power law involving the amplitude $\mathcal{P}(k_0)$ and the scalar spectral index n_s. We further adopted standard values for these parameters, specifically $k_0 = 0.05\text{Mpc}^{-1}$ and $n_s = 0.96$.

In the folded limit, we conducted two separate analyses: in the first case, we plotted equation (6.24) considering the filters as constant. We ensured that $k_4 > k_1$ and used the same conditions presented in section 2.5.2. Our results showed that the shape of our local trispectrum, as depicted in figure 6.2, resembled the shape presented in Chen et al. (2009). However, it is important to note that the amplitude of T_ζ was larger in our case. In the second case, we plotted the full expression of our trispectrum, as described in equation (6.25). In this case, we set the initial conditions based on the ranges of the filters w and g (figure 5.2). In one scenario, we fixed the value of k_4 in the range of (0, 0.1) and varied k_1 in the range of (0, 0.002), while keeping the diagonal k_{14} as a free parameter, see figure 6.3. In another scenario, we set the value of k_1 between (0, 0.002) and explored k_4 between (0, 0.1), as shown in figure 6.4. We also examined the case where both k_1 and k_4 varied within the same range. However, this last scenario did not provide useful insights into identifying the trispectrum's shape, as it primarily revealed different configurations that satisfy the given conditions. Among all these cases, we identified the first configuration as the most appropriate for describing the shape of the trispectrum.

The plot depicted on the right side in figure 6.3 exhibits some intriguing features: the overall shape of T_ζ^{loc2} resembles the form of filter w, the conditions to form a closed tetrahedron are satisfied when the diagonal k_{14} closely matches the value of k_4. Additionally, the amplitude of the trispectrum is significantly larger in the range where $k_4 > k_1$. It is worth emphasizing the substantial impact of the filters on the shape of the trispectrum, particularly when comparing a g_{NL} local-type non-Gaussian model (figure 6.2) and g_{NL}-like non-Gaussian model with scale dependence introduced by the filters (figure 6.3). Therefore, it is reasonable to associate the presence of the filters as a strong constraint that limits the configurations where our trispectrum is non-zero. Understanding the role of these filters and their significant influence on the trispectrum's shape requires a physical mechanism related to the convolution kernel, which could provide further insights into this specific arrangement.

Furthermore, we also delved into the specialized planar limit described by equations (6.27) and (6.28). In this case, we explored several initial conditions, but we could not identify any specific shapes, similar to the case in figure 6.4. The plots often displayed peaks or a single peak, and the amplitude T_ζ^{loc2} exhibited lower values than in the previous cases. Clearly, when filters are incorporated into the expression of the shape function, the conditions necessary to generate a closed configuration become challenging to satisfy. This significantly constrains the parameter space where our trispectrum is non-zero. However, when we plotted (6.27) applying the same conditions outlined in section 2.5.2, figure 6.7 started to resemble the shape of the specialized limit as presented in Chen et al. (2009). This observation underscores the necessity for a more profound understanding of the filters to gain insights into their effects on the shape.

From all the previous considerations, we assume that the folded limit best describes our trispectrum based on the evidence we have accumulated thus far. This case can be associated with a folded kite shape, as illustrated in figure 6.6. However, this assumption remains subject to confirmation. It is important to note that we have only examined two limits, and the specialized planar limit does not seem suitable for characterizing the trispectrum's shape. On the other hand, an intriguing work conducted by Kalaja et al. (2021) introduced an alternative parametrization of the shape function. This approach considers the mass of the mediator responsible for interactions that could lead to the folded limit (or collapsed limit). Investigating this type of parametrization may provide a deeper understanding of the interactions between perturbations and potentially provide more insight into the role of the filters. It is crucial to acknowledge that there are several aspects of the shape of the primordial trispectrum that we still need to comprehend. Nevertheless, this simplified study has allowed us to identify a potential shape and can open the way for a more in-depth analysis.

After obtaining the expression for the 4-point correlation of ζ, as shown in equation 6.21, we proceeded to compute the temperature trispectrum, as given by equation 6.29. We defined the trispectrum expression, $T_{l_1 m_1 \ldots l_4 m_4}$ similarly to what was discussed in section 3.3, as presented in equation 6.33. In this expression, the reduced trispectrum $t^{l_1 l_2}_{l_3 l_4}$ specific for our model is defined in equation 6.44, and it is expressed in terms of equations (6.36), (6.37) and (6.38). Additionally, we computed another expression under the assumption of constant filters and in the Sach-Wolfes approximation, given by equation (6.45), which contains the contribution of the product of three angular power spectrum, C_l^{SW}, and their permutations. It is important to highlight that these equations require numerical solutions to better elucidate their behavior and the influence of the filters. In the general case, we have to solve the Boltzman-Einstein equations to obtain the radiative transfer function Δ_l, and integration over k which can be done by numerical tools like CAMB and CMBFAST codes. Consequently, our equations serve as a starting point for developing a further numerical analysis of the properties of the template that we have derived, taking into account the properties of the toy model.

Appendix A

Conventions and definitions

Throughout the thesis, we use the following Fourier convention for the case of our computations

$$\tilde{f}(\boldsymbol{k}) = \int d^3\boldsymbol{x}\, e^{-i\boldsymbol{x}\cdot\boldsymbol{k}} f(\boldsymbol{x})\,, \tag{A.1}$$

$$f(\boldsymbol{x}) = \int \frac{d^3\boldsymbol{k}}{(2\pi)^3}\, e^{i\boldsymbol{x}\cdot\boldsymbol{k}} \tilde{f}(\boldsymbol{k})\,, \tag{A.2}$$

$$\delta(\boldsymbol{x}) = \int \frac{d^3\boldsymbol{k}}{(2\pi)^3}\, e^{i\boldsymbol{x}\cdot\boldsymbol{k}}\,, \tag{A.3}$$

$$\delta(\boldsymbol{k}) = \int \frac{d^3\boldsymbol{x}}{(2\pi)^3}\, e^{-i\boldsymbol{x}\cdot\boldsymbol{k}}\,. \tag{A.4}$$

As usual, the temperature fluctuations of the CMB are decomposed into spherical harmonics

$$\frac{\Delta T}{T}(\hat{\boldsymbol{n}}) = \sum_{l=0}^{\infty} \sum_{m=-l}^{l} a_{lm}\, Y_{lm}(\hat{\boldsymbol{n}})\,, \tag{A.5}$$

with the spherical harmonics normalization given by

$$\int d\boldsymbol{\Omega}(\hat{\boldsymbol{n}})\, Y^*_{lm}(\hat{\boldsymbol{n}}) Y_{l'm'}(\hat{\boldsymbol{n}}) = \delta_{ll'}\delta_{mm'}\,, \tag{A.6}$$

$$\sum_{lm} Y^*_{lm}(\hat{\boldsymbol{n}}') Y_{lm}(\hat{\boldsymbol{n}}) = \delta^3(\hat{\boldsymbol{n}}' - \hat{\boldsymbol{n}})\,. \tag{A.7}$$

For the specific case of the Sachs-Wolfe temperature fluctuations and when the Bardeen potential Φ is a Gaussian, the Sachs-Wolfe a_{lm} is given by

$$a_{lm} = -\frac{4\pi}{3} i^l \int \frac{d^3\boldsymbol{k}}{(2\pi)^3}\, \Phi(\boldsymbol{k})\, j_l(kx)\, Y^*_{lm}(\hat{\boldsymbol{k}})\,. \tag{A.8}$$

Appendix B

Angular four-point correlation function

In this section, we compute the angular four-point correlation function for one of the contributions. We consider the results obtained in Chapter 5. Particularly, we follow the procedure outlined in Liguori et al. (2003).

Considering equations (5.26) and (5.31), we obtain that

$$
\begin{aligned}
\langle a^{G}_{l_1m_1} a^{G}_{l_2m_2} a^{G}_{l_3m_3} a^{NG}_{l_4m_4}\rangle_c = g_{NL} \left(\frac{6}{5\pi}\right)^4 \sum_{\substack{L_iM_i\\ i=1,2,3}} F^{L_1M_1L_2M_2L_3M_3}_{l_4m_4}(r_{dec}) \\
\times \prod_{p=1}^{3} \int d^3\boldsymbol{x_p} Y^*_{l_1m_1}(\boldsymbol{\hat{n}_1}) D_{l_1}(r_1)\, Y^*_{l_2m_2}(\boldsymbol{\hat{n}_2}) D_{l_2}(r_2)\, Y^*_{l_3m_3}(\boldsymbol{\hat{n}_3}) D_{l_3}(r_3) \\
\times \prod_{j=4}^{6} \int d^3\boldsymbol{x_j} Y^*_{L_1M_1}(\boldsymbol{\hat{n}_4}) D_{L_1}(r_4)\, Y^*_{L_2M_2}(\boldsymbol{\hat{n}_5}) D_{L_2}(r_5)\, Y^*_{L_3M_3}(\boldsymbol{\hat{n}_6}) D_{L_3}(r_6) \\
\times \langle \zeta_G(\boldsymbol{x_1})\, \zeta_G(\boldsymbol{x_2})\, \zeta_G(\boldsymbol{x_3})\, \zeta_G(\boldsymbol{x_4})\, \zeta_G(\boldsymbol{x_5})\, \zeta_G(\boldsymbol{x_6})\rangle\,. \qquad \text{(B.1)}
\end{aligned}
$$

Subsequently, we decompose the ensemble average by applying the Wick theorem, leading to

$$
\begin{aligned}
\langle a^{G}_{l_1m_1} a^{G}_{l_2m_2} a^{G}_{l_3m_3} a^{NG}_{l_4m_4}\rangle_c = g_{NL} \left(\frac{6}{5\pi}\right)^4 \sum_{\substack{L_iM_i\\ i=1,2,3}} F^{L_1M_1L_2M_2L_3M_3}_{l_4m_4}(r_{dec}) \times \\
\prod_{j=1}^{6} \int dr_j r_j^2 D_{l_1}(r_1)\, D_{l_2}(r_2)\, D_{l_3}(r_3)\, D_{L_1}(r_4)\, D_{L_2}(r_5)\, D_{L_3}(r_6) \times \\
\langle \zeta^G_{l_1m_1}(r_1)\, \zeta^G_{L_2M_2}(r_5)\rangle\, \langle \zeta^G_{l_3m_3}(r_3)\, \zeta^G_{L_1M_1}(r_1)\rangle \langle \zeta^G_{l_2m_2}(r_2)\, \zeta^G_{L_3M_3}(r_6)\rangle + perm.\,, \qquad \text{(B.2)}
\end{aligned}
$$

where we have decomposed the curvature perturbation as

$$\zeta_G(\boldsymbol{x}) = \sum_{lm} \zeta^G_{lm}(r)\, Y_{lm}(\hat{\boldsymbol{n}})\,. \tag{B.3}$$

We now compute the two-point correlation functions that satisfy the following property,

$$\begin{aligned}
\langle \zeta^G_{l_1m_1}(r_1)\,\zeta^G_{L_2M_2}(r_5)\rangle &= \int d\Omega(\hat{\boldsymbol{n}}_{\boldsymbol{1}})d\Omega(\hat{\boldsymbol{n}}_{\boldsymbol{5}})Y^*_{l_1m_1}(\hat{\boldsymbol{n}}_{\boldsymbol{1}})Y^*_{L_2M_2}(\hat{\boldsymbol{n}}_{\boldsymbol{5}})\langle\zeta_G(\boldsymbol{x}_{\boldsymbol{1}})\,\zeta_G(\boldsymbol{x}_{\boldsymbol{5}})\rangle \\
&= \int d\Omega(\hat{\boldsymbol{n}}_{\boldsymbol{1}})d\Omega(\hat{\boldsymbol{n}}_{\boldsymbol{5}})Y^*_{l_1m_1}(\hat{\boldsymbol{n}}_{\boldsymbol{1}})Y^*_{L_2M_2}(\hat{\boldsymbol{n}}_{\boldsymbol{5}}) \int \frac{d^3\boldsymbol{k}}{(2\pi)^3}P_\zeta(k)e^{i(\boldsymbol{x}_1-\boldsymbol{x}_5)\cdot\boldsymbol{k}} \\
&= \frac{2}{\pi}\,(-1)^{M_2}\, i^{l_1-L_2}\,\delta_{l_1L_2}\,\delta_{m_1-M_2}\int dkk^2 j_{l_1}(kr_1)j_{L_2}(kr_5)P_\zeta(k)\,.
\end{aligned} \tag{B.4}$$

By substituting equation (B.4) into (B.2), this leads to

$$\begin{aligned}
\langle a^G_{l_1m_1}a^G_{l_2m_2}a^G_{l_3m_3}a^{NG}_{l_4m_4}\rangle = g_{NL}&\left(\frac{6}{5\pi}\right)^4\left(\frac{2}{\pi}\right)^3 \sum_{\substack{L_iM_i\\ i=1,2,3}} F^{L_1M_1L_2M_2L_3M_3}_{l_4m_4}(r_{dec}) \\
&\times\prod_{j=1}^{6}\int dr_jr_j^2 D_{l_1}(r_1)\,D_{l_2}(r_2)\,D_{l_3}(r_3)\,D_{L_1}(r_4)\,D_{L_2}(r_5)\,D_{L_3}(r_6) \\
&\times i^{l_1-L_2}\,(-1)^{M_2}\delta_{l_1L_2}\delta_{m_1-M_2}\int dkk^2 j_{l_1}(kr_1)j_{L_2}(kr_5)P_\zeta(k) \\
&\times i^{l_3-L_1}\,(-1)^{M_1}\delta_{l_3L_1}\delta_{m_3-M_1}\int dkk^2 j_{l_3}(kr_3)j_{L_1}(kr_4)P_\zeta(k) \\
&\times i^{l_2-L_3}\,(-1)^{M_3}\delta_{l_2L_3}\delta_{m_2-M_3}\int dkk^2 j_{l_2}(kr_2)j_{L_3}(kr_6)P_\zeta(k)\ + perm.\,,
\end{aligned} \tag{B.5}$$

to further simplify the above expression we can define that

$$b_{l_il_j}(r_{ij}) = \int_0^\infty dkk^2 j_{l_i}(kr_i)j_{l_j}(kr_j)P_\zeta(k)\,, \tag{B.6}$$

therefore, we obtain

$$\begin{aligned}
\langle a^G_{l_1m_1}a^G_{l_2m_2}a^G_{l_3m_3}a^{NG}_{l_4m_4}\rangle = g_{NL}\frac{10368}{625\pi^7}&\sum_{\substack{l_im_i\\ i=1,2,3}}(-1)^{-m_1-m_2-m_3}\,F^{l_3-m_3l_1-m_1l_2-m_2}_{l_4m_4}(r_{dec}) \\
&\times\prod_{j=1}^{6}\int dr_j\,r_j^2\,D_{l_1}(r_1)\,D_{l_2}(r_2)\,D_{l_3}(r_3)\,D_{l_3}(r_4)\,D_{l_1}(r_5)\,D_{l_2}(r_6) \\
&\times b_{l_1l_1}(r_{15})\,b_{l_2l_2}(r_{26})\,b_{l_3l_3}(r_{34})\ + perm.\,,
\end{aligned} \tag{B.7}$$

where P_ζ is the primordial curvature perturbation power spectrum, D_l is the radiation transfer function, and F contains the relation between the integral kernel and the filters applied to the CMB temperature field, equation (5.37). Thus, we obtain that it can be expressed as follows,

$$F_{l_4 m_4}^{l_3 - m_3 l_1 - m_1 l_2 - m_2}(r_{dec}) = \frac{6}{\pi} g_{l_4} w_{l_1} w_{l_2} \mathcal{B}_{l_4 m_4}^{l_3 - m_3 l_1 - m_1 l_2 - m_2} , \tag{B.8}$$

here, g_l and w_L are the filters whose properties are described in section 5.1, and $\mathcal{B}$ is given by

$$\mathcal{B}_{l_4 m_4}^{l_3 - m_3 l_1 - m_1 l_2 - m_2} = \int d\Omega(\hat{\boldsymbol{n}}) Y_{l_4 m_4}^{*}(\hat{\boldsymbol{n}}) Y_{l_3 - m_3}(\hat{\boldsymbol{n}}) Y_{l_1 - m_1}(\hat{\boldsymbol{n}}) Y_{l_2 - m_2}(\hat{\boldsymbol{n}}) . \tag{B.9}$$

On the other hand, to further simplify the equation (B.7), we use the property Bessel function (3.34),

$$\begin{aligned} \langle a_{l_1 m_1}^{G} a_{l_2 m_2}^{G} a_{l_3 m_3}^{G} a_{l_4 m_4}^{NG} \rangle = g_{NL} \frac{1296}{625\pi^4} & \sum_{\substack{l_i m_i \\ i=1,2,3}} (-1)^{-m_1 - m_2 - m_3} \, F_{l_4 m_4}^{l_3 - m_3 l_1 - m_1 l_2 - m_2}(r_{dec}) \\ & \times \int dr_4 \, dr_5 \, dr_6 \, r_4^2 r_5^2 r_6^2 \, D_{l_3}^2(r_4) \, D_{l_1}^2(r_5) \, D_{l_2}^2(r_6) P_\zeta^3(k) + perm. \end{aligned} \tag{B.10}$$

To compute the four-point correlation function, we must solve the Boltzmann equation to obtain the radiation transfer functions $D_l(r_{dec})$, substitute the expression for F that contains the information of the filter, and propose a specific form for the primordial curvature perturbation power spectrum, one particular choice could be a power-law power spectrum such as $P_\zeta(k) = A_\zeta k^{n_s - 4}$.

Bibliography

Ade, P. A. R. et al. (2016). Planck 2015 results. XVI. Isotropy and statistics of the CMB. *Astron. Astrophys.*, 594:A16.

Adhikari, S., Deutsch, A.-S., and Shandera, S. (2018). Statistical anisotropies in temperature and polarization fluctuations from a scale-dependent trispectrum. *Physical Review D*, 98(2).

Adhikari, S., Shandera, S., and Erickcek, A. L. (2016). Large-scale anomalies in the cosmic microwave background as signatures of non-gaussianity. *Physical Review D*, 93(2).

Aghanim, N. et al. (2020). Planck 2018 results. VI. Cosmological parameters. *Astron. Astrophys.*, 641:A6. [Erratum: Astron.Astrophys. 652, C4 (2021)].

Aghanim, N., Majumdar, S., and Silk, J. (2008). Secondary anisotropies of the CMB. *Reports on Progress in Physics*, 71(6):066902.

Akrami, Y. et al. (2020a). Planck 2018 results. IX. Constraints on primordial non-Gaussianity. *Astron. Astrophys.*, 641:A9.

Akrami, Y. et al. (2020b). Planck 2018 results. VII. Isotropy and Statistics of the CMB. *Astron. Astrophys.*, 641:A7.

Akrami, Y. et al. (2020c). Planck 2018 results. X. Constraints on inflation. *Astron. Astrophys.*, 641:A10.

Axelsson, M., Fantaye, Y., Hansen, F. K., Banday, A. J., Eriksen, H. K., and Gorski, K. M. (2013). DIRECTIONAL DEPENDENCE OF ΛCDM COSMOLOGICAL PARAMETERS. *The Astrophysical Journal*, 773(1):L3.

Babich, D., Creminelli, P., and Zaldarriaga, M. (2004). The shape of non-gaussianities. *Journal of Cosmology and Astroparticle Physics*, 2004(08):009.

Bartolo, N., Fasiello, M., Matarrese, S., and Riotto, A. (2010). Large non-gaussianities in the effective field theory approach to single-field inflation: the trispectrum. *Journal of Cosmology and Astroparticle Physics*, 2010(09):035–035.

Bartolo, N., Komatsu, E., Matarrese, S., and Riotto, A. (2004). Non-gaussianity from inflation: theory and observations. *Physics Reports*, 402(3-4):103–266.

Bartolo, N., Matarrese, S., and Riotto, A. (2004). Non-Gaussianity in the curvaton scenario. , 69(4):043503.

Bartolo, N., Matarrese, S., and Riotto, A. (2005). Primordial non-gaussianity from different cosmological scenarios. *Nuclear Physics B - Proceedings Supplements*, 148:56–63. DPU 2004.

Baumann, D. (2012). Tasi lectures on inflation.

Bellomo, N., Bartolo, N., Jimenez, R., Matarrese, S., and Verde, L. (2018). Measuring the energy scale of inflation with large scale structures. *Journal of Cosmology and Astroparticle Physics*, 2018(11):043–043.

Bjørklund, M. (2021). An analysis of non-gaussian models predicting anomalies in the cosmic microwave background.

Byrnes, C. T. (2014). Lecture notes on non-gaussianity.

Byrnes, C. T., Regan, D., Seery, D., and Tarrant, E. R. (2016a). The hemispherical asymmetry from a scale-dependent inflationary bispectrum. *Journal of Cosmology and Astroparticle Physics*, 2016(06):025–025.

Byrnes, C. T., Regan, D., Seery, D., and Tarrant, E. R. (2016b). Implications of the cosmic microwave background power asymmetry for the early universe. *Physical Review D*, 93(12).

Chen, X., Hu, B., xin Huang, M., Shiu, G., and Wang, Y. (2009). Large primordial trispectra in general single field inflation. *Journal of Cosmology and Astroparticle Physics*, 2009(08):008–008.

Cheng, C., Zhao, W., Huang, Q.-G., and Santos, L. (2016). Preferred axis of CMB parity asymmetry in the masked maps. *Physics Letters B*, 757:445–453.

Cornish, N. J., Spergel, D. N., Starkman, G. D., and Komatsu, E. (2004). Constraining the Topology of the Universe. *Physical Review Letters*, 92(20).

Cruz, M., Tucci, M., Martinez-Gonzalez, E., and Vielva, P. (2006). The non-gaussian cold spot in wmap: significance, morphology and foreground contribution. *Mon. Not. Roy. Astron. Soc.*, 369:57–67.

Dai, L., Jeong, D., Kamionkowski, M., and Chluba, J. (2013). The pesky power asymmetry. *Phys. Rev. D*, 87:123005.

de Oliveira-Costa, A., Tegmark, M., Zaldarriaga, M., and Hamilton, A. (2004). Significance of the largest scale CMB fluctuations in WMAP. *Physical Review D*, 69(6).

Erickcek, A. L., Kamionkowski, M., and Carroll, S. M. (2008). A hemispherical power asymmetry from inflation. *Physical Review D*, 78(12).

Eriksen, H. K., Banday, A. J., and Gorski, K. M. (2002). The N-point correlation functions of the COBE-DMR maps revisited. *Astronomy &amp Astrophysics*, 395(2):409–415.

Eriksen, H. K., Banday, A. J., Gorski, K. M., Hansen, F. K., and Lilje, P. B. (2007). Hemispherical power asymmetry in the third-year wilkinson microwave anisotropy probe sky maps. *The Astrophysical Journal*, 660(2):L81–L84.

Feng, C., Cooray, A., Smidt, J., O'Bryan, J., Keating, B., and Regan, D. (2015). Planck trispectrum constraints on primordial non-gaussianity at cubic order. *Physical Review D*, 92(4).

Fergusson, J. R., Regan, D. M., and Shellard, E. P. S. (2010). Optimal trispectrum estimators and wmap constraints.

Freese, K. (2009). Review of observational evidence for dark matter in the universe and in upcoming searches for dark stars. *EAS Publications Series*, 36:113–126.

Garrett, K. and Duda, G. (2011). Dark matter: A primer. *Advances in Astronomy*, 2011:1–22.

Gualdi, D., Novell, S., Gil-Marín, H., and Verde, L. (2021). Matter trispectrum: theoretical modelling and comparison to n-body simulations. *Journal of Cosmology and Astroparticle Physics*, 2021(01):015–015.

Gupta, S., Berera, A., Heavens, A. F., and Matarrese, S. (2002). Non-gaussian signatures in the cosmic background radiation from warm inflation. *Phys. Rev. D*, 66:043510.

Guth, A. H. (1981). Inflationary universe: A possible solution to the horizon and flatness problems. *Phys. Rev. D*, 23:347–356.

Hansen, F. K., Banday, A. J., Górski, K. M., Eriksen, H. K., and Lilje, P. B. (2009). POWER ASYMMETRY IN COSMIC MICROWAVE BACKGROUND FLUCTUATIONS FROM FULL SKY TO SUB-DEGREE SCALES: IS THE UNIVERSE ISOTROPIC? *The Astrophysical Journal*, 704(2):1448–1458.

Hansen, F. K., Banday, A. J., and Górski, K. M. (2004). Testing the cosmological principle of isotropy: local power-spectrum estimates of the WMAP data. *Monthly Notices of the Royal Astronomical Society*, 354(3):641–665.

Hansen, F. K., Boero, E. F., Luparello, H. E., and Garcia Lambas, D. (2023). A possible common explanation for several cosmic microwave background (CMB) anomalies: A strong impact of nearby galaxies on observed large-scale CMB fluctuations. , 675:L7.

Hansen, F. K., Trombetti, T., Bartolo, N., Natale, U., Liguori, M., Banday, A. J., and Górski, K. M. (2019). Isotropic non-gaussian g_{NL}-like toy models that reproduce cosmic microwave background anomalies. *Astronomy &amp Astrophysics*, 626:A13.

Heavens, A. (2008). The cosmological model: an overview and an outlook. *Journal of Physics: Conference Series*, 120(2). Copyright - Copyright IOP Publishing Jul 2008.

Hu, W. (2001). Angular trispectrum of the cosmic microwave background. *Physical Review D*, 64(8).

Jung, G., Ravenni, A., Baldi, M., Coulton, W. R., Jamieson, D., Karagiannis, D., Liguori, M., Shao, H., Verde, L., Villaescusa-Navarro, F., and Wandelt, B. D. (2023). Quijote-PNG: The Information Content of the Halo Mass Function.

Kalaja, A., Meerburg, P. D., Pimentel, G. L., and Coulton, W. R. (2021). Fundamental limits on constraining primordial non-gaussianity. *Journal of Cosmology and Astroparticle Physics*, 2021(04):050.

Kogo, N. and Komatsu, E. (2006). Angular trispectrum of CMB temperature anisotropy from primordial non-gaussianity with the full radiation transfer function. *Physical Review D*, 73(8).

Liguori, M., Matarrese, S., and Moscardini, L. (2003). High-resolution simulations of non-gaussian cosmic microwave background maps in spherical coordinates. *The Astrophysical Journal*, 597(1):57–65.

Linde, A. and Mukhanov, V. (1997). Non-gaussian isocurvature perturbations from inflation. *Physical Review D*, 56(2):R535–R539.

Luparello, H. E., Boero, E. F., Lares, M., Sánchez, A. G., and Lambas, D. G. (2022). The cosmic shallows – I. interaction of CMB photons in extended galaxy haloes. *Monthly Notices of the Royal Astronomical Society*, 518(4):5643–5652.

Lyth, D. H., Ungarelli, C., and Wands, D. (2003). Primordial density perturbation in the curvaton scenario. *Phys. Rev. D*, 67:023503.

Maldacena, J. (2003). Non-gaussian features of primordial fluctuations in single field inflationary models. *Journal of High Energy Physics*, 2003(5):013.

Mizuno, S. and Koyama, K. (2010). Trispectrum estimator in equilateral type non-gaussian models. *Journal of Cosmology and Astroparticle Physics*, 2010(10):002–002.

Nishimichi, T. (2012). Scale dependence of the halo bias in general local-type non-gaussian models i: analytical predictions and consistency relations. *Journal of Cosmology and Astroparticle Physics*, 2012(08):037–037.

Okamoto, T. and Hu, W. (2002). Angular trispectra of CMB temperature and polarization. *Physical Review D*, 66(6).

Peebles, P. J. E. and Yu, J. T. (1970). Primeval adiabatic perturbation in an expanding universe. *Astrophys. J.*, 162:815–836.

Regan, D., Gosenca, M., and Seery, D. (2015). Constraining the WMAP9 bispectrum and trispectrum with needlets. *Journal of Cosmology and Astroparticle Physics*, 2015(01):013–013.

Regan, D. M., Shellard, E. P. S., and Fergusson, J. R. (2010). General CMB and primordial trispectrum estimation. *Physical Review D*, 82(2).

Riess, A. G., Filippenko, A. V., Challis, P., Clocchiatti, A., Diercks, A., Garnavich, P. M., Gilliland, R. L., Hogan, C. J., Jha, S., Kirshner, R. P., Leibundgut, B., Phillips, M. M., Reiss, D., Schmidt, B. P., Schommer, R. A., Smith, R. C., Spyromilio, J., Stubbs, C., Suntzeff, N. B., and Tonry, J. (1998). Observational evidence from supernovae for an accelerating universe and a cosmological constant. *The Astronomical Journal*, 116(3):1009.

Riotto, A. (2017). Inflation and the theory of cosmological perturbations.

Ryden, B. (2016). *Introduction to Cosmology*. Cambridge University Press, 2 edition.

Sachs, R. K. and Wolfe, A. M. (1967). Perturbations of a Cosmological Model and Angular Variations of the Microwave Background. , 147:73.

Schmidt, F. and Kamionkowski, M. (2010). Halo clustering with nonlocal non-gaussianity. *Physical Review D*, 82(10).

Schwarz, D. J., Copi, C. J., Huterer, D., and Starkman, G. D. (2015). CMB anomalies after Planck. *Classical and Quantum Gravity*, 33(18):184001.

Senatore, L. and Zaldarriaga, M. (2012a). The effective field theory of multifield inflation. *Journal of High Energy Physics*, 2012(4).

Senatore, L. and Zaldarriaga, M. (2012b). A note on the consistency condition of primordial fluctuations. *Journal of Cosmology and Astroparticle Physics*, 2012(08):001–001.

Silk, J. (1967). Fluctuations in the primordial fireball. *Nature*, 215(5106):1155–1156.

Smith, K. M., Senatore, L., and Zaldarriaga, M. (2015). Optimal analysis of the cmb trispectrum.

Sunyaev, R. A. and Zeldovich, Y. B. (1970). Small-Scale Fluctuations of Relic Radiation. , 7(1):3–19.

Tegmark, M., de Oliveira-Costa, A., and Hamilton, A. J. S. (2003). High resolution foreground cleaned CMB map from WMAP. *Phys. Rev. D*, 68:123523.

Verde, L. and Heavens, A. F. (2001). On the Trispectrum as a Gaussian Test for Cosmology. , 553(1):14–24.

Verde, L., Jimenez, R., Kamionkowski, M., and Matarrese, S. (2001). Tests for primordial non-Gaussianity. , 325(1):412–418.

Verde, L., Wang, L., Heavens, A. F., and Kamionkowski, M. (2000). Large-scale structure, the cosmic microwave background and primordial non-gaussianity. *Monthly Notices of the Royal Astronomical Society*, 313(1):141–147.

Wang, L. and Kamionkowski, M. (2000). Cosmic microwave background bispectrum and inflation. *Physical Review D*, 61(6).